UNIVERSITÀ DEGLI STUDI DI PALERMO
Dottorato di ricerca in "Ingegneria Civile, Ambientale, dei Materiali"
Dipartimento di Ingegneria Civile, Ambientale, Aerospaziale, dei Materiali
Settore Scientifico Disciplinare ICAR/01

ON THE WAVE-U-OWC INTERACTION IN A NUMERICAL 2D WAVE FLUME

LA CANDIDATA

Ing. Luana Gurnari

IL COORDINATORE

Prof. Ing. Mario Di Paola

IL TUTOR

Prof. Ing. Tullio Tucciarelli

IL CO-TUTOR

Prof. Ing. Pasquale Filianoti

CICLO XXIX

ANNO 2015/2016

"If at first you don't succeed,
Try, try again"
(W.E. Hickson)

LIST OF CONTENTS

LIST OF FIGURES

NOTATION

A absorption coefficient = quotient between the absorbed energy flux and the incident wave energy flux

C quotient between $\overline{\Phi}$ and $\overline{\mathscr{E}}$

c_G group celerity

c_R propagation speed of the reflected wave energy

c wave celerity

d water depth

E mean wave energy flux

$\overline{E}$ mean wave energy per unit surface

$\overline{E}_{in}$ mean wave energy per unit surface (incident waves)

f frequency

g acceleration of gravity

$H/2$ amplitude of the incident wave

H_v quasi-antinode height

H_n quasi-node height

H_s significant wave height

h= water depth

K head loss coefficient

k wave number

k exponent in the equation of state

L wave length

l' length of the water duct

l'' height of the room containing the water column

M_a air mass

p_a pressure in the air pocket

p_{atm} atmospheric pressure

p pressure

Q water discharge of the wave

Q_p water discharge of the plant

R resonance coefficient

S the total horizontal stroke excursion

S_x solution of the problem of the wave-breakwater interaction, for which $c_R = xc_G$ with x being a given value

s' width of the vertical duct

s'' width of the oscillating water column

T wave period

T^* lag of the absolute maximum of cross-correlation ψ

t time

U^* flow coefficient

x horizontal coordinate-axis parallel to the breakwater

y horizontal coordinate-axis orthogonal to the breakwater

z vertical coordinate axis with origin at the mean water level

α volume of fraction

β amplification factor = quotient between the wave amplitude at the breakwater-converter and the wave amplitude at a conventional reflecting breakwater

ε random phase angle

Δp wave pressure on the outer opening of the plant

θ angle between the *y*-axis and the direction of wave advance

$\bar{\theta}$ mean value of θ

ξ height of the air pocket

ξ_0 still water value of ξ

φ velocity potential

η free surface elevation

η_{ph} the fluctuating pressure head

ρ water density

ρ_a air density

σ root-mean square

Φ_{abs} energy flux absorbed by the plant

$\overline{\Phi}_p$ mean value of Φ_{abs}

$\overline{\Phi}_{in}$ mean energy flux of the incident waves

ψ cross-correlation of Δp and Q_p

ω angular frequency

ABBREVIATIONS AND ACRONYMS

AMG	Algebraic MultiGrid
CFD	Computational Fluid Dynamics
ECMWF	European Centre for Medium-range Weather Forecasts
FDM	Finite Difference Method
FEM	Finite Element Method
FVM	Finite Volume Method
NDBC	National Data Buoy Center
MWL	Mean Water Level
ODE	Ordinary Differential Equations
OWC	Oscillating Water Column
REWEC	Resonant Wave Energy Converter
r.m.s	root mean square
RON	Rete Ondametrica Nazionale
PDE	Partial Differential Equation
POS	Piece Of Spectrum
PRESTO	PREssure STaggering Option
PTO	Power Take Off
S.W.L.	Still Water Level
UDF	User Defined Function.
U- OWC	U-shaped OWC
VOF	Volume Of Fluid
WEC	Wave Energy Converter
WERATLAS	European Wave Energy ATLAS

Preface

Wave energy exploitation is not mature yet in comparison with other renewable energy sources. Therefore, many different concepts are currently being developed. The widest research efforts are focused on OWCs (see, Falcão, 2003) which are fixed plants and hence easier to build and maintain, in respect to devices belonging to the family of "point absorbers" (Falnes (2002)).

An OWC consists of a box with a big vertical opening in the front wall. Waves enter through this opening with only some small diffraction effects from the front wall (see Sarmento & Falcão (1985)), and they propagate on the water surface in the box. On the roof of the box there is a tube connecting the atmosphere with the air pocket enclosed between the water surface and the roof. This tube contains one or more self-rectifying turbine (like the Wells, see Raghunathan, 1995). The air pocket inside the box, is compressed and expanded alternately. As a consequence, an air flow is produced which drives the turbine in the tube.

U-OWC plants (Boccotti, 2002-2003; Arena & Filianoti, 2007, Filianoti & Camporeale, 2008; Filianoti & Piscopo, 2015) are breakwaters in reinforced concrete embodying an OWC with an additional vertical duct on the front wall. Two kinds of plants have been widely studied: REWEC1 and REWEC3. REWEC1 (Boccotti, 2002; Boccotti P. et al., 2007; Boccotti, 2003a, 2003b; Filianoti & Camporeale, 2008; Filianoti & Piscopo, 2015) is fully beneath the sea surface, with water-driven turbines in the vertical duct. REWEC3 (Boccotti, 2003c; Filianoti & Camporeale, 2008) is in part beneath the sea level and in part above the sea level. The air pocket of the REWEC3 is connected with the atmosphere through a tube where a Wells turbine is installed. The size (width and length) of the vertical duct, the sizes (length and height) of the

room, and the diameter of the air tube must be designed so that the eingenperiod is close to the wave period, in order to operate the plant in "resonant" condition, achieving the maximum energy absorption. REWEC1 is suited for coast defense, while REWEC3 was conceived for port protection.

The performance of a U-OWC with a Wells turbine has been investigated through a small-scale field experiment by Filianoti & Camporeale (2007).

The REWEC3 (or U-OWC rel. 3) is valuable for two main reasons:

(i) it has a structure which is very close to the well-established structure of conventional caisson breakwaters;

(ii) unlike conventional OWC devices, it exploits a natural resonance with sea waves, leading to very large absorption of wave energy for different heights (and therefore periods) of incoming waves (Boccotti, 2007b).

This work has the following articulation. The first Section describes the main typologies of devices for converting wave energy, focusing the attention on REWECs. Section II contains the mathematical schemes at the base of this work. In particular, it shows the governing equations, according to Boccotti's theory on the wave field in front of the U-OWC breakwater, a simplified analytical approach for the flow motion inside the plant, and the CDF model of the numerical experiment carried on in the present work. In particular, the latter consists of the numerical integration of Reynolds averaged Navier-Stokes equation (RANS) using the commercial code Ansys Fluent 17.0, Academic Version. Sect. III introduces generation and propagation of a wave train in a flume, and explains different stages of waves (i.e. transient, progressive and standing, waves) and mathematical forms to represent them, in view of subsequent preliminary checks on the numerical flume carried out in Sect. V. The layout of the numerical experiment, the boundary and initial conditions, and the discretization of the domain are shown in Sect. IV. In

Sect. V, the validation of the numerical wave flume is presented. Then, Sect. VI shows the results of the experiment, the performance of the plant and the comparison with the experimental data illustrated in Boccotti et al., 2007. Lastly, a summary of the work and Conclusions are carried out.

1 Introduction

1.1 Wave energy resources

Wave energy stands out among the different renewable energy sources not only for its high potential but also for its high energy density, the highest of all the renewables (Lopez & Iglesias, 2014).

The first estimate of the wave energy potential was made by Barstow et al., 1998 (see Figure 1.1). They made an analysis of the wave energy resources at a few hundred discrete points, basing their analysis on 2 years of satellite altimeter data.

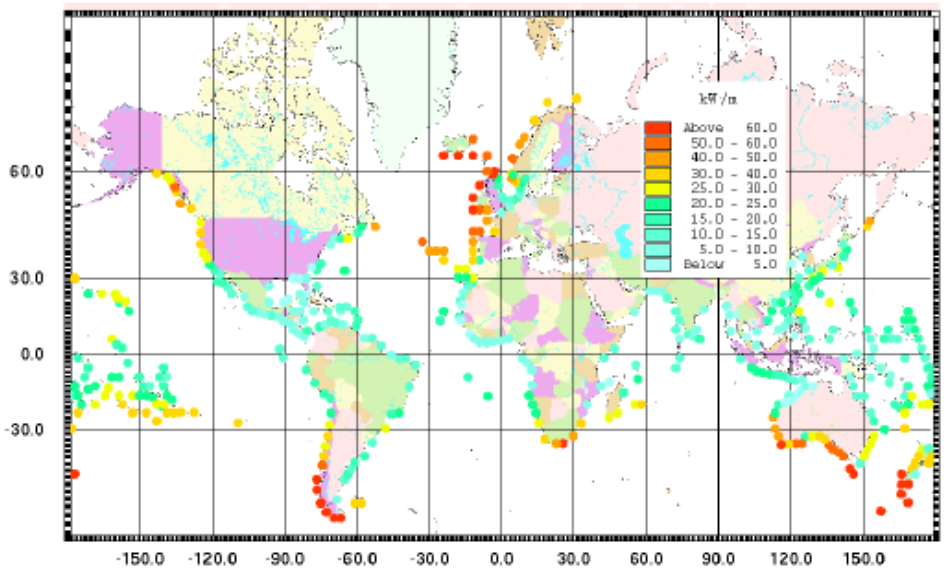

Figure 1.1 – Global wave energy estimates from Barstow et al., 1998.

Over the last fifteen years several attempts have been made to map the offshore wave energy resources. For seas and oceans surrounding Europe, the WERATLAS project (Pontes, 1998), was developed by a team of seven institutions from six European countries. It was the first attempt to assess the

offshore European wave energy resource using a common methodology and homogeneous data sets whose accuracy had been carefully evaluated. It includes a wide range of annual and seasonal wave climate and wave energy statistics for 85 offshore data points distributed along the Atlantic and Mediterranean European coasts. The WAM model is the wind wave model selected for developing WERATLAS, after a comparison of four buoy stations in the Atlantic and two buoys located in the Mediterranean, over a one-year period. WAM is a numerical model in which the two-dimensional wave spectrum was allowed to evolve freely (up to a cut-off frequency) with no constraints on the spectral shape (Komen et al.,1994).

Globally, the WorldWaves (Barstow et al., 2003) is a package for providing wave climate data and statistics everywhere on the Planet, both in deep and shallow waters. The data is derived from the European Centre for Medium-range Weather Forecasts' (ECMWF) operational and hindcast models. Then, they are calibrated by Fugro OCEANOR against satellite data, and, where available, through buoy data, to ensure the best quality (from Fugro OCEANOR website).

Several authors have reported more detailed wave energy resource assessments for particular regions or countries. As shown in Figure 1.2, Filianoti (2000) calculated the wave energy potential for the Mediterranean Sea and for several parts of the world utilizing only buoy data, such as the Italian buoy network (RON) and the American NDBC. As we see, the energy that can be harvested from ocean coasts is much greater than that of the Mediterranean coasts. In particular, along the Pacific coasts, the average annual energy is 400000 kWh/m, while for the Atlantic coasts is 150000 kWh/m.

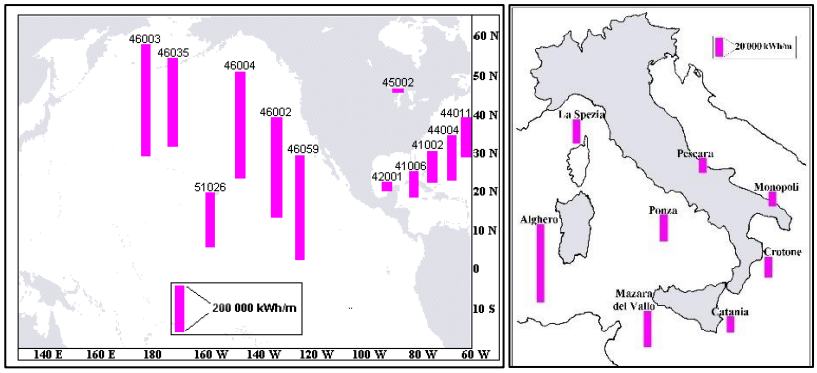

Figure 1.2 – Wave energy estimates (Filianoti, 2000): along oceanic (left panel) and Italian coasts (right panel).

1.2 The Wave Energy Converter

There is a large number of concepts for wave energy conversion; several wave energy conversion techniques have been patented all over the world. Despite this large variation in design, the Wave Energy Converters (WECs) are generally categorized by location, type and modes of operation (B. Drew, et al., 2009).

According to location the WEC devices can be categorized in:

1) Shoreline devices. They have the advantage of being close to the utility network, easy to maintain, and have a reduced chance of being damaged in extreme wave conditions. On the other hand, the shallow water leads to lower wave power. In addition, by the nature of their location, there are generally site specific requirements including shoreline geometry.

2) Nearshore devices. They are installed in relatively shallow water and they are often posed on the seabed. Like shoreline devices, a disadvantage is that shallow water leads to waves with reduced power.

3) Offshore device. They are generally in deep water. The advantage of siting a WEC in deep water is that it can harvest greater amounts of energy because of the higher energy content in deep water waves. However, offshore devices are more difficult to construct and maintain, and they need to be designed to survive the more extreme conditions.

The WEC devices can also be classified into three types or categories: point absorbers, attenuators, and terminators. Each design class uses a different method of converting wave energy to a useful form of mechanical energy. Point absorbers are characterized by device designs with very small surface areas in comparison to the incident wavelength. By means of a hydraulic system, the vertical motion is converted into a rotational movement that drives the hydraulic motor. Because of their small size, wave direction is not important for these devices. There are numerous examples of point absorbers, one of which is Ocean Power Technology's Powerbuoy (OPT — Ocean Power Technology website).

Attenuator devices are relatively long in length as compared to ocean wavelengths, and are typically positioned parallel to the general direction of wave propagation. They consist of multiple buoyant segments that articulate as wave crests and troughs pass. An example of an attenuator WEC is the Pelamis, developed by Ocean Power Delivery Ltd, now known as Pelamis Wave Power, (B. Drew et al., 2009).

Terminator wave energy converters are designed to absorb the entire, or a large portion of, energy content of incident waves. These devices have their principal axis parallel to the wave front (perpendicular to the predominant wave direction) and physically intercept waves. The most notable overtopping terminator WEC is the WaveDragon (Previsic, et al., 2004)

Another way to categorize the energy converters is based on how they capture the mechanical energy of ocean waves. Figure 1.3 shows a classification according to the modes of operation of the wave energy technologies.

An Oscillating Water Column consists of a chamber with an opening to the sea below the water line. As waves approach the device, water is forced into the chamber, applying pressure on the air within the chamber. This air escapes to atmosphere through a turbine. There are several examples of OWCs as point absorbers, as well as being built into the shoreline, where it acts as a terminator. An example of a shoreline mounted device is the Wavegen Limpet, installed on the island of Islay, Western Scotland (B. Drew et al., 2009).

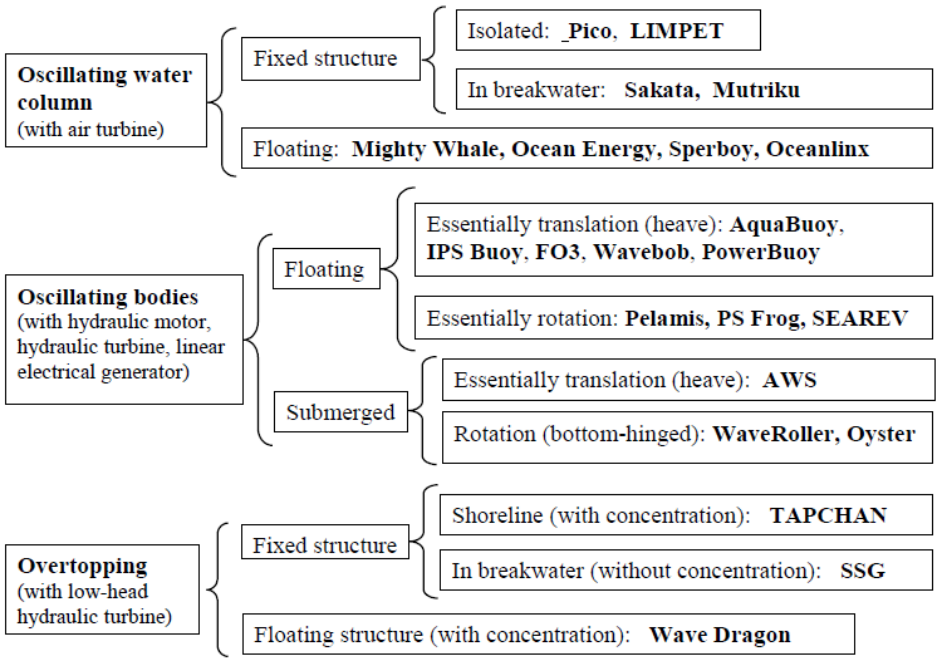

Figure 1.3 – Various wave energy technologies. Classification according to the working principles (António F. O. Falcão, 2014).

Oscillating bodies are typically offshore devices (sometimes classified as third generation devices) such as the floating or (more rarely) fully submerged device. These devices produce energy by reacting against the sea floor (or a fixed structure like a breakwater) or against another oscillating body.

An Overtopping device captures sea water of incident waves in a reservoir above the sea level, then releases the water back to sea through turbines. An example of such a device is the Wave Dragon.

1.3 The Oscillating Water Column

Oscillating water column (OWC) devices, of fixed structure or floating, are an important class of wave energy devices.

The main advantage of the OWC is its simplicity. On a practical level, as reported by Heath (2012), these advantages are that:

- the only moving part of the energy conversion mechanism is the rotor of a turbine;
- there are no moving parts in the water, as the turbine is located above water level;
- the use of an air turbine eliminates the need for gearboxes;
- it can be used on a range of collector forms situated on the coastline, in the nearshore region or floating offshore;
- it is easy to maintain.

In almost all OWCs, the air alternately flows from the chamber to the atmosphere and back. These devices have self-rectifying turbines, like the Wells, i.e. their rotational direction remains unchanged regardless of the direction of the air flow. Figure 1.4 shows a shoreline OWC scheme; under the wave action, the surface of water column rises (or decreases) and

compresses (or decompresses) the air volume in the plenum chamber. The air is forced through a duct containing the self-rectifying turbine, which connects the plenum to the atmosphere.

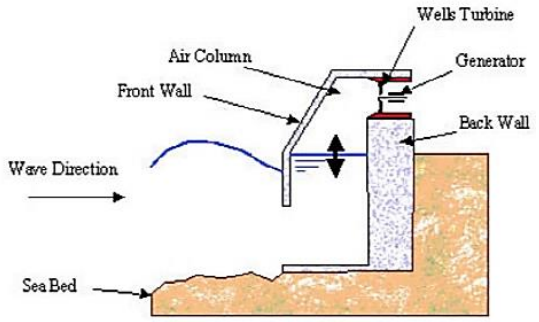

Figure 1.4 –A shoreline Oscillating Water Column scheme.

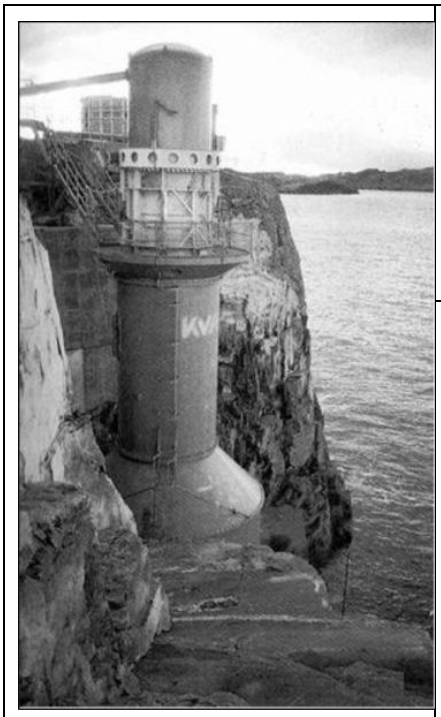

Shoreline OWC at Toftestallen, near Bergen, Norway, about 1985- Tapchan (Tapered Channel Wave Power Device)

LIMPET OWC plant installed in 2000 on the island of Islay, Scotland

OWC plant on the island of Pico, Azores, Portugal, 1999.

Figure 1.5 – Three prototypes of shoreline Oscillating Water Columns.

OWCs are a major class of wave energy converters, probably the class with the largest number of prototypes so far deployed into the sea (Falcao and Henriques, 2016). Full sized shoreline OWC prototypes, shown in Figure 1.5, were built in Norway (in Toftestallen, near Bergen, 1985), Portugal (Pico, Azores, 1999) and the UK (the LIMPET plant on Islay island, Scotland, 2000).

The largest nearshore OWC bottom-standing plant (named OSPREY) was destroyed by the sea (in 1995) shortly after having been towed and sunk into place near the Scottish coast. Full sized nearshore OWC prototypes are shown in Figure 1.6. They were built in Japan (Sakata harbor, 1990), Australia (Port Kembla, 2005), and in Spain (Mutriku harbour, Basque Country).

OWC Plant integrated in a Sakata harbor breakwater, Japan, 1990

Oceanlinx installed at Port Kembla, Australia, in 2005

Multi-chamber OWC plant integrated into a breakwater, Mutriku harbour, Basque Country, Spain, 2008–10

OSPREY- Ocean Swell Powered Renewable Energy destroyed in 1995 near the Scottish coast.

Figure 1.6 – Four prototypes of nearshore Oscillating Water Columns.

In some cases, the OWC is integrated into a breakwater and this embodiment has several advantages. For example, the constructional costs are shared, and access for construction, operation and maintenance of the wave energy plant becomes much easier. This integration was done successfully for the first time, in 1990, in the harbor of Sakata, Japan, where one of the caissons making up the breakwater has a special shape to accommodate the OWC and the mechanical and electrical equipment.

Backward Bent Duct Buoy (1:4th of full scale, tested in Galway Bay, Ireland, 2008.

Model (1:10th-scale) of Spar-buoy tested in 2012 at NAREC, UK

Mighty Whale, deployed in 1998 in Gokasho Bay, Japan.

Figure 1.7 – Three prototypes of offshore Oscillating Water Columns.

The offshore OWCs have been proposed and developed with a wide range of configurations. As we can see in Figure 1.7, a few prototypes were built in Ireland, UK and in Japan. In particular, the Spar Buoy, is possibly the simplest concept for a floating OWC. Its 1:10th-scale model was tested in 2012 at NAREC, in the United Kingdom. It is an axisymmetric device (and so insensitive to wave direction) consisting basically of a (relatively long) submerged vertical tail tube which is open at both ends and fixed to a floater that moves essentially in heave.

In the BBDB (Backward Bent Duct Buoy) device, the OWC duct is bent backward from the incident wave direction. In this way, the length of the water column could be made sufficiently large to achieve the resonance condition.

1.4 Resonant Wave Energy Converters

In the conventional OWC waves enter the plant undergoing some diffraction effects produced by the lower end of the front wall. Moreover, the eigenperiod of the plan is smaller than the wave period conveying the largest part of the energy in seas and oceans. Resonant Wave Energy Converters are a family of plant belonging to OWCs.

The first release of these devices is a submerged breakwater called REWEC1 (Resonant Wave Energy Converter, release n.1). As we can see in Figure 1.8, the REWEC1 has a vertical duct on the wave beaten side that extends transversally along the whole caisson and is connected to the sea through an upper opening and to an inner chamber through a lower opening. this chamber contains a water mass in its lower part and an air pocket in its upper part. The height of the air pocket is set through an air compressor, in order to obtain the resonance condition between the period of the pressure

fluctuations on the upper opening of the duct and the eigenperiod of the plant. Arena & Filianoti (2003), described a small-scale field experiment, carried out directly at sea in the OKEANOS laboratory, with the aim of checking whether the resonance condition can be obtained by regulating the mass of air inside the plant.

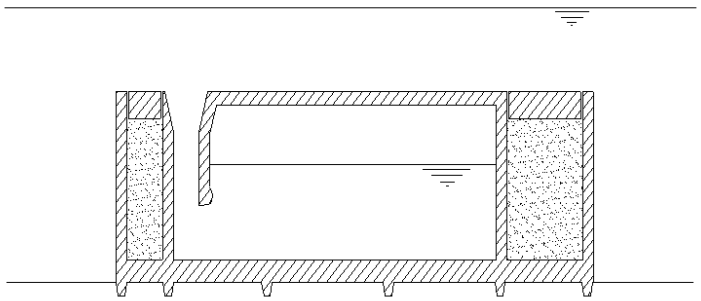

Figure 1.8 – Vertical cross section of Boccotti's submerged breakwater (REWEC1).

The REWEC1 is able to absorb the wave energy and to protect coasts. As confirmed by Filianoti and Piscopo, (2015), the energy transmission behind the breakwater is limited, thanks to the resonance that maximize the energy absorption by the plant.

The second release (REWEC2) is essentially a caisson breakwater that incorporates a REWEC1. This release was made in order to have the turbines above the sea level. The plenum, as we can see in Figure 1.9, is connected to two reservoirs where there is a compressor which serves to feed air into the plant (that is into the air-duct, the air pocket and the air reservoirs); the exhaust valve serves to release some air from the plant. The advantages are that being above sea level the turbine is easy to maintain and that the air mass can be varied both by operating the gate valves which intercept the reservoirs (see Figure 1.9) and through the compressor. This optional mode allows the

eigenperiod of the plant to be varied in a large range, making it possible to tune the plant with the largest part of the waves hitting the plant.

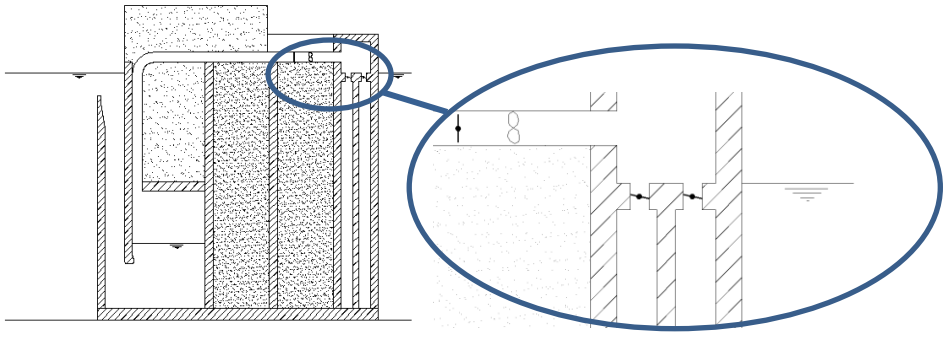

Figure 1.9 – Scheme of a caisson breakwater that incorporates a REWEC1 (REWEC2).

The last release of these devices is called REWEC3 (see Figure 1.10). It essentially consists of a vertical U-conduit, which extends along the wave-beaten side of the caisson, and it is connected with the sea through an upper opening. Under the wave action, the pressure on the upper opening of the vertical duct fluctuates and, as a consequence, the water oscillates vertically in the plenum chamber.

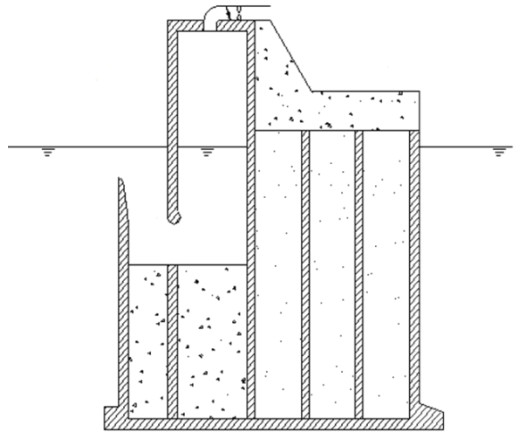

Figure 1.10 – Scheme of a caisson breakwater embodying an OWC with an additional vertical duct (REWEC3).

A small-scale model of this breakwater has been placed off the coast of Reggio Calabria in the eastern coast of the Messina Straits (Southern Italy). The results of the experiment were described by Boccotti et al. (2007) and by Filianoti and Camporeale (2007-2009a -2009b). The experiment permitted the analysis the energy conversion from the fluctuating water flow at the outer opening of the vertical duct to the fluctuating air motion across the turbine. Moreover, the performance of the Wells turbine was analysed under real, randomly varying sea conditions.

REWEC3 is simpler to operate and maintain than REWEC1 and REWEC2, because the air in the chamber is, on average, at atmospheric pressure. For this reason, there is no risk of air leakages from the plenum chamber. Furthermore, the REWEC3 does not require substantial structural changes from the well-established structure and construction technique of cellular caisson breakwaters.

1.5 Open challenges in the conversion of wave energy

The harvesting of the wave energy had, and still has, several challenges to face. They include the efficiency of system, material selection, wind and wave forces, corrosion and biofouling, energy storage, daily and seasonal wave characteristics variations (R.H. Charlier and J.R. Justus, 1993).

First of all, WEC devices have to face great challenges once at sea and several prototypes have not survived (e.g. OSPREY). Additionally, in offshore locations, wave direction is highly variable, and so wave devices have to align themselves accordingly on compliant moorings, or be symmetrical, in order to capture the energy of the wave. The directions of waves near the shore can be largely determined in advance owing to the natural phenomena of

refraction and reflection. The challenge of efficiently capturing this irregular motion also has an impact on the design of the device (B. Drew et al., 2009).

As we can see in Figure 1.11, there are also challenges in order to harvest wave energy. The major difficulties regard the anchoring and the mooring. Indeed, especially for the offshore devices, they have to resist to stronger current and higher sea states. Indeed, the highest waves are the most productive but pose also the major design and constructions problems (R.H. Charlier and J.R. Justus, 1993).

Another problem regards power cables and grid connection, that are very expensive at sea, thinking that for offshore wind power farms the internal power connection is 5% of the total cost and grid connection is 10% (as reported by *www.wavepiston.dk*).

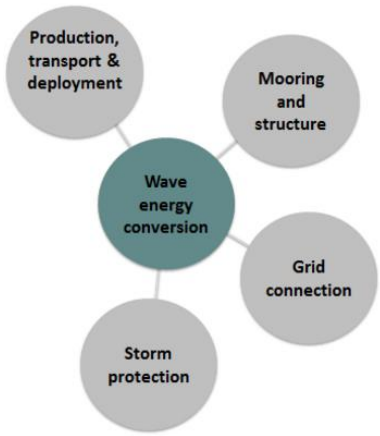

Figure 1.11 – Wave power challenges (from *www.wavepiston.dk*).

Also, the maintenance and the survivability in seawater are some challenges. The correct choice of design and material is essential, in order to mitigate the highly corrosive environment where the devices operate.

Nevertheless, it is working to improve the design of the WEC devices to optimize the extraction of wave energy under most wave conditions.

2 Mathematical schemes for the wave-U-OWC interaction

2.1 The governing equations

2.1.1 The waves before the U-OWC

The problem of wave motion before the breakwater must be solved in order to determine the pressure fluctuation Δp, on the outer end of the vertical duct. This has been solved by Boccotti (2007a), supposing that every periodic waveform has a given frequency and the mean energy flux smaller than (or equal to) the mean energy flux of the incident waves. Then, looking at the waveform which satisfies the equations of wave-OWC interaction, and gives the largest value of $\overline{\Phi}/\overline{\mathscr{E}}$ (mean energy flux / mean energy per unit surface), it has been shown that, in most cases the wave motion before the breakwater is the superimposition of the standing waves, yielded by the reflection of the incident waves, with a progressive wave generated by the water discharge through the plant. In some cases, the solution giving the largest value of $\overline{\Phi}/\overline{\mathscr{E}}$ proves to be a sum of two standing waves with phase angles in space and time. In these cases (the sum of two standing waves), the plant may absorb up to 100% of the incident wave energy.

According to Boccotti (2007a), there are two forms of wave fields: superimposition of standing with progressive waves and superimposition of two standing waves.

2.1.1.1. Superimposition of two standing waves

Referring to the scheme represented in Figure 2.1, the periodic wave function (having height H, wave number k and angular frequency ω) can be exprest in the form

$$\eta(y,t) = [\beta \cos ky \cos(\omega t) + \alpha \sin ky \cos(\omega t + \varepsilon)]H, \tag{2.1}$$

where α and β are two factors which are to be determined. In particular, β is the quotient between the wave height at the breakwater converter and the wave height at a conventional reflecting breakwater.

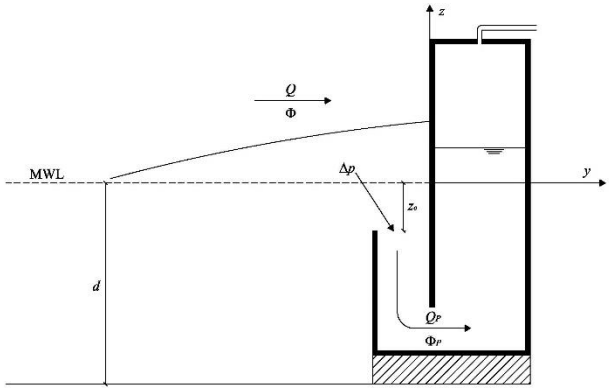

Figure 2.1 - Reference scheme for the calculation of the wave field in front of the U-OWC.

From the distribution of velocity potential associated with the wave (2.1), we obtain the expression of the wave pressure $\Delta p(t)$ on the outer opening of the vertical duct:

$$\Delta p(t) = \rho g \beta H \cos(\omega t) \frac{\cosh[k(d + z_o)]}{\cosh(kd)}. \tag{2.2}$$

The water discharge of the wave at the converter is

$$Q(t) = -g\alpha H \omega^{-1} \tanh(kd) \sin(\omega t + \varepsilon); \tag{2.3}$$

the average wave energy flux and the mean wave energy per unit surface are respectively:

$$\overline{\Phi} = -4\alpha\beta \sin\varepsilon \overline{\Phi}_{in}\,, \tag{2.4}$$

$$\overline{\mathscr{E}} = 2(\alpha^2 + \beta^2)\overline{\mathscr{E}}_{in}\,, \tag{2.5}$$

$\overline{\Phi}_{in}$ and $\overline{\mathscr{E}}_{in}$ being the mean values referred to the incident waves.

The wave field gradually expands seaward with a propagation speed c_R. The ratio χ ($\leq$1) between c_R and c_G (the group velocity of a progressive wave) is

$$\chi = \frac{c_R}{c_G} = \frac{1 + 4\alpha\beta \sin\varepsilon}{2(\alpha^2 + \beta^2) - 1}\,. \tag{2.6}$$

Boccotti (2007a) chose the value of β among the ∞^1 solutions which, at all instants of time, fulfill the conditions that:

(i) the water discharge $Q_p(t)$ entering (or exiting from) the plant must be equal to the water discharge $Q(t)$ of the wave at the converter;

(ii) the energy flux absorbed by the plant $\overline{\Phi}_p$ must be equal to the wave energy flux $\overline{\Phi}$ at the breakwater converter.

As a consequence of the conditions (i), the phase angle between $\Delta p(t)$ and $Q_p(t)$ must be equal to the phase angle between $\Delta p(t)$ and $Q(t)$, resulting in:

$$\varepsilon = -\frac{\pi}{2}\left(1 + \frac{4T^*}{T}\right), \tag{2.7}$$

where T^* is the known time lag of $Q_p(t)$ with respect to $\Delta p(t)$ and T is the wave period.

The ratio $R \equiv 4T^* / T$ is called "resonant coefficient". It can vary from -1 to 1: *R* negative means that the wave period is greater than the eigenperiod, *R* positive means that the wave period is smaller than the eigenperiod. If *R*=0 the plant absorbs the maximum ratio of the incident wave energy.

The condition (ii) implies

$$\alpha = \frac{\overline{\Phi}_p}{4\beta \sin(\varepsilon)\overline{\Phi}_{\text{in}}} \ . \tag{2.8}$$

The selected β is the one giving the largest value of the quotient between mean energy flux $\overline{\Phi}$ and mean energy per unit surface $\overline{\mathscr{E}}$ (i.e. the largest value of the propagation speed of the wave energy reflected by the breakwater-converter). Calling *C* this quotient, its expression is

$$C = \frac{\overline{\Phi}}{\overline{\mathscr{E}}} = \frac{-2\alpha\beta \sin\varepsilon}{\alpha^2 + \beta^2} c_G \ , \tag{2.9}$$

where c_G is the group velocity.

Boccotti, (2007) suggests the following sequence of calculations:

(i) fix a value of β greater than zero;

(ii) obtain $\Delta p(t)$ with Eq. (2.2);

(iii) solve, numerically, the equation of flow inside the plant and as results obtain the water discharge of the plant $Q_p(t)$, the energy flux absorbed by the plant $\Phi_p(t)$ and its mean value $\overline{\Phi}_p$;

(iv) evaluate the time lag T^* of $Q_p(t)$ with respect to $\Delta p(t)$;

(v) calculate ε by means of Eq. (2.7)

(vi) find α such that $\overline{\Phi}$ [Eq. (2.4)] be equal to $\overline{\Phi}_p$;

(vii) calculate *C* with Eq. (2.9);

(viii) repeat the sequence from (i) to (vii) till you find the values of β, α and ε giving the largest value of *C*.

The calculation of β, α and ε is preparatory to evaluate:

- the performance of the U-OWC absorber, in particular the absorption coefficient *A*

$$A = \frac{\overline{\Phi}_p}{\overline{\Phi}_{\text{in}}} = -4\alpha\beta \sin\varepsilon \ ; \tag{2.10}$$

- the wave field in front of the absorber [Eqs (2.1), (2.6)] and other derived].

2.1.1.2. Superimposition of standing wave with progressive waves

Before the breakwater-converter we have

$$\eta(y,t) = \eta_1(y,t) + \eta_2(y,t), \tag{2.11}$$

where $\eta_1(y,t)$ is the standing wave which is produced before a reflecting wall:

$$\eta_1(y,t) = H\cos(ky)\cos(\omega t), \tag{2.12}$$

and $\eta_2(y,t)$ is the wave generated by the discharge entering (or exiting from) the plant:

$$\eta_2(y,t) = \hat{\alpha}H\cos(ky + \omega t + \hat{\varepsilon}), \tag{2.13}$$

where, without loss of generality, we assume

$$\hat{\alpha} > 0. \tag{2.14}$$

Eq.(2.13) represents a progressive wave moving towards the open sea. Here $\hat{\alpha}$ and $\hat{\varepsilon}$ are to be determined.

From the distribution of velocity potential associated with wave (2.11) we get the following expression of the mean energy flux per unit length and of the mean energy per unit surface:

$$\overline{\Phi} = -4(\hat{\alpha}^2 + \hat{\alpha}\cos\hat{\varepsilon})\overline{\Phi}_{in}, \tag{2.15}$$

$$\overline{\mathscr{E}} = (2 + 4\hat{\alpha}^2 + 4\hat{\alpha}\cos\hat{\varepsilon})\overline{\mathscr{E}}_{in}, \tag{2.16}$$

where $\overline{\Phi}_{in}$ and $\overline{\mathscr{E}}_{in}$ are, respectively, the mean energy flux per unit length, and the mean energy per unit surface of the incident waves, that is to say

$$\overline{\Phi}_{in} = \frac{1}{8}\rho g H^2 c_G, \tag{2.17}$$

$$\overline{\mathscr{E}}_{in} = \frac{1}{8}\rho g H^2. \tag{2.18}$$

Moreover, we get the following expression for the water discharge (per unit length) of the wave at $y = 0$:

$$Q(t) = -\frac{\omega}{k}\hat{\alpha} H \cos(\omega t + \hat{\varepsilon}). \tag{2.19}$$

It is convenient to shift the origin of time so that it coincides with a wave crest at $y = 0$. Thus, if we call βH the wave amplitude at $y = 0$, we may write

$$\eta(0,t) = \beta H \cos(\omega t), \tag{2.20}$$

$$\eta_1(0,t) = H \cos(\omega t + \varepsilon_1), \tag{2.21}$$

$$\eta_2(0,t) = \hat{\alpha} H \cos(\omega t + \varepsilon_2), \tag{2.22}$$

$$Q(t) = -\frac{\omega}{k}\hat{\alpha} H \cos(\omega t + \varepsilon_2), \tag{2.23}$$

where $\varepsilon_1, \varepsilon_2$ and $\hat{\alpha}, \beta$ are to be determined.

If we fix a tentative value of β, we know $\eta(0,t)$,eq. (2.20), and consequently we know the pressure fluctuation on the opening of the vertical duct:

$$\Delta p(t) = \rho g \frac{\cosh[k(d+z_o)]}{\cosh(kd)} \beta H \cos(\omega t). \tag{2.24}$$

Once we have calculated the flow inside the plant, we know $Q_p(t)$ and $\Phi_p(t)$. Hence, we can obtain the mean value $\overline{\Phi}_p$ which will serve later, and the phase angle between $Q_p(t)$ and $\Delta p(t)$. This phase angle must be equal to the phase angle between $Q(t)$ and $\Delta p(t)$. The fact that the known phase angle between $Q_p(t)$ and $\Delta p(t)$ must be equal to the unknown phase angle between $Q(t)$ and $\Delta p(t)$ enables us to obtain the unknown angle ε_2. We have

$$\varepsilon_2 = -\pi - \frac{4T^*}{T}\frac{\pi}{2}, \tag{2.25}$$

where T^* is the known time lag of $Q_p(t)$ with respect to $\Delta p(t)$.

Since the plant absorbs energy, T^* must fall in $(-T/4, T/4)$, and hence (2.25) implies the inequality

$$-\frac{3\pi}{2} < \varepsilon_2 < -\frac{\pi}{2}. \tag{2.26}$$

From (2.11)and (2.20-23) the equation

$$\beta\cos(\omega t) = \cos(\omega t + \varepsilon_1) + \hat{\alpha}\cos(\omega t + \varepsilon_2) \tag{2.27}$$

follows, which implies

$$\cos\varepsilon_1 = \beta - \hat{\alpha}\cos\varepsilon_2, \tag{2.28}$$

$$\sin \varepsilon_1 = -\hat{\alpha} \sin \varepsilon_2, \tag{2.29}$$

which, in their turns, imply

$$\hat{\alpha}^2 - 2\beta \cos \varepsilon_2 \hat{\alpha} = 1 - \beta^2. \tag{2.30}$$

Given that ε_2 is known, eq.(2.30) enables us to obtain $\hat{\alpha}$. Hence, we also obtain ε_1 by means of eqq. (2.28), (2.29). Finally, when ε_1 and ε_2 are known we can obtain $\hat{\varepsilon}$ with the equation

$$\hat{\varepsilon} = \varepsilon_2 - \varepsilon_1. \tag{2.31}$$

Boccotti (2007), suggests the following sequence of calculations:

(i) fix a value of β between 0 and 1;

(ii) obtain $\Delta p(t)$ with (2.24);

(iii) solve, numerically, the equations of flow inside the plant, and as results obtain $Q_p(t)$, $\Phi_p(t)$, $\overline{\Phi}_p$;

(iv) evaluate the time lag T^* of $Q_p(t)$ with respect to $\Delta p(t)$;

(v) calculate ε_2 with (2.25);

(vi) calculate $\hat{\alpha}$ with (2.30)

(vii) calculate ε_1 with (2.28), (2.29);

(viii) calculate $\hat{\varepsilon}$ with (2.31);

(ix) calculate $\overline{\Phi}$ with (2.15).

If $\overline{\varphi}$ proves to be equal to $\overline{\varphi}_p$ the problem is resolved. Indeed, in the solution for ε_2 we have fulfilled the condition that the phase angle between $Q_p(t)$ and $\Delta p(t)$ be equal to the phase angle between $Q(t)$ and $\Delta p(t)$, from

which it follows that the phase angle between $Q(t)$ and $Q_p(t)$ is equal to zero.

2.1.2 *The water/air motion inside the plant*

The study of the flow motion inside the absorber has been carried out by Boccotti (2007a, 2003a.). With reference to the scheme of Figure 2.2, the equation of the water flow inside a cell may be expressed in the form

$$\frac{(l''-\xi)}{g}\frac{\mathrm{d}^2\xi}{\mathrm{d}t^2}+\frac{l'}{g}\frac{\mathrm{d}u}{\mathrm{d}t^2}=h'-h''-\Delta h_w, \tag{2.32}$$

where the head losses Δh_w (both continuous and minor) and the velocity u in the vertical duct are respectively

$$\Delta h_w=\left(\frac{\lambda_w}{4\mathcal{R}}l'+K_w\right)\frac{|u|u}{2g}, \tag{2.33}$$

$$u=\frac{s''}{s'}\frac{\mathrm{d}\xi}{\mathrm{d}t}, \tag{2.34}$$

where $\mathcal{R}$ is the hydraulic radius, λ_w is the friction coefficient and K_w is the minor loss coefficient, assuming a unique value independent from the flow direction.

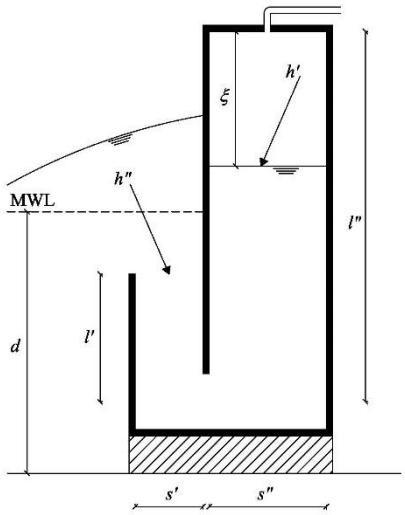

Figure 2.2- Reference scheme of a U-OWC.

The energies per unit weight are

$$h' = \xi_0 - \xi + \frac{1}{2g}\left(\frac{\mathrm{d}\xi}{\mathrm{d}t}\right)^2 + \frac{p_a - p_{atm}}{\rho g}, \tag{2.35}$$

$$h'' = \frac{\Delta p}{\rho g}, \tag{2.36}$$

where p_a is the pressure in the air pocket, p_{atm} is the atmospheric pressure, Δp is the wave pressure on the upper opening of the vertical duct. Eq (2.36) is rigorous with the linear theory of wave motion.

The air density in the plenum is

$$\rho_a = \frac{M_a}{bs''\xi}, \tag{2.37}$$

and it varies with time because of variations of air mass M_a and because of variations of height ξ. The pressure in the air pocket is related to the air density by the equation of state

$$\frac{p_a}{\rho_a^k} = \frac{p_{atm}}{\rho_{atm}^k}. \tag{2.38}$$

The velocity u_a in the air tube is related to pressure p_a of the air pocket:

$$K_a \frac{u_a^2}{2} \frac{u_a}{|u_a|} = \frac{p_{atm}}{\rho_{atm}} \frac{k}{k-1} \left[\left(\frac{p_a}{p_{atm}} \right)^{1-1/k} - 1 \right], \tag{2.39}$$

where K_a is the head loss coefficient in the air tube.

The rate of change of the air mass in the air pocket is related to u_a and ρ_a:

$$\frac{\mathrm{d}M_a}{\mathrm{d}t} = -\frac{1}{2}(\rho_a + \rho_{atm}) \frac{\pi D^2}{4} u_a. \tag{2.40}$$

Equations (2.32) and (2.40) are integrated numerically from the knowledge of $\Delta p(t)$ and of conditions at time t=0:

$$\frac{\mathrm{d}\xi}{\mathrm{d}t} = 0, \quad \xi = \xi_0, \quad M_a = \rho_{atm} bs" \xi_0. \tag{2.41}$$

The flow chart is shown in Figure 2.3

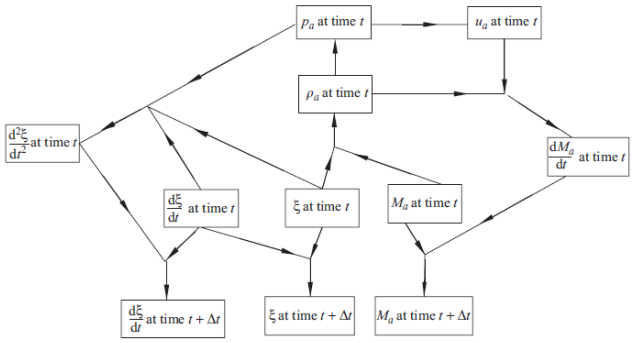

Figure 2.3- Flow chart for the U-OWC (Boccotti 2007).

The mathematical model has been validated and calibrated against the experimental results obtained in the field on a small-scale model (Boccotti et al., 2007).

2.1.3 The Power Take Off (PTO) system

The Power Take Off (PTO) system converts the pneumatic power into electricity or some other usable form. The PTO is typically an air turbine and normally is a self-rectifying turbine.

Wave energy power plants experienced a renewed interest after the introduction of the Wells turbine. In fact, the Wells turbine is commonly adopted in OWC wave energy converters, where, due to the wave motion, the pressure at the inlet of the vertical duct generates pressure fluctuations in the plenum, thus producing an oscillating air flow able to drive a turbine. The transformation of the oscillatory motion of the air column in the unidirectional rotational motion of the turbine can be effectively performed by the self-rectifying Wells turbine. It is an axial-flow turbine, composed of a rotor with untwisted airfoil blades of a symmetrical cross section, usually belonging to the NACA00XX series (see Figure 2.4).

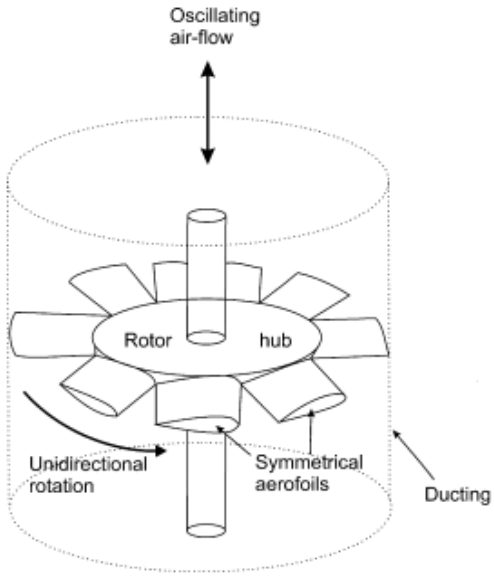

Figure 2.4- The Wells turbine.

The main feature of the Wells turbine is its capability of producing time-averaged positive power from a cyclically reversing flow. Figure 2.5 illustrates the forces acting on the blades mounted on the turbine hub. Given an axial velocity V and α tangential rotor velocity U, the relative flow velocity W_1 forms an angle a with respect to the blade chord, generating lift, L, and drag, D, forces perpendicular and parallel to W_1, respectively. These forces can be split into the tangential F_u, and axial F_a, forces, whose magnitude varies during the cycle. However, the F_u direction is predominantly independent of the flow direction (Raghunathan S, 1995).

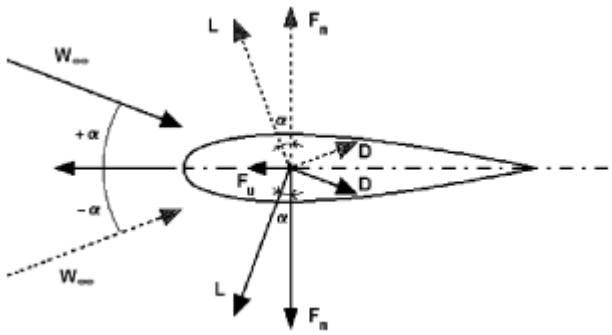

Figure 2.5- Forces acting on the blade.

The power conversion system in an oscillating water column wave device chain is illustrated in Figure 2.6.

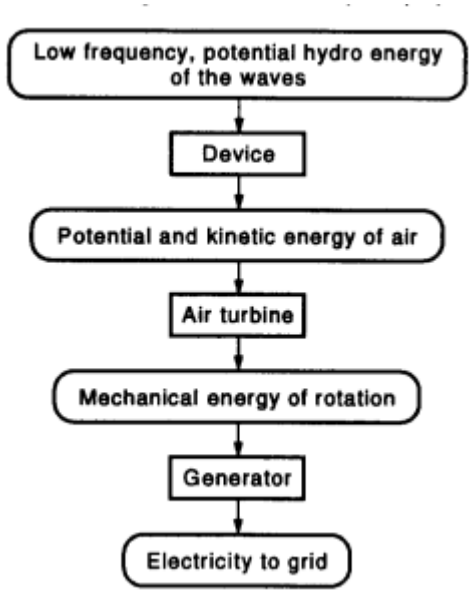

Figure 2.6- A typical wave energy conversion system (S. Raghunathan., 1995).

The performance of the Wells turbine can be expressed in terms of non-dimensional parameters,

$$T^* = \frac{T_t}{\rho_a \ \omega^2 \ R_{\text{tip}}^5}, \qquad (2.42)$$

where T_t is the torque referred to the internal (blade) power P_t

$$T_t = P_t / \omega , \tag{2.43}$$

ρ_a is the air density, ω is the angular speed, R_{tip} is the blade tip radius, and Δp_0^* is the non-dimensional stagnation pressure drop, defined as:

$$\Delta p_0^* = \frac{\Delta p_0}{\rho \omega^2 R_{tip}^2} , \tag{2.44}$$

where Δp_0 is the stagnation pressure drop across the turbine. The characteristic curves are given against the flow coefficient

$$\phi = \frac{V}{\omega R_{tip}} , \tag{2.45}$$

where V is the average axial velocity in the turbine annulus, evaluated from the volumetric flow rate Q and the annulus area A_t through

$$V = \frac{Q}{A_t} . \tag{2.46}$$

The efficiency η, is defined as:

$$\eta = \frac{T\omega}{Q\Delta p_0}. \tag{2.47}$$

In Figures 2.7, 2.8 and 2.9 the comparison carried out between the experimental data (Curran and Gato, 1997) and CDF simulation by Torresi et al. (2004 and 2008) at the same working condition is shown. In particular, Figure 2.7, shows the torque coefficient characteristics, defined by eq. (2.42). The results of Torresi et al. (2004 and 2008) simulations are in reasonable good agreement with the experimental data, in particular the torque coefficient is very close to the experimental data until the flow coefficient U*=0.2, before reaching the stall conditions around U*=0.225.

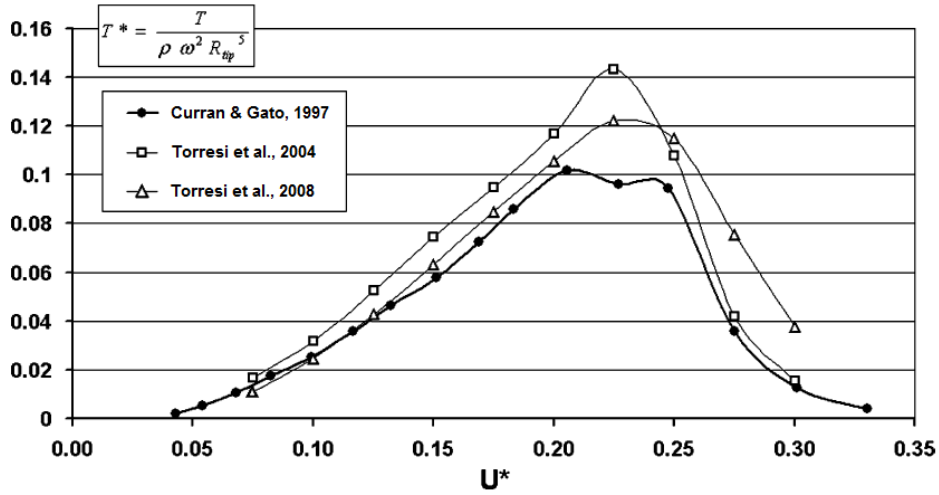

Figure 2.7- Torque coefficient characteristics (Torresi et al., 2008).

Figures 2.8 and 2.9 show the non-dimensional total pressure drop, defined by eq. (2.44), and the efficiency characteristics, eq. (2.47), respectively.

As we can see in Figure 2.8, the non-dimensional total pressure drop has a linear variation with the flow rate coefficient U*. There, we can see the absolute correspondence between experimental data and CFD simulation.

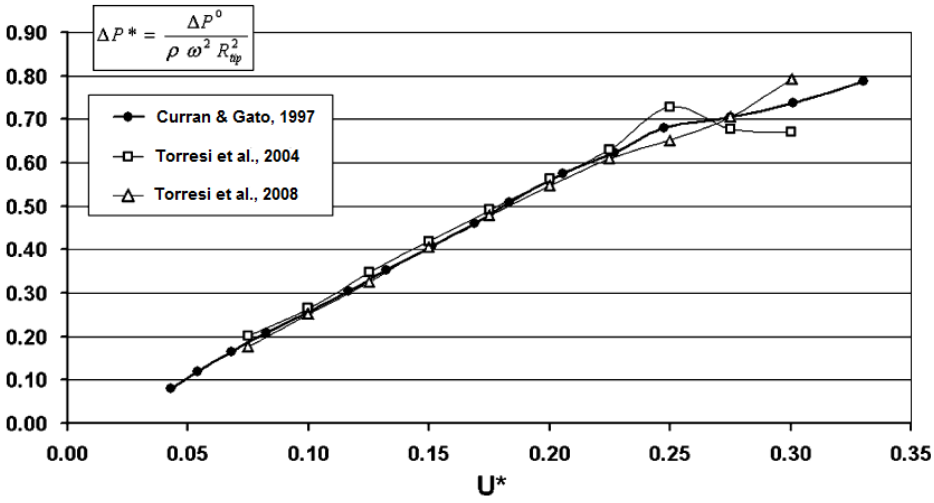

Figure 2.8- Non-dimensional total pressure drop characteristics (Torresi et al., 2008).

The efficiency (see Figure 2.9), remains quite constant for a range of U* values included between 0.10 and 0.20 and at the U* value equal to 0.15, the efficiency is at its maximum.

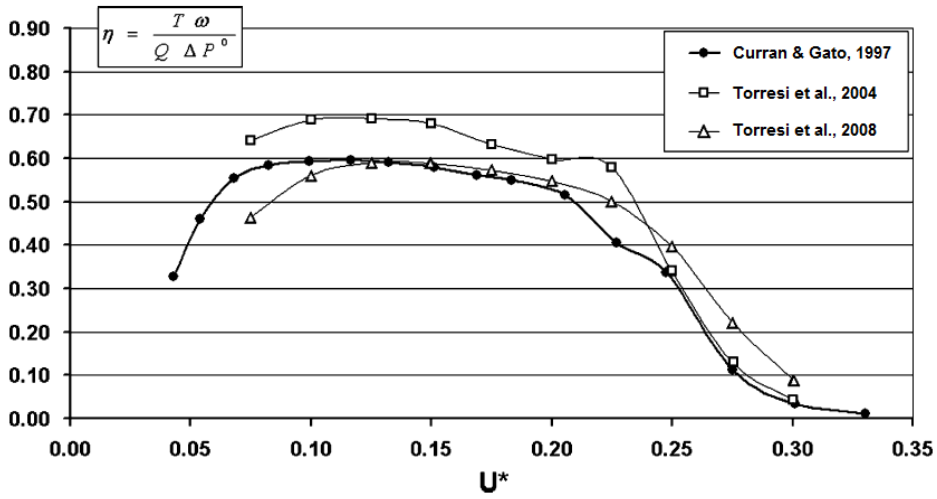

Figure 2.9- Efficiency characteristics (Torresi et al., 2008).

2.2 The Simplified one-dimensional approach

2.2.1 Mechanical system equivalent to the U-OWC

An analytical solution for the U-OWCs has been proposed by Filianoti & Camporeale (2008), using a linearized form of Eq. (2.32) obtained considering small displacements of ξ from the value of static equilibrium ξ_0, and an incompressible flow in the air tube. The linearized form obtained consists of a system of 2nd order ordinary differential equations, analogous to the equations that describe the mechanical spring-mass-damper system shown in Figure 2.10.

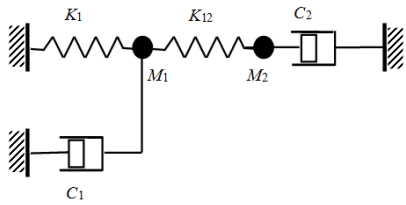

Figure 2.10 - The mechanical system equivalent to U-OWCs (Filianoti & Camporeale, 2008).

Terms that are necessary to linearize are the fluid dynamic head losses of the water in the duct and the polytropic which governs the air transformation in the plenum (which works like a gas spring).

Expanding terms Δh_w, u, h' and h'' in Eq. (2.32) by means of Eqs (2.33), (2.34) (2.35) and (4.36) respectively, we obtain

$$A\frac{\mathrm{d}^2 y}{\mathrm{d}t^2} - \frac{B_w}{g}\left|\frac{\mathrm{d}y}{\mathrm{d}t}\right|\frac{\mathrm{d}y}{\mathrm{d}t} + \frac{p_a - p_{atm}}{\rho g} + y = \Delta p(t)\,, \tag{2.48}$$

where

$$B_w \equiv \frac{1}{2}\left(\frac{\lambda_w}{4\mathcal{R}}l + K_w\right)\left(\frac{s''}{s'}\right)^2, \tag{2.49}$$

and

$$y = \xi - \xi_0 \tag{2.50}$$

is the displacement of the water surface in the air chamber.

Assuming small oscillations of the water-air interface in the room, round the rest position, it is possible to express Eq (2.48) in the form

$$A'\frac{\mathrm{d}^2 y}{\mathrm{d}t^2} + F'\frac{\mathrm{d}y}{\mathrm{d}t} + Q'y = -\frac{\Delta p}{\rho g}, \tag{2.51}$$

where ρ is the water density, g is the acceleration of gravity, terms A' and Q' follow straight forwardly from the Taylor series expansion of 2nd order term coefficient in Eq. (2.33) and polytropic law (2.38), respectively:

$$A' \equiv \frac{1}{g}\left(l' - \zeta_0 + \frac{s'}{s''} l' \right), \tag{2.52}$$

$$Q' \equiv \left(\xi_0 + \frac{p_{\text{atm}}}{\rho g} \right) \frac{k}{\xi_0} + 1. \tag{2.53}$$

The expression of coefficient F', is obtained by equating the mean dissipated power in the actual turbulent flow (non-linear model) to the mean dissipated power in a laminar flow having the same peak period T_p of the energy spectrum of the velocity process.

Neglecting the kinetic term in the air-water interface in the chamber, we obtain:

$$F' \equiv \frac{1}{2g} \left(\frac{\lambda_w}{4\mathcal{R}} l + K_w \right) \left(\frac{s'}{s''} \right)^2 K_{ad} \,. \tag{2.54}$$

Filianoti & Camporeale (2008) show that the U-OWC dynamic behaviour is characterized by a core of waves constituted by the 3rd part of the highest waves in the sea state. Consequently, they calculated the mean adequacy coefficient $K_{ad\,1/3}$ (= turbulent flow mean energy losses / laminar flow mean energy losses) relevant to the highest third of the waves of velocity fluctuations in the vertical duct, assuming that the random water flowing in the vertical duct is represented by a Gaussian process with an infinitely narrow energy spectrum:

$$(K_{ad})_{1/3} = \frac{\int_{U_{1/3}}^{\infty} K_{ad}\, p(u; \sigma_v = w) \mathrm{d}u}{\int_{U_{1/3}}^{\infty} p(u; \sigma_v = w) \mathrm{d}u} \,. \tag{2.55}$$

The product $p(u;\sigma_v = w)$ is the probability of a velocity amplitude within the fixed small interval (u, u+ du), in a sea state with a given standard deviation $\sigma_v = w$; and $U_{1/3}$ is the threshold being exceeded by 1/3 wave heights of velocity fluctuations. Solving the integrals in Eq. (2.51), we arrive at

$$(K_{ad})_{1/3} = \frac{16}{3\pi}\sigma_v . \tag{2.56}$$

An iteration process is necessary to calculate σ_v (in all worked calculations a few iterations have been necessary to achieve convergence).

2.2.2 *Energy conversion step by step: partial efficiency*

The electrical power generation through a U-OWC plant involves the conversion of energy in several intermediate forms. The first is the conversion of wave energy into hydraulic energy from the water current inside the duct. Then, we have the pneumatic energy of the air mass in the plenum chamber. This is converted into mechanical energy by means of the turbine and finally into electrical energy by the generator.

Let us call P_e, the electrical power, and P_w the wave power, the overall efficiency of the system is given by

$$\eta = \frac{P_E}{P_W}. \tag{2.57}$$

Considering the P_U

$$\eta = \frac{P_E}{P_W}.\frac{P_U}{P_U} = \eta_W.\frac{P_E}{P_U}, \tag{2.58}$$

P_U being the useful hydrodynamic power and η_W the hydraulic efficiency, given by the ratio between P_U and P_W.

Multiplied and divided by P_A the (2.58) can be rewritten as

$$\eta = \eta_W . \frac{P_E}{P_U} . \frac{P_A}{P_A} = \eta_W \cdot \eta_A . \frac{P_E}{P_A}, \quad (2.59)$$

P_A being the reduced flow power and η_A the volumetric efficiency, given by the ratio between P_U and P_A. In particular P_A represents the pneumatic power excluding the power losses by the flow of air through the blades of the turbine.

Let us multiply and divide by the mechanical shaft power, P_M the second member of the (2.59) we obtain

$$\eta = \eta_W \cdot \eta_A . \frac{P_E}{P_A} . \frac{P_M}{P_M} = \eta_W \cdot \eta_A \cdot \eta_M . \frac{P_E}{P_M} = \eta_W \cdot \eta_A \cdot \eta_M . \eta_E, \quad (2.60)$$

with η_M the mechanical efficiency, given by the ratio between P_A and P_M and η_E the electrical efficiency, given by the ratio between P_M and P_E.

Hence the overall efficiency of the (2.57), can be rewritten as:

$$\eta = \eta_W \cdot \eta_A \cdot \eta_M . \eta_E . \quad (2.61)$$

2.3 The two-dimensional approach

2.3.1 The Navier Stokes equations

Fluid mechanics is essentially the study of fluids either in motion or at rest. CFD is particularly dedicated to the former, fluids that are in motion, and how the fluid flow behavior influences processes that may include heat transfer and possibly chemical reactions in combusting flows. The physical characteristics of the fluid motion can usually be described through fundamental mathematical equations, usually in partial differential form.

The multi-phase flow CFD simulation, in which both air and water flows have been assumed unsteady, was solved by the Navier-Stokes equations. These can be written using Cartesian tensor notation. This is an extremely useful tool for performing vector algebra. Consider the coordinate system

illustrated in Figure 2.11. Instead of using the typical axis labels x, y, and z, we use x_1, x_2, and x_3, or x_i, with i= 1,2,3.

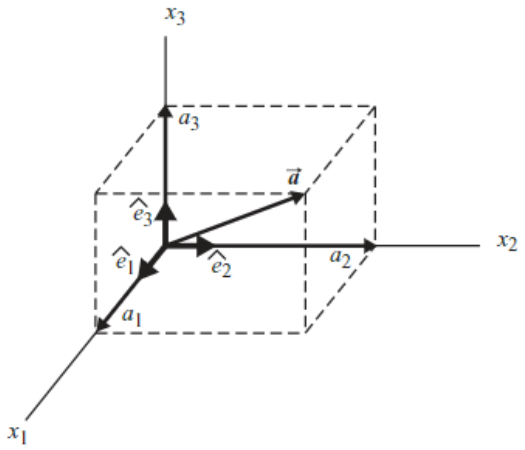

Figure 2.11 – Reference coordinate system.

The general form of the mass conservation equation, for incompressible as well as compressible flows, is

$$\frac{\partial \rho}{\partial t} + \frac{\partial}{\partial x_i}(\rho v_i) = 0. \tag{2.62}$$

The continuity equation (2.62) states that the mass is constant in a given system. Meaning that the amount of mass into the system is equal to the mass out of the system.

The equation of conservation of momentum in an inertial reference frame can be written in the form

$$\frac{\partial}{\partial t}(\rho v_i) + \frac{\partial}{\partial x_j}(\rho v_i v_j) = -\frac{\partial p}{\partial x_i} + \frac{\partial}{\partial x_j}\left[\nu\left(\frac{\partial v_i}{\partial x_j} + \frac{\partial v_j}{\partial x_i}\right)\right] + \frac{\partial}{\partial x_j}\left(-\overline{v_i' v_j'}\right), \tag{2.63}$$

where v_i and p are the time-averaged tensor velocity and pressure, respectively, and ν is the kinematic viscosity. The quantity

$$\tau_{i,j} = -\overline{v_i' v_j'}, \tag{2.64}$$

is known as the Reynolds stress tensor which is symmetric and thus has six components.

From Newton's second law, the total force is given as the rate of change of momentum. In a given system, the conservation of momentum means that the momentum into the system equals the momentum out of the system. In practice, this illustrates Newton's third law between fluid particles where an equal and opposite force will act on each particle in order to conserve the momentum.

The equations system (2.62 and 2.63) is not yet closed. In order to close, it must find enough equations to solve the unknowns. To solve the RANS equations there are several turbulence models. The most used models in CFD simulations are:

1) Boussinesq approximation;
2) Spalart-Allmaras model;
3) k-ω model;
4) k- ε model.

The Boussinesq approximation is a common method which employs the Boussinesq's hypothesis. It is at the heart of eddy viscosity models used in many different fields to model turbulent flows. This hypothesis corresponds to an alignment between Reynolds stresses and the mean velocity gradients as follow:

$$-\overline{v_i v_j} = 2\nu_T S_{ij} - \frac{2}{3} k\delta_{ij}, \tag{2.65}$$

where νT is the kinetic eddy viscosity and the turbulent kinetic energy, k, is defined as

$$k = -\frac{1}{2}\overline{v_i v_j} \tag{2.66}$$

and S_{ij} is the mean strain-rate tensor

$$S_{ij} = -\frac{1}{2}\left(\frac{\partial v_i}{\partial x_j} + \frac{\partial v_j}{\partial x_i}\right). \tag{2.67}$$

In the Spalart-Allmaras Model, the turbulent kinetic energy is ignored and the Reynolds stress is calculated as

$$-\overline{v_i v_j} = 2\nu_T S_{ij}, \tag{2.68}$$

The k-ω and k-ε are two equation models, which means, they include two extra transport equations to represent the turbulent properties of the flow. This allows a two-equation model to consider effects like the convection and the diffusion of turbulent energy. The first transported variable is turbulent kinetic energy, k. The second transported variable can be the turbulent dissipation, ε, or the specific dissipation, ω. These variables determine the scale of the turbulence, whereas the first variable, k, determines the energy in the turbulence. In this work, we used the k-ω turbulence model.

2.3.2 The discretization method

Discretization of the Navier–Stokes equations is a reformulation of the equations in such a way that they can be applied to computational fluid dynamics. The typical discretization methods used are:

4) Finite difference method.
5) Finite element method;
6) Finite volume method;

In the Finite Difference Method (FDM), the derivatives in the Partial Differential Equation (PDE) are approximated by linear combinations of

function values at the grid points. The error in the solution of this method is defined as the difference between the approximation and the exact analytical solution.

To use a finite difference method to approximate the solution to a problem, one must first discretise the domain of the problem. This is usually done by dividing the domain into a uniform grid (see Figure 2.12).

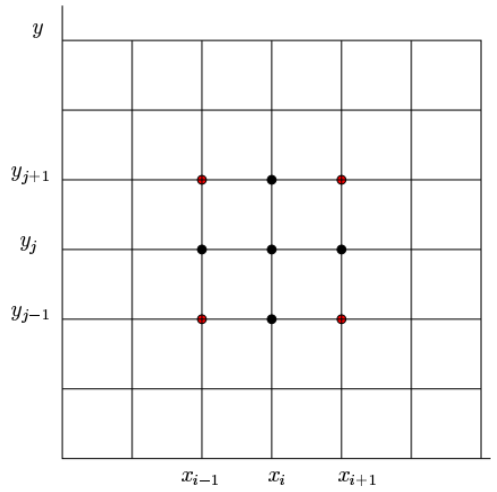

Figure 2.12- Uniform grid in which the domain can usually be discretized.

Note that this means that finite-difference methods produce sets of discrete numerical approximations to the derivative, often in a "time-stepping" manner.

Given the scheme of Figure 2.12 the central difference approximation to 1st order derivatives, on (x_i, y_i) node can be written by:

$$\frac{\partial f(x)}{\partial x} = \frac{f(x_{i-1}) - f(x_{i+1})}{2\Delta x}, \tag{2.69}$$

the backward difference approximation to 1st order derivatives is

$$\frac{\partial f(x)}{\partial x} = \frac{f(x) - f(x_{i-1})}{\Delta x}, \tag{2.70}$$

and the forward difference approximation to 1st order derivatives is

$$\frac{\partial f(x)}{\partial x} = \frac{f(x_{i+1}) - f(x)}{\Delta x}. \tag{2.71}$$

In contrast to Finite Difference techniques, the Finite Element Method (FEM) divides the solution domain into simply shaped regions, or "elements".

This subdivision of a whole domain into simpler parts has several advantages such as an accurate representation of complex geometry, inclusion of dissimilar material properties, the easy representation of the total solution and the capability to capture local effects.

An approximate solution for the PDE can be developed for each of these elements. The total solution is then generated by linking together, or "assembling," the individual solutions taking care to ensure continuity at the element boundaries. Thus, the PDE is satisfied in a piecewise fashion.

The implementation of the finite-element approach usually follows a standard step-by-step procedure. The first step involves dividing the solution domain into finite elements. Figure 2.13 provides examples of elements employed in one, two, and three dimensions. The points of intersection of the lines that make up the sides of the elements are referred to as nodes, and the sides themselves are called nodal lines or planes.

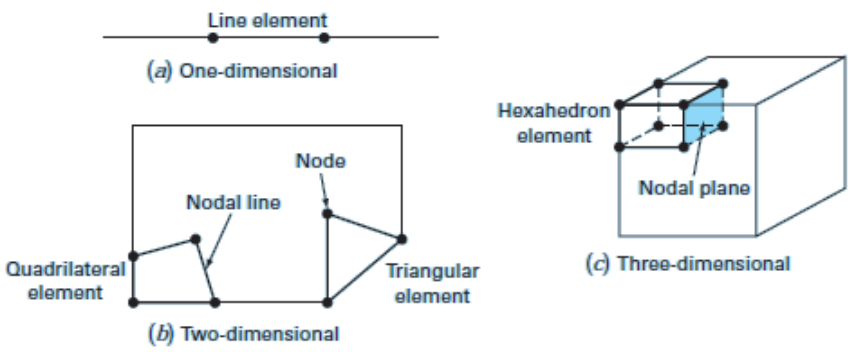

Figure 2.13- Examples of elements employed in (a) one, (b) two, and (c) three dimensional domains. (Steven C. Chapra & Raymond P. Canale, 1998).

The next step is to develop equations to approximate the solution for each element. This involves two phases. First, we must choose an appropriate polynomial function with unknown coefficients that will be used to approximate the solution. Secondly, we evaluate the coefficients so that the function approximates the solution optimally.

The polynomial approximation process eliminates all the spatial derivatives from the PDE, thus approximating the PDE locally with either a set of algebraic equations for steady state problems or, alternatively, with a set of Ordinary Differential Equations (ODE) for transient problems.

Algebraic equations are solved using numerical linear algebra methods, while ordinary differential equations are solved by numerical integration using standard techniques such as Euler's method or the Runge-Kutta method.

The Finite Volume Method (FVM) is similar to the finite difference method or finite element method. It is used to represent and evaluate PDE in the form of algebraic equations, and the values are calculated at discrete places on a meshed geometry. "Finite volume" refers to the small volume that surrounds each node point on a mesh. In the finite volume method, volume integrals in

a partial differential equation that contain a divergence term are converted to surface integrals, using the divergence theorem.

Referring to Figure 2.14,the first step in the finite volume method is to divide the domain into discrete control volumes. Let us place a number of nodal points in the space between W and E. The boundaries (or faces) of control volumes are positioned mid-way between adjacent nodes. Thus, each node is surrounded by a control volume or cell. It is common practice to set up control volumes near the edge of the domain in such a way that the physical boundaries coincide with the control volume boundaries.

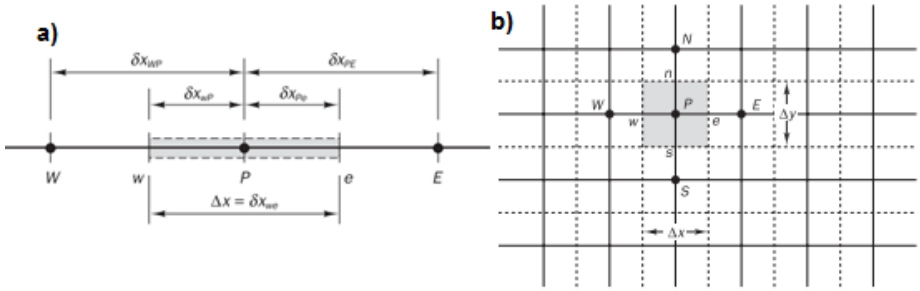

Figure 2.14 - The usual convention of CFD methods: a) the one-dimensional control volume width is $\Delta x = \delta x_{we}$, b) the two-dimensional control volume width is $\Delta x * \Delta y$ (Versteeg and W Malalasekera, 1995).

The key step of the finite volume method is the integration of the governing equation (or equations) over a control volume to yield a discretized equation at its nodal point P. Finally, after the discretization of the PDE in a system of linear algebraic equations, any matrix solution technique may be enlisted to resolve of the system.

2.3.3 Numerical CFD model

The numerical approach is based on a two-dimensional CFD simulation. There are two approaches for the numerical calculation of multiphase flows: the *Euler-Lagrange* approach and the *Euler-Euler* approach.

In the *Euler–Lagrange* models, grid-averaged equations for the continuous-phase flow field are solved, where the grid size is larger than the discrete phase size, while the discrete phase is explicitly tracked and experiencing forces in a Lagrangian fashion (Johan T.et al., 2015). The particle trajectories are computed individually at specified intervals during the fluid phase calculation.

In the *Euler–Euler* model, the different phases are regarded as continuum. Mathematically each phase is calculated by solving the balance equations.

To carry out the numerical experiment we used the *Euler-Euler* approach, implemented in the commercial code Ansys Fluent. In particular, we used the *volume of fluid* (VOF) model, in which two or more fluids (or phases) are not interpenetrating between each other. In the present case, VOF is used to model the air-water interface.

The maximum velocity of the air flow is reached at the slit located at the U-OWC roof. The Mach number being very low (nearly equal to 0.02), the air is assumed incompressible (For well-prepared initial data, the solutions of the full compressible Navier–Stokes–Maxwell system converge to that of the incompressible Navier–Stokes–Maxwell system as the Mach number tends to zero [Fucai Li and Yan-min MuLow, 2014]).

The volume fraction α of the i^{th} fluid occupying cells of the computation mesh is computed by

$$\frac{\partial \alpha}{\partial t} + \nabla(\alpha v_i) = 0. \qquad (2.72)$$

where the $0 < \alpha < 1$. If a cell is completely full of the considered fluid, $\alpha = 1$, if it is empty, $\alpha = 0$.

In each control volume, the sum of the volume fractions of all phases is equal to one (F.B. Ferreira et al., 2015). It is shown that the volume fraction

is more flexible and efficient than other methods for treating complicated free boundary configurations (C.W Hirt & B.D Nichols, 1981).

The *volume fraction* in cells that lie near the interface between two phases is calculated by a piecewise linear interpolation.

In order to accelerate the convergence of the solver by computing corrections on a series of coarse grid levels, we used a multigrid scheme. A multigrid cycle can be defined as a recursive procedure that is applied at each grid level, as it moves through the grid hierarchy. In particular, we have used the Algebraic Multigrid (AMG) method to obtain a converged solution.

In CFD techniques, the primitive variable method used to predict the flows could be divided into two groups: density-based methods and pressure-based methods, with the former used for compressible flows, and the latter for incompressible flows (J. F. Zhang et al., 2014). Here, we used a pressure-based solver for the discretization of the momentum and continuity equations.

In order to obtain the spatial discretization of the convection terms in the governing equations, we used the Green-Gauss Cell-Based method to gradient evaluation and the PRESTO! (PREssure STaggering Option) scheme for pressure equation. The other convection-diffusion equations (e.g. momentum or energy equation) were discretised by means of the Second Order Upwind scheme.

3 Wave generation and propagation of a wave train in a 2D flume

3.1 Transient waves generation

A general theory for mechanical wave generation was presented by Havelock (1929), and this is generally considered the foundation of wavemaker theory.

The most common way for a physical experimental flume to generate waves is through the movement of a paddle, which is located at one end of the flume. Paddles used in flumes can be a flap, a piston or a wedge type, of which the piston-type is the most popular permitting simple generation of shallow water waves according to the velocity pattern near the paddle (H.B. Gu et al., 2011).

As reported by Hughes (1993), the general, first order solution for sea surface elevation, resulting from a piston-type wavemaker starting from rest was described in 1949 by Kennard as

$$\eta(x,t) = \frac{2}{\pi}\int_0^\infty \int_0^t \int_{-d}^0 U_0(z,\tau)\frac{\cosh k(d+z)}{\cosh kd}\cos kx \cos\sigma(t-\tau)dzd\tau dk. \quad (3.1)$$

The free surface displacement η, produced in a wave flume by a piston-type wavemaker starting from rest and moving sinusoidally for a given period of time t, can be expressed in the form (Hughes, 1993):

$$\eta(x,t) = \frac{2}{\pi}\int_0^\infty \frac{\tanh kd}{k}\cos kx\left[\int_0^t U_0(\tau)\cos\sigma(t-\tau)d\tau\right]dk, \quad (3.2)$$

where d is the flume depth, U_0 is the horizontal velocity of the wave board, and $\sigma^2 = gk\tanh(kd)$, where $k=2\pi/\lambda$, λ being the length of the flume. Assuming that the board starts from rest at its extreme backward position, its displacement and velocity are given by

$$x(t) = -\frac{S}{2}\cos(\omega t), \tag{3.3}$$

$$U_o(t) = \frac{S}{2}\omega \sin(\omega t), \tag{3.4}$$

where S is the total horizontal stroke excursion and ω is the angular frequency of the wave board. Substituting eq. (3.4) into eq. (3.2), and integrating with respect to time, we obtain

$$\eta(x,t) = \frac{2}{\pi}\int_0^\infty \frac{\tanh kd}{k}\cos kx\left\{\frac{\omega}{\omega^2-\sigma^2}[\cos(\sigma t)-\cos(\omega t)]\right\}\mathrm{d}k, \tag{3.5}$$

As reported by Dean & Dalrymple (1984) a simplified theory for plane wavemakers in shallow water was proposed by Galvin (1964), who imposed that the water displacement by the wavemaker is equal to the crest volume of the propagating wave form. Considering a piston wavemaker with a stroke S, which is constant over a depth h, the volume of water displaced over a whole stroke is Sh (see Figure 3.1), whereas the volume of water in a wave crest is:

$$\int_0^{L/2} (H/2)\sin(kx)\mathrm{d}x, \tag{3.6}$$

equating the two volumes, we obtain

$$Sh = \frac{H}{k} = \frac{H}{2}\left(\frac{L}{2}\right)\frac{2}{\pi}\ , \tag{3.7}$$

where the $2/\pi$ factor represents the ratio between the shaded area and the area of the enclosing rectangle (see Figure 3.1). This equation can also be expressed as

$$\left(\frac{H}{S}\right)_{\text{piston}} = kh\,, \tag{3.8}$$

where H/S is the height-to-stroke ratio. This relationship is valid in the shallow water region, $kh<\pi/10$.

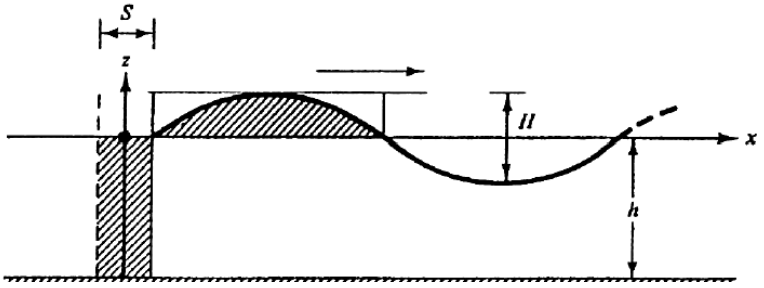

Figure 3.1 –Simplified shallow water piston-type wavemaker theory of Galvin [Dean & Dalrymple, 1984].

In Figure 3.2 the wave height to stroke ratio H/S, as a function of the relative depth of the flume is shown. The dotted lines represent the simplified wavemaker theory (eq.(3.8), in the case of the piston type).

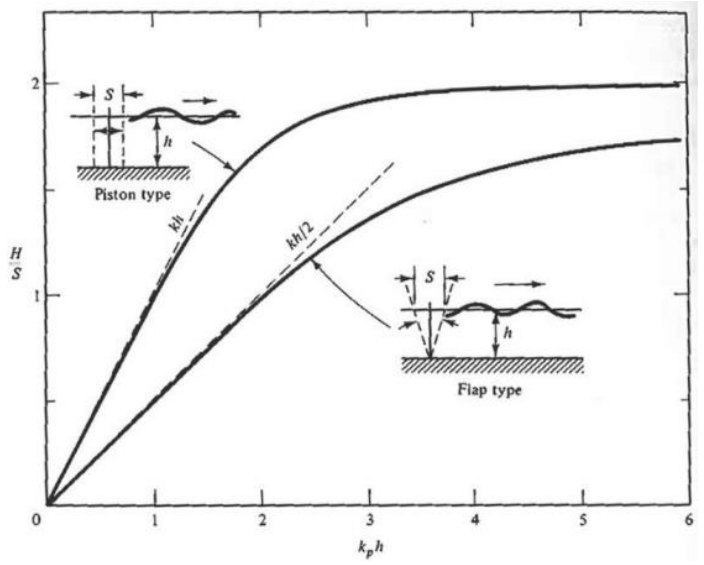

Figure 3.2 -Wave height to stroke ratios versus relative depths from plane wavemaker theory. Piston and flap type wavemaker motions [from Dean & Dalrymple, 1984].

3.2 First order waves

Referring to a two-dimensional reference frame *yz*, in which *y*-axis is the direction of wave propagation and *z*-axis is an upward orientated vertical axis, the system of differential equations of an irrotational two-dimensional flow with a free surface is:

$$g\eta+\left(\frac{\partial\varphi}{\partial t}\right)_{z=\eta}+\frac{1}{2}\left[\left(\frac{\partial\varphi}{\partial y}\right)^2+\left(\frac{\partial\varphi}{\partial z}\right)^2\right]_{z=\eta}=\frac{1}{\rho}f(t), \tag{3.9}$$

$$\left(\frac{\partial\varphi}{\partial z}\right)_{z=\eta}=\left(\frac{\partial\varphi}{\partial y}\right)_{z=\eta}\frac{\partial\eta}{\partial y}+\frac{\partial\eta}{\partial t}, \tag{3.10}$$

$$\frac{\partial^2\varphi}{\partial y^2}+\frac{\partial^2\varphi}{\partial z^2}=0, \tag{3.11}$$

$$\left(\frac{\partial\varphi}{\partial z}\right)_{z=-d}=0. \tag{3.12}$$

The first equation says that the pressure is zero on the free surface (atmospheric pressure being taken as reference pressure); it proceeds straightforwardly from the Bernoulli equation. The second one is the general equation of the free surface. The third and fourth ones are, respectively, the continuity equation and the boundary condition at the horizontal bottom.

The free surface displacement η and the velocity potential can be written respectively as

$$\eta(y,t)=\frac{H}{2}\cos(ky-\omega t) \tag{3.13}$$

$$\varphi(y,z,t)=g\frac{H}{2}\omega^{-1}\frac{\cosh[k(d+z)]}{\cosh(kd)}\sin(ky-\omega t)+\frac{1}{\rho}\int_0^t f(t')\,dt' \tag{3.14}$$

with $f(t)$, an arbitrary function of time. So the velocity potential (3.14)

(3.14) is not univocally specified. But the functions which are of interest, that is to say $\mathbf{v}(y,z,t)$ and $p(y,z,t)$, prove to be independent of $f(t)$ and thus they are univocally specified. In particular, the components of vector **v** prove to be

$$v_y(y,z,t) = g\frac{H}{2}\omega^{-1}k\frac{\cosh[k(d+z)]}{\cosh(kd)}\cos(ky-\omega t), \tag{3.15}$$

$$v_z(y,z,t) = g\frac{H}{2}\omega^{-1}k\frac{\sinh[k(d+z)]}{\cosh(kd)}\sin(ky-\omega t). \tag{3.16}$$

In Figure 3.3 we can see the velocity components for four phase position.

The pressure field associated with the progressive wave field (1.14) is determined from the Bernoulli equation (3.9). The result is

$$p(y,z,t) = -\rho gz + \rho g\frac{H}{2}\frac{\cosh[k(d+z)]}{\cosh(kd)}\cos(ky-\omega t), \tag{3.17}$$

(where the terms of order smaller than or equal to H^2 have been neglected), and hence the fluctuating pressure head proves to be

$$\eta_{ph}(y,z,t) = \frac{(p+\rho gz)}{\rho g} = \frac{H}{2}\frac{\cosh[k(d+z)]}{\cosh(kd)}\cos(ky-\omega t). \tag{3.18}$$

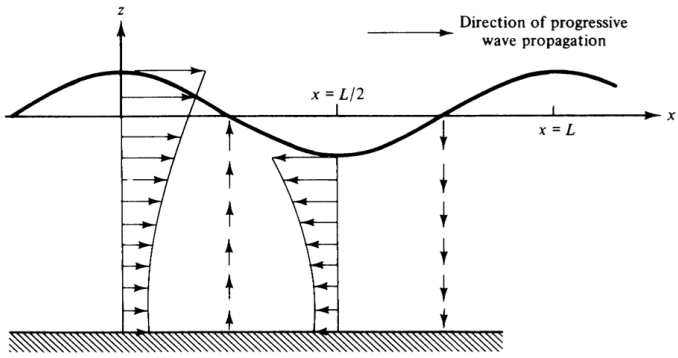

Figure 3.3 - Water particle velocity in a progressive wave (Dean and Dalrymple, 1984).

The first term on the right-hand of the pressure equation is the hydrostatic term, which would exist without the presence of the waves. The second term is due to waves and called the dynamic pressure. In Figure 3.4 the effect of the dynamic pressure in modifying the hydrostatic pressure is shown.

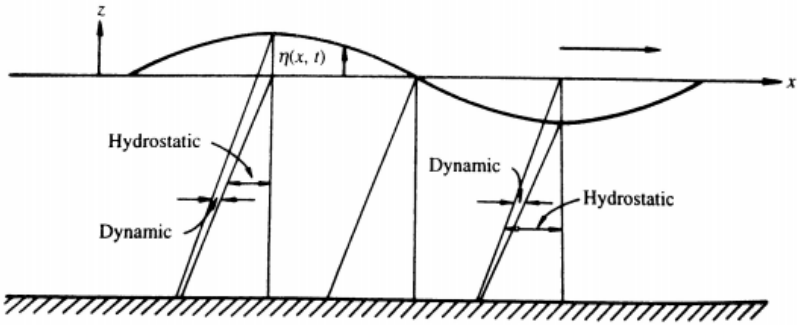

Figure 3.4 - Hydrostatic and dynamic pressure components at various phase positions in a progressive wave (Dean and Dalrymple, 1984).

Clearly the formulae of p and η_{ph} hold for $z \leq \eta$, and the formula of η_{ph} requires in addition z to be smaller than or equal to zero. Indeed eq.(3.18) presupposes that the static pressure is $-\rho g z$. To this purpose, note that, in the whole text, η_{ph} denotes the fluctuating pressure head only at points which are always beneath the water surface, where eq.(3.18) is, of course, valid.

3.3 Group celerity and wave power

Generally, wave motion implies energy travelling in the space-time domain. Treating surface water waves, the most used energy measure is the mean wave energy density per unit horizontal area. It is the sum of the kinetic and potential energy density integrated over the depth of the fluid layer and averaged over the wave phase.

The average (mean) energy density per unit area of gravity waves on the water surface is proportional to the wave height squared, according to linear wave theory:

$$E = \frac{1}{8}\rho g H^2 \tag{3.19}$$

where E is the mean wave energy density per unit horizontal area (J/m2). The potential energy density is equal to the kinetic energy, both contributing half of the total wave energy density E, as can be expected from the equipartition theorem. As the waves propagate, their energy is transported. The energy transport velocity is the group velocity. As a result, the wave energy flux, through a vertical plane of unit width, perpendicular to the wave propagation direction, is equal to

$$\phi = E\frac{c}{2}\left[1+\frac{2kd}{\sinh(2kd)}\right] \tag{3.20}$$

To explain the meaning of the group velocity C_G, we consider a long wave flume (see Figure 3.5) supposing that the wavemaker starts, from rest at time t=0. The time needed for the waves to get to a fixed point at a distance y_o from the wavemaker is t_o.

Considering a control volume extending from $y = 0$ (wavemaker) to $y = y_o$, during the time interval $0 < t < t_o$, the flow in the control volume is not periodic. Indeed, if we took some photographs at a regular time interval *T* (equal to the wave period) we would catch an evolving situation. Initially, we would see some waves close to the wavemaker with the rest of the tank still being calm.

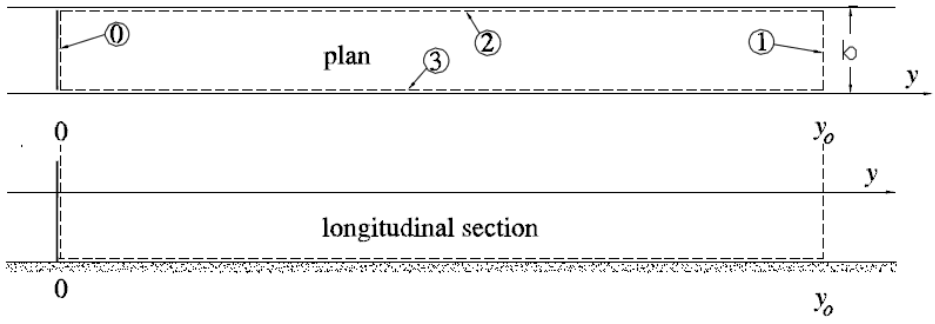

Figure 3.5 - Plan view and longitudinal section of a long wave flume. (Boccotti, 2000)

Then, we would see the wave zone widen gradually. Integrating the energy equation respect to *t* on the interval $(0, t_o)$, we obtain

$$\int_0^{t_o}\int_{\tilde{A}} (p+\rho e)\mathbf{v}\cdot\mathbf{n}\,\mathrm{d}A\,\mathrm{d}t = \left[\int_{\tilde{W}} \rho e\,\mathrm{d}W\right]_{t=0} - \left[\int_{\tilde{W}} \rho e\,\mathrm{d}W\right]_{t=t_o}, \qquad (3.21)$$

where $\tilde{A}$ is the lateral surface of the control volume and consists of four parts: the cross section ⓪ at the wavemaker; the cross section ① at y_o; and the two sides ② and ③ of the tank.

In detail, explicating the contributions of all cross sections, we arrive to

$$-t_o\, b\,\frac{1}{8}\rho g H^2\,\frac{c}{2}\left[1+\frac{2kd}{\sinh(2kd)}\right] = -by_o\,\frac{1}{8}\rho g H^2, \qquad (3.22)$$

and, simplifying and rearranging the term, we obtain

$$t_o = \frac{y_o}{\frac{c}{2}\left[1+\frac{2kd}{\sinh(2kd)}\right]}. \tag{3.23}$$

The quotient y_o/t_o being the propagation speed of a wave motion on a calm basin, we can write the group celerity as:

$$c_G = \frac{c}{2}\left[1+\frac{2kd}{\sinh(2kd)}\right] \tag{3.24}$$

Figure 3.6*a* shows three instant pictures of the wave tank taken an interval *T* from each other. The waves are sketched as vertical segments: the height of the segment is equal to the wave height and the interval between two consecutive segments is equal to the wavelength. Each single wave advances a wavelength *L* in a wave period *T*, so that its propagation speed is L/T (see the detail of the head of the group in Figure 3.6*b*). It is not so for the wave group which advances a wavelength in two wave periods, so that its propagation speed is $c/2$.

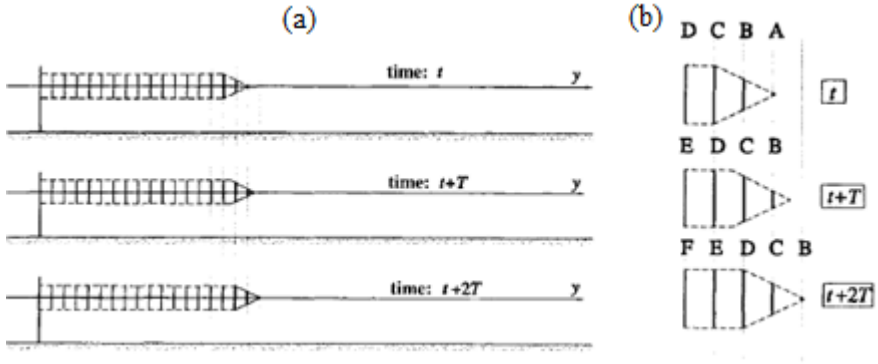

Figure 3.6 - (a) Three pictures taken a wave period from each other, while the wave motion advances on an initially still basin (the waves are sketched as vertical segments). (b) Details of the head of the group. [from Boccotti, 2000.]

The propagation speed of the group is smaller than the propagation speed of each single wave, simply because each single wave goes to die at the head of the group. In particular, in the first picture of Figure 3.6*b*, wave A is going to die; then in the third picture, two periods later, wave B is going to die; then it will be the turn of C, D and so on.

Therefore, known the group celerity, the mean energy flux of progressive waves can be written as:

$$\phi = \frac{1}{8}\rho g H^2 c_G \,. \tag{3.25}$$

3.4 Standing waves in front of a reflective vertical wall

Whenever a wave train attacks a vertical wall, we see a phenomenon of wave reflection.

If the direction of the incident waves makes an angle $\theta < \pi/2$ with the *y*-axis (wall-orthogonal), then the direction of the reflected waves makes an angle $\pi - \theta$ with the *y*-axis (see Figure 3.7).

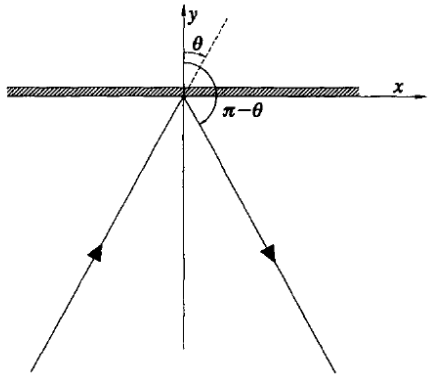

Figure 3.7 - Reflection: reference scheme. [Boccotti,2000.]

The flow field before the wall is given by the sum of incident and reflected waves:

$$\eta(x,y,t)=\frac{H}{2}\cos(kx\sin\theta+ky\qquad\cos\theta-\omega t)+$$
$$+\frac{\tilde{H}}{2}\cos(\tilde{k}x\sin\theta-\tilde{k}y\qquad\cos\theta-\tilde{\omega}t+\varepsilon)\qquad,\tag{3.26}$$

$$\phi(x,y,z,t)=g\frac{H}{2}\omega^{-1}\frac{\cosh[k(d+z)]}{\cosh(kd)}\sin(kx\qquad\sin\theta+ky\qquad\cos\theta-\omega t)+$$
$$+g\frac{\tilde{H}}{2}\tilde{\omega}^{-1}\frac{\cosh[\tilde{k}(d+z)]}{\cosh(\tilde{k}d)}\sin(\tilde{k}x\sin\theta-\tilde{k}y\qquad\cos\theta-\tilde{\omega}t+\varepsilon),\tag{3.27}$$

where it can be readily verified that both eqq. (3.26) and (3.27) satisfy Stokes' linear equations, that is to say the system consisting of the equations (3.9-12) with $f(t)=0$. Indeed, if a pair of functions η_1, ϕ_1 satisfy an homogeneous linear system, and a second pair of functions η_2 and ϕ_2 satisfy the same system, then the sum $\eta_1+\eta_2$, $\phi_1+\phi_2$ also satisfies this system of equations.

If the breakwater is along the line $y=0$ and is infinitely long, the boundary condition is

$$\left(\frac{\partial\varphi}{\partial y}\right)_{y=0}=0,\tag{3.28}$$

that is

$$H\omega^{-1}k\frac{\cosh[k(d+z)]}{\cosh(kd)}\cos(kx\qquad\sin\theta-\omega t)=$$
$$=\tilde{H}\tilde{\omega}^{-1}\tilde{k}\frac{\cosh[\tilde{k}(d+z)]}{\cosh(\tilde{k}d)}\cos(\tilde{k}x\qquad\sin\theta-\tilde{\omega}t+\varepsilon)\qquad,\tag{3.29}$$

and it must hold the *x, z* and *t*. Here, it is convenient to examine firstly the specific point $x = 0, z = 0$, where (3.29) is reduced to

$$H\omega^{-1}k\cos(\omega t) = \tilde{H}\tilde{\omega}^{-1}\tilde{k}\cos(\tilde{\omega}t - \varepsilon)\,. \tag{3.30}$$

Given that two cosine functions are equal to each other all over their domains, if and only if they have the same frequency, same amplitude and a phase angle of some integer multiple of 2π, it follows that (3.30) holds, for each *t,* if and only if

$$\left.\begin{array}{l}\tilde{\omega} = \omega \Rightarrow \tilde{k} = k \\ \tilde{H}\tilde{\omega}^{-1}\tilde{k} = H\omega^{-1}k\end{array}\right\} \Rightarrow \tilde{H} = H\,,$$

$$\varepsilon = n2\pi, n = 0,1,2,\ldots\,.$$

These observations are sufficient to conclude that the only way to satisfy the boundary condition (3.28) is that the height and frequency of the reflected waves must be equal to the height and frequency of the incident waves, and that the phase angle ε must be equal to $n2\pi$ with *n* any integer (in what follows we shall take it as zero). If the breakwater was not at $y = 0$, but at some parallel line, the conclusions would not change for what concerns height and frequency of the reflected waves, and the phase angle ε would be generally different from zero.

Since $\varepsilon = 0$, $\tilde{H} = H$, $\tilde{\omega} = \omega$ and $\tilde{k} = k$, the two functions (3.26-27) can be rewritten in the form

$$\eta(x, y, t) = H\cos(kx\sin\theta - \omega t)\cos(ky\cos\theta)\,, \tag{3.31}$$

$$\phi(x, y, z, t) = gH\omega^{-1}\frac{\cosh[k(d+z)]}{\cosh(kd)}\sin(kx\sin\theta - \omega t)\cos(ky\cos\theta) \tag{3.32}$$

In the basic case of $\theta = 0$, in which the wave attacks the breakwater orthogonally, the flow becomes two-dimensional *y-z*, and the formulae of η and ϕ reduce themselves to

$$\eta(y,t) = H\cos(\omega t)\cos(ky), \tag{3.33}$$

$$\phi(y,z,t) = -gH\omega^{-1}\frac{\cosh[k(d+z)]}{\cosh(kd)}\sin(\omega t)\cos(ky), \tag{3.34}$$

and hence the velocity components are

$$v_y(y,z,t) = gH\omega^{-1}k\frac{\cosh[k(d+z)]}{\cosh(kd)}\sin(\omega t)\sin(ky), \tag{3.35}$$

$$v_z(y,z,t) = -gH\omega^{-1}k\frac{\sinh[k(d+z)]}{\cosh(kd)}\sin(\omega t)\cos(ky). \tag{3.36}$$

Stationary waves do not transfer energy from one place to another. Instead, they "store" their energy in one place. Stationary waves are formed when two progressive waves with the same frequency and similar amplitudes, travelling in opposite directions, interfere with each other.

As with the velocities under a progressive wave, these velocities increase with elevation above the bottom. The extreme values of horizontal and vertical velocity in space occur under the nodes and antinodes of the water surface profile. As we can see in Figure 3.8 the horizontal and vertical velocity are zero under antinodes and nodes respectively.

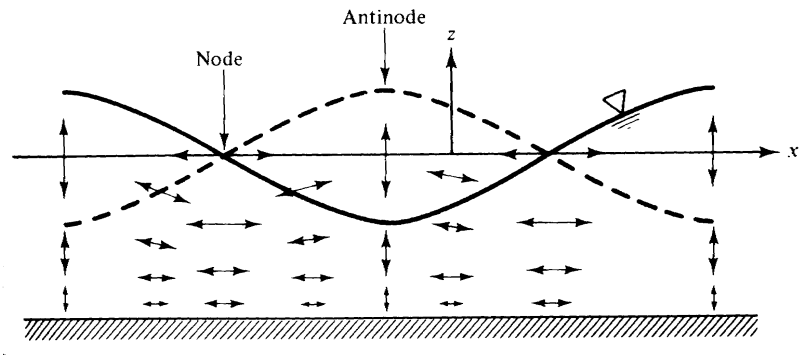

Figure 3.8 - Distribution of water particle velocities in a standing wave. [Dean & Dalrymple, 1984.]

The wave height at the antinodes is $2H$ (we mean the height of the wave in the time domain), that is twice the wave height that would be there without the wall. Also, the velocity maximum is twice the maximum in absence of the wall.

The pressure distribution on the wall, whatever the angle θ of the waves, according to Stokes' first order, is given by

$$p(z) = -\rho g z + \rho g H \frac{\cosh[k(d+z)]}{\cosh(kd)}, \tag{3.37}$$

which proceeds from equation (3.32)

of φ, and may be rewritten in the equivalent form (apart from some terms of order H^2):

$$p(z)\begin{cases} = -\rho g z + \rho g H \dfrac{\cosh[k(d+z)]}{\cosh(kd)} & \text{if} \quad z \le 0, \\ = \rho g (H - z) & \text{if} \quad 0 \le z \le H. \end{cases} \tag{3.38}$$

The wave pressure, that is the difference of (3.38) and the static pressure, is shown in Figure 3.9*a*.

Figure 3.9*b* shows Saintflou's model (1928). According to this model, we have to evaluate the two extremes of pressure distribution, that are

(i) the elevation where the pressure becomes zero, which is the highest elevation reached by the water surface;

(ii) the pressure at the lowest point of the wall.

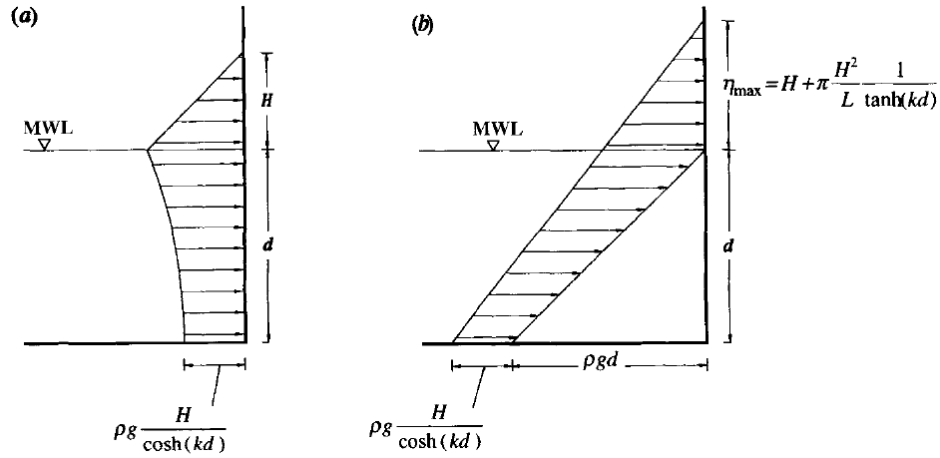

Figure 3.9 - The pressure exerted on an upright breakwater by a wave crest: (a) Stokes' linear theory; (b) Saintflou's model. [Boccotti, 2000.]

4 Set up of the wave flume

4.1 Layout of the experiment

The numerical approach is based on a two-dimensional CFD simulation using the Euler-Euler approach, implemented in the commercial code Ansys Fluent 17.0, Academic Version. We used the volume of fluid (VOF) model to represent the air-water interface.

A preliminary check has been carried out by considering a vertical reflecting wall instead of the absorbing wall. The computational domain (see Figure 4.1) is a wave-flume having a piston-type wavemaker placed on the left extremity and a vertical breakwater on the right extremity of the contour. The water depth and the dimensions of the wave-flume are indicated in Figure 4.1.

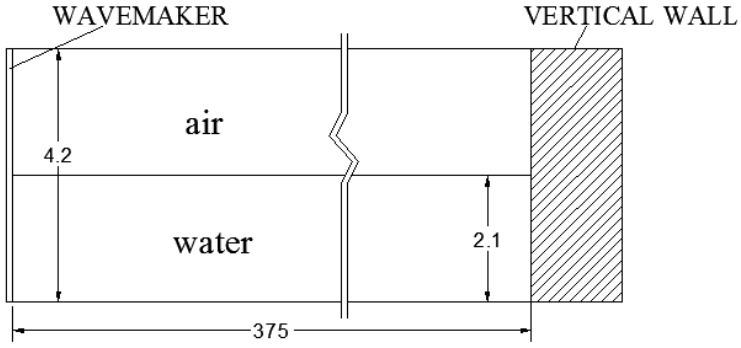

Figure 4.1- The computational domain of the wave flume. The wavemaker is on the left side. On the right, a reflecting vertical wall for carrying out preliminary tests (measures are in meters) is considered.

The distance between the wavemaker and the wall is 375 m; the flume water depth is 2.1 m. The length of the flume has been chosen in order to have many wave lengths before the wall where the stationary condition of the wave motion is established after the wave's reflection by the wall.

The numerical experiment has been carried out by substituting the vertical wall with the U-OWC (see Figure 4.2). The plant shown, has the same size as the plant tested at sea by Boccotti et al (2007). Due to the two-dimensional scheme, the circular air tube is substituted by a slit 4.2 cm wide.

As we can see, the U-OWC is the same as the small-scale breakwater built in the natural laboratory of Reggio Calabria (Boccotti et al., 2007). It is the 1:10 scale model (with some modifications) of a hypothesis of a breakwater for the North-East Pacific coast or a 1:6 scale model of a breakwater suited for the Mediterranean Sea.

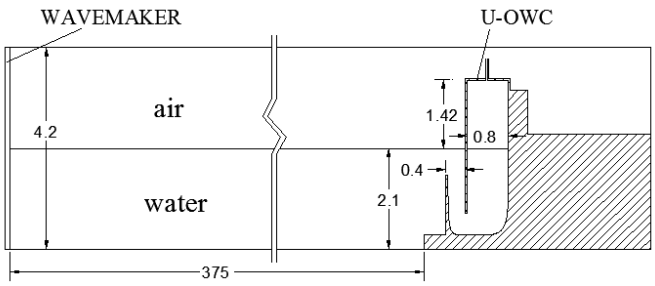

Figure 4.2 - Sketch of the computational domain with a U-OWC breakwater instead of the vertical wall considered in Figure 4.1[measures are in meters].

As we can see in Figure 4.3, in all the computational domains we have used the laminar model, except inside the plant where a turbulence model has been implemented.

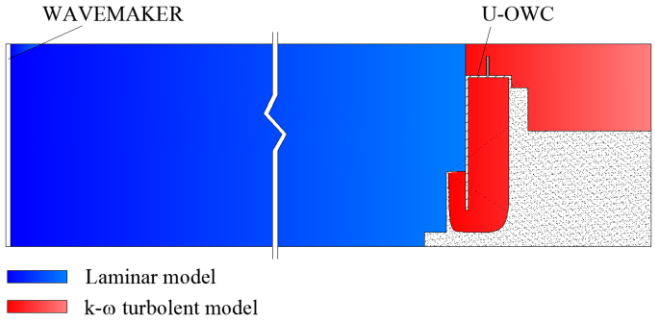

Figure 4.3 - Sketch of the computational domain with a U-OWC breakwater. In blue is the domain in which we use a laminar model, in red is the domain with a turbulent model.

4.2 Wave generation by a piston type wavemaker

There are many types of wave generating devices; they may be classified in two general categories, active and passive. The active generator consists of mechanical devices of various sorts displacing the water in direct contact with the generator. By controlling the movement of the device, the wave form is created. On the other hand, the passive wavemakers have no moving parts in contact with the water. They use air pressure to generate oscillations of the water (S.K. Chakrabarti, 1994).

In Figure 4.4, various types of active and passive generators proposed by Ploeg and Funke (1980) are shown.

The wave-flume has a piston-type wavemaker placed on the left extremity of the computational domain. Starting from rest, the wave generation process has been simulated assigning the velocity [eq. (3.4)] to the left wall of the wave flume, by means of a User Defined Function (UDF).

In Figure 4.5 the code to specify the motion of the rigid body (wavemaker) in the dynamic zone is shown.

The Fluent dynamic mesh feature has been used for both the wall motion and the deformation of the neighboring cells. The dynamic mesh model can be used to model single or multiphase flows where the shape of the domain is changing with time due to motion on the domain boundaries. The motion can be a prescribed motion, specifying the linear and angular velocities or can be chosen through the User Define Function. To use the dynamic mesh model, it needs to provide a starting volume mesh and the description of the motion of any moving zones in the model.

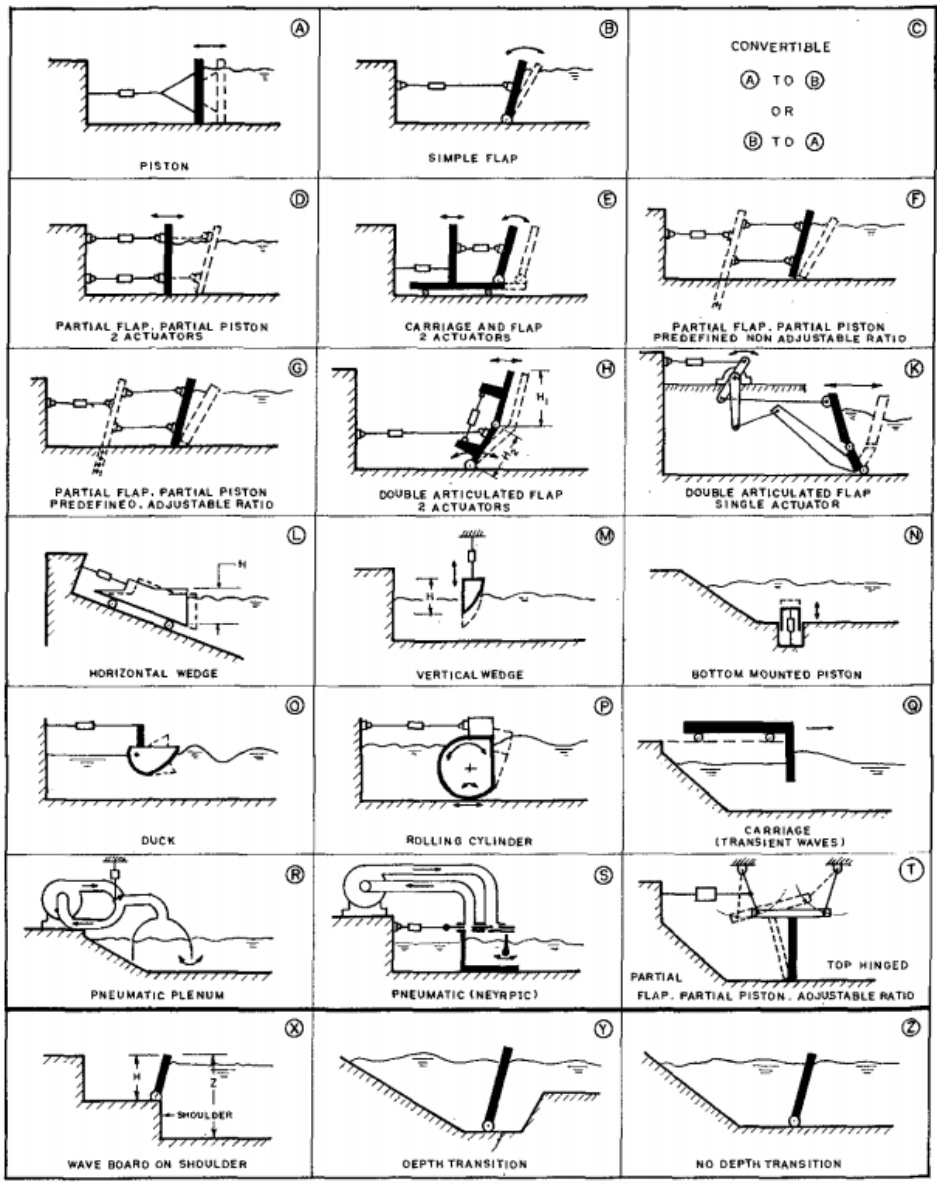

Figure 4.4 – Variety of wave generator schematics (Ploeg & Funke, 1980). All wavemakers are active type except for the types R and S.

```
/************************************************************/
/*DEFINE_CG_MOTION*/
/* macro to specify the motion of a particular dynamic zone*/
/* with the linear and angular velocities at every time step*/
/************************************************************/

/************************************************************/
/*1-degree of freedom equation of motion (x-direction)*/
/************************************************************/

#include "udf.h"
 real ds = 0.213; /*maximum displacement of piston-type wavemaker (m)*/
 real g = 9.806;
 real T = 3.5;    /*wave period (sec)*/

DEFINE_CG_MOTION(onda, dt, vel, omega, time, dtime)
/* There are six arguments to DEFINE_CG_MOTION*/
/* name, dt, vel, omega, time, and dtime*/
/*The current time and time step are time and dtime, respectively */

{
    real pi = 4.*atan(1.);
    real L = g*T*T/(2.*pi);      /* wavelength (m)*/
    real om = 2.*pi/T;         /* angular frequency */

Thread *t;
face_t f;

/*ct = current_time */

 real ct =  RP_Get_Real("flow-time");

/*get the thread pointer for which this motion is defined*/

t = DT_THREAD(dt);

/* set x-component of velocity*/

 vel[0] = 0.5*ds*om*sin(om*ct);

}
```

Figure 4.5– The User Define Function (UDF), to specify the motion of the wavemaker in Fluent.

We generated a set of wave trains with periods ranging in the time interval $3.5<T<9$. The wave height for all generated waves was fixed at $H = 0.2$m and the water depth d, is equal to 2.1 m. The time step for the numerical integration was set at 1/1000 of wave period.

At the end of each time step, the water surface inside the wave flume has been recorded, allowing us to analyze the wave motion in depth.

4.3 The mesh discretization

The initial phase of any numerical simulation begins with the discretization of the calculation domain in a suitable mesh.

The major data structures of meshes typically used are shown in Figure 4.6. In particular, we can see a structured mesh (Fig.4.6 *a*), an un-structured mesh (Fig.4.6 *b*), and hybrid grid (Fig.4.6 *c*).

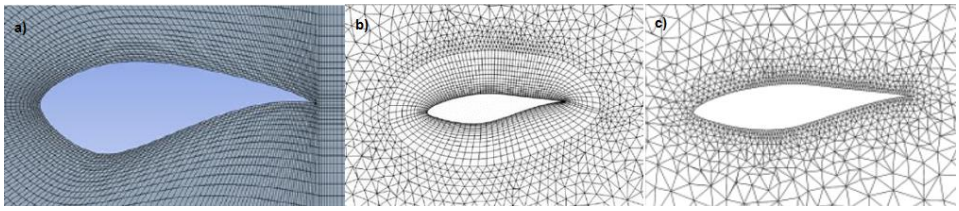

Figure 4.6 – Example of mesh classification: a) structured mesh, b) unstructured mesh, c) hybrid grid.

Structured grids are identified by regular connectivity. The possible element choices are quadrilateral in 2D and hexahedra in 3D.

An unstructured grid is identified by irregular connectivity. The most prevalent techniques for generating unstructured meshes are the advancing-front method, and Delaunay-based approaches. While the advancing-front method is somewhat heuristic in nature, Delaunay-based methods are firmly rooted in computational geometry principles (D. J. Mavriplis, 1997).

In the advancing-front technique an unstructured mesh is generated by adding individual elements one at a time to an existing front of generated elements. Generation of a two-dimensional grid begins with a discretization of the geometry boundaries as a set of edges. These edges form the initial

front that is to be advanced out into the field. A particular edge of this front is selected, and a new triangle is formed with this edge as its base, by joining the two ends of the current edge either to a newly created point, or to an existing point on the front. The current edge is then removed from the front, since it is now obscured by the new triangle. Similarly, the remaining two edges of the new triangle are either assigned to the front or removed from the front, depending on their visibility, as shown in Figure 4.7.

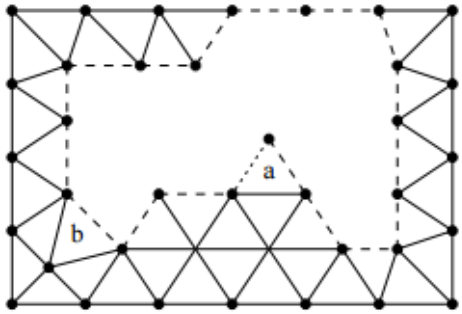

Figure 4.7 – Generation of a new triangle using new point (a), or existing front point (b), in the advancing-front method. Dashed line edges denote current front (D. J. Mavriplis, 1997).

Given a set of points in the plane, many possible triangulations of these points exist. A Delaunay triangulation in R^2 is defined by the condition that all the nodes in the mesh are not interior to the circles defined by the three nodes of each triangle, as shown in Figure 4.8 *a* (C. Aricò et al., 2013). Figure 4.8 *b* shows a triangulation in which the Delaunay property is not satisfied.

In other words, a Delaunay triangulation of a vertex set is a triangulation with the property that no vertex in the vertex set falls in the interior of the circumcircle (circle that passes through all three vertices) of any triangle in the triangulation. A hybrid grid contains a mixture of structured portions and unstructured portions. It integrates the structured meshes and the unstructured meshes in an efficient manner. Structured grids generally lead to fast and accurate flow solvers and are therefore preferred where the cost of

generating the grid is not excessive. For situations where the complexity of the domain is such that grid generation is very expensive and where the user can live with modest accuracy, unstructured grids are generally used.

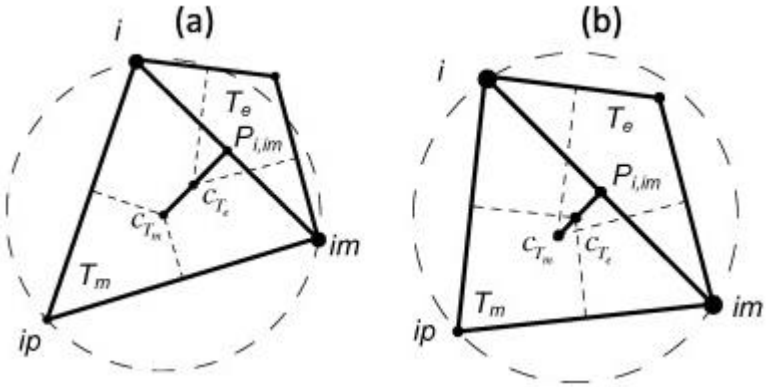

Figure 4.8 – The Delaunay condition: (a) triangles Tm and Te satisfy Delaunay condition; (b) triangles Tm and Te do not satisfy Delaunay condition (C. Aricò et al., 2013)

In this work, the mesh was created by the ANSYS Meshing application which implements two meshing algorithms: *patch conforming* and *patch independent*. The first is the most common and it is a meshing technique in which adjacent elements share common boundaries (edges and vertices), defined by the same nodes. The second is a meshing technique in which the adjacent elements are not necessarily respected unless there is a boundary condition. In this technique, the vertices are not necessarily conformed. Figure 4.9 shows the algorithm comparison; in particular, panel *a* shows the details captured by the patch conforming algorithm and panel *b* shows the details ignored by the second algorithm.

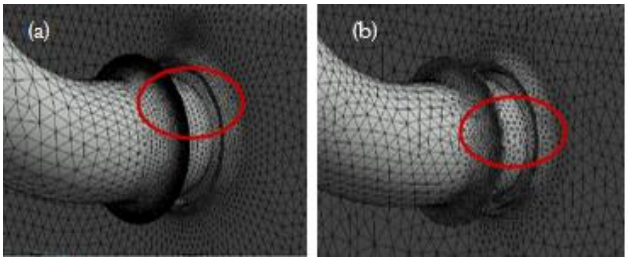

Figure 4.9 – The comparison between the patch confirming (a) and patch independent algorithm (b).

Non-conforming meshes are typically used to allow for the partial adaptive refinement of a finite element mesh, such as at locations of stress concentration or steep gradients, without imposing a high computational cost in areas where such a refinement is not needed (G. Haikal and K.D. Hjelmstad, 2010). Figure 4.10 shows the comparison between the conformal and non-conformal meshes.

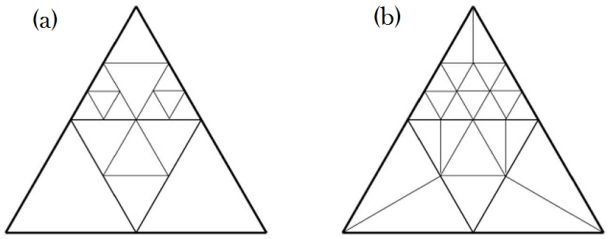

Figure 4.10 – The comparison between the non-conformal (a) and conformal meshes(b).

In this work, we use the *patch conforming* algorithm and *all triangles* mesh method. The size of mesh is variable according to geometrical needs. In particular, we adopted a ticker mesh near the REWEC edges than elsewhere in the domain. The slit on the roof of the air chamber required the smallest triangles, being only 0.042 m wide. Therefore, along the flume (both in the water and in the air) the maximum size of the triangular elements reaches 7 cm. While, within the slit the minimum size is 7 mm.

A different reasoning concerns the water-air interface, as we can see in Figure 4.11, which shows the conformal mesh adopted for the computational domain of Figure 4.1.

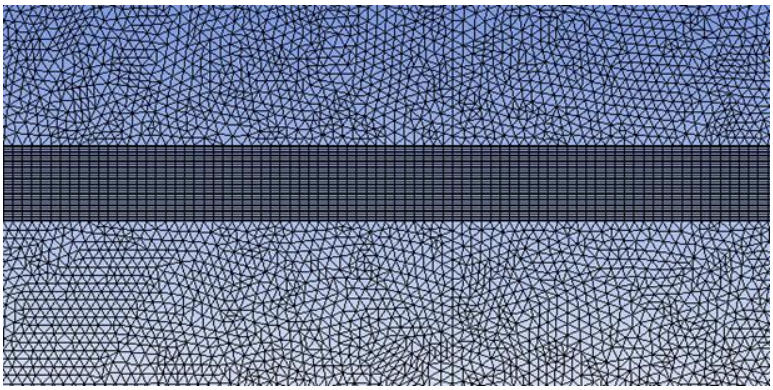

Figure 4.11 - The conformal mesh adopted for the computational domain of Figure 4.1.

As we can see, near the air-water interface the mesh adopted is rectangular. This choice is made to achieve a better resolution of the instantaneous free surface displacement. As shown in Figure 4.12, a conformal mesh in the proximity and inside the U-OWC was created (i.e. built from various geometrical bodies that form a single part). The size of the triangular elements and the thickening in the proximity of the water-air interface is the same as that used for the reflecting wall.

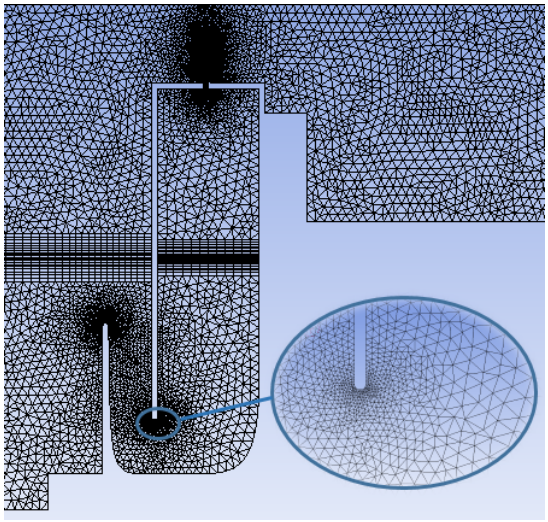

Figure 4.12-The conformal mesh adopted in the proximity and inside the U-OWC.

In order to match the behavior of a physical wave tank, we have to set the boundary conditions of the numerical wave tank. Smooth no-slip wall boundary conditions have been assigned to all solid walls, whilst the upper domain boundary is defined as a pressure outlet with zero-gauge pressure.

5 Validation of generated waves in the space-time domain

5.1 Transient waves

In order to validate the numerical experiment, we carried out some preliminary tests on the numerical wave flume. Figure 5.1 shows four pictures of the free surface elevation $\eta(y,t)$, taken at some wave period from each other. The considered time instants are $5T$, $15T$, $40T$ and $60T$, ranging from panel (a) to (d). The dashed vertical line marks the distance y_0 ($=9L$) from the wavemaker. As we can see, at $t = 5T$, the wave train has not yet reached the abscissa y_0. After $15T$, the head of the group has passed y_0, and the wave motion is periodic until the waves reflected by the vertical wall (see panel c) reach y_0 (see panel d).

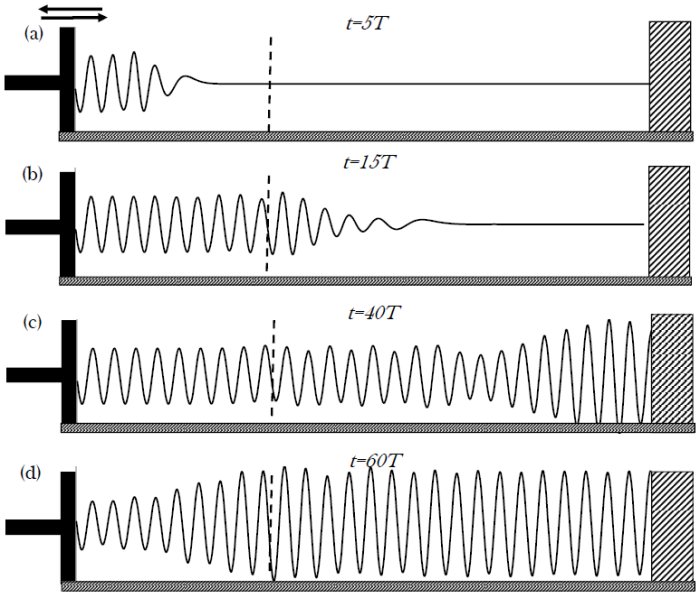

Figure 5.1- Four pictures of free surface elevation in a long wave flume with a wavemaker at the left extremity and a vertical wall on the right (H=0.20m, T=3.5s).

To test the wave generation and propagation in the flume, the $\eta(y,t)$ generated numerically, has been compared with the analytical solution. Figure 5.2 shows this comparison at $t=5T$. The dashed line is that of Figure 5.1 (a), the continuous line is obtained through eq (3.5). The good agreement is not limited to the η, in fact, as we can see in Figure 5.3, it also holds for the fluctuating pressure head, η_{pb}. In particular, Figure 5.3a shows the comparison in the time domain between a sinusoidal wave and the numerical solution obtained at three wavelengths ($y=3L$) from the wavemaker. As evident, we have the typical profile of a progressive wave, in that the recording portion is taken inside the interval [$10T$, $40T$] (see Figure 5.1).

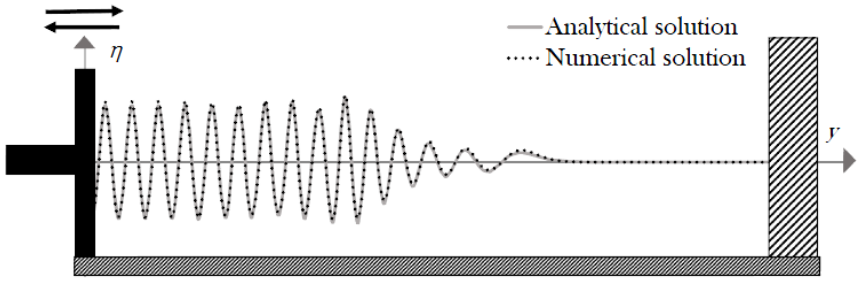

Figure 5.2 - Comparison between the analytical solution for transient waves in a flume (Huges,1993) and numerical solution carried out by the preliminary experiment (H=0.20m, T=3.5s).

Figure 5.3b shows the η_{pb} in front of the vertical wall after the incident waves have been reflected by the wall itself. For comparison, the analytical solution of standing waves in front of a reflecting wall is shown (the continuous line). As we can see, there is a good agreement between theory and numerical simulations.

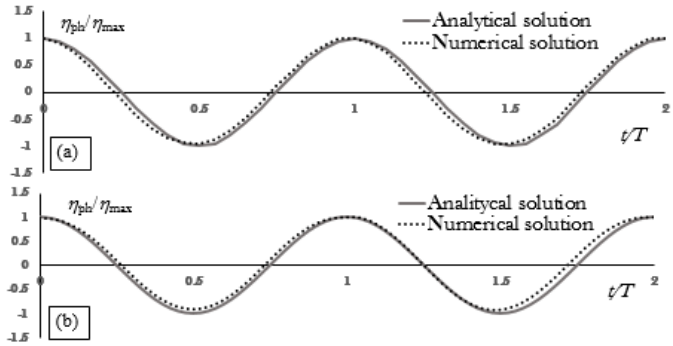

Figure 5.3 - Dimensionless fluctuating pressure head in the time domain at 1 m below the free surface: (a) at the distance $y = 3L$ away from the wavemaker; (b) on the breakwater wall. The continuous lines represent analytical solutions; the dashed lines have been obtained with numerical simulations.

5.2 The progressive wave field

Figure 5.4 shows several snapshots of the surface waves in the flume taken every $T/20$, during the 14th period of the simulation (i.e. $t=t_i=14T+iT/20$, i:1, 2, ….19). As we can see, the successive wave profiles form an envelope typical of a progressive wave field.

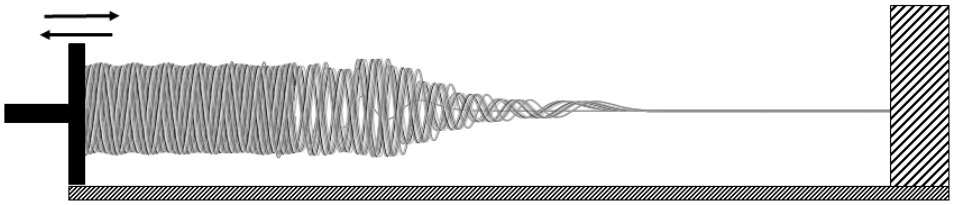

Figure 5.4 - Several snapshots of the surface waves (H=0.20 m, T=3.5 s) from 14T to 15T.

The wave height is practically constant in the tail of the wave train (near the wavemaker) and it reduces gradually to zero at the head of the wave train. The waves are generated at the moving wall, then they move towards the head of the wave train with a speed equal to the wave celerity c. The envelope advances with a speed C_G, less than c ($c_G=c/2$, in deep water). C_G is named celerity group (see Sect. 3.3)

To check the cinematism of the waves field we make a comparison with the analitical solution of a progressive wave in the Airy limit of small amplitude waves [eq. (3.17)]. The wave pressure distribution along a vertical section is shown in Figure 5.5. Four time instants have been considered: t=0=crest; t=T/4=zero down-crossing; t=T/2=trough; t=3T/4=zero up-crossing.

The results show that there is a suitable correspondence between analytical and numerical simulation and this confirms that the wave field expanding along the wave flume has the characteristics of a progressive wave. As confirmation, we can look at the velocity wave field shown in Figure 5.6. The meaning of both points and curves is the same as Figure 5.5. In addition, the considered abscissa is the same in the two figures. The theoretical horizontal velocity is calculated by means eq. (3.15), the vertical one, with the eq. (3.16).

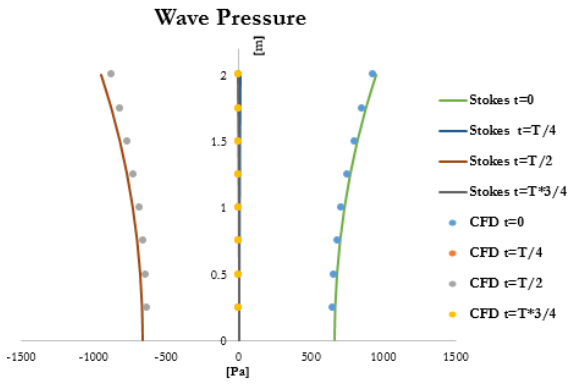

Figure 5.5- Wave pressure distribution along a vertical section at 3L distance from the wavemaker. Points have been obtained through CFD. Lines, through first order Stokes' theory.

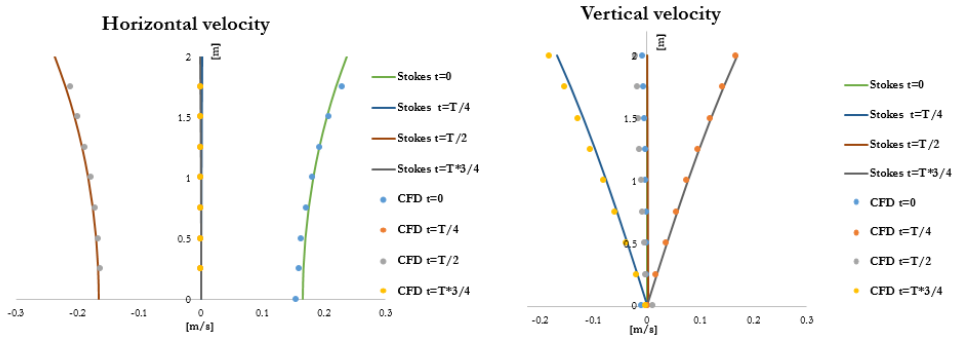

Figure 5.6- Horizontal and vertical velocity distribution along vertical sections at 3*L* distance from the wavemaker. Points have been obtained through CFD. Lines, through first order Stokes' theory.

5.3 The standing wave field

The progressive wave train propagating in the wave flume impacts on a vertical wall and is reflected backwards. The reflected wave train superimposed with the incident waves generates a standing wave field propagating from the breakwater towards the wavemaker.

Figure 5.7 shows the overlapping of several snapshots of the instantaneous surface elevation in the flume. Each frame is taken every $1/20T$ during a time interval of a wave period.

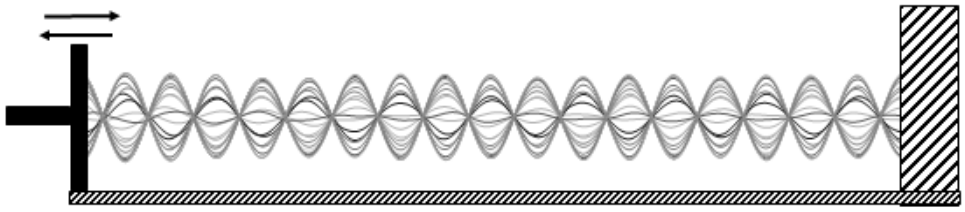

Figure 5.7 – Superimposition of 20 snapshots of the water surface, taken regularly during a time period equal to *T* (*H*=0.20m, *T*=3.5s).

Figure 5.8 shows a standing wave field. In particular, we can see the characteristic "nodes" at $y = (2n+1)\ L/4$ (n=0,1,2,..), where the free surface displacement is zero whatever the time instant is.

As we described in paragraph 3.4, standing waves, unlike progressive ones, do not transfer energy from one place to another. The envelope of waves of Figure 5.8 is the same as shown in Figure 3.8 obtained through the analytical solution.

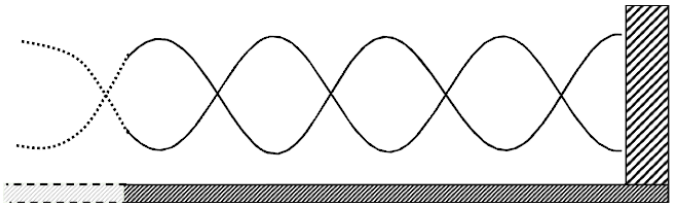

Figure 5.8 – The envelope of waves shown in Figure 5.7.

Figure 5.9 shows four snapshots of free surface elevation η, in front of the wall. Panel (a) shows free surface elevation at $t = t_0$ and panels (b), (c) and (d), represent η at subsequent instants $t_0 + iT/4$ (i=0,1,2,3). At t_0 and $t_0 + T/2$, the vertical displacement is at its maximum (except in nodes). At $t_0 + T/4$ and $t_0 + 3T/4$, η is nearly equal to zero in all the flume.

The stationarity of the wave field is confirmed also by distributions of horizontal velocity v_y, along some fixed vertical sections (see Figure 5.1). At time instants t_1 and t_3, $v_y = 0$, everywhere. For $t = t_2, t_4$, $v_y = 0$ at vertical sections y_2, y_4; and are maxima (in absolute value) at y_3 and y_1. For comparison, the v_y calculated with the analytical solution (points) is also shown in Figure 5.10.

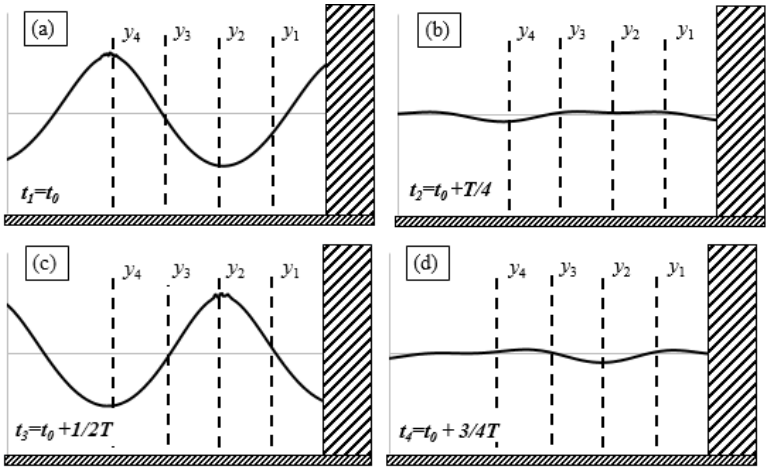

Figure 5.9 - Four snapshots of the free surface elevation in front of the vertical reflecting breakwater, taken every $T/4$ of time interval.

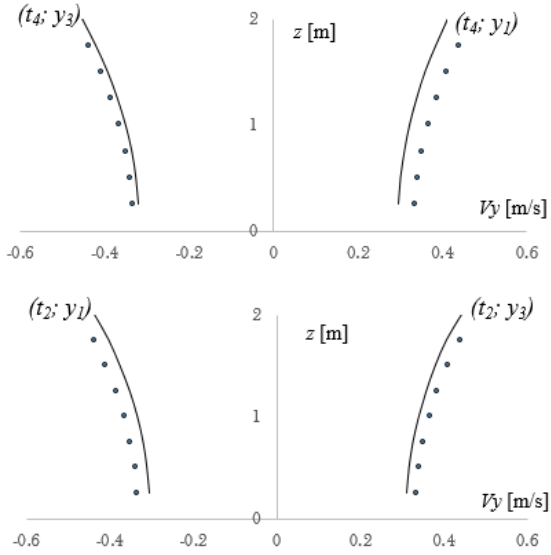

Figure 5.10 - Horizontal velocity distribution along vertical sections y_1 and y_3 for the snapshot (b) and (c) of Figure 5.9. Comparison between analytical (dashed line) and numerical (continuous line).

5.4 Wave energy propagation along the flume

The wave dimensions for all proceeding worked examples are: H= 0,2m; T= 3,5 s. Starting from rest, the wave train takes about 90s (about 25T) to hit the wall posed at the opposite site of the flume. Therefore, the runtime of the

simulation was set to 196s (t=55 T), enough to represent the evolution of the wave field before the U-OWC.

Figure 5.11 shows a time series of the non-dimensional pressure fluctuation Δp and discharge Qp at 3L from the wavemaker, as a function of t/T, in the time interval $10T < t < 15T$.

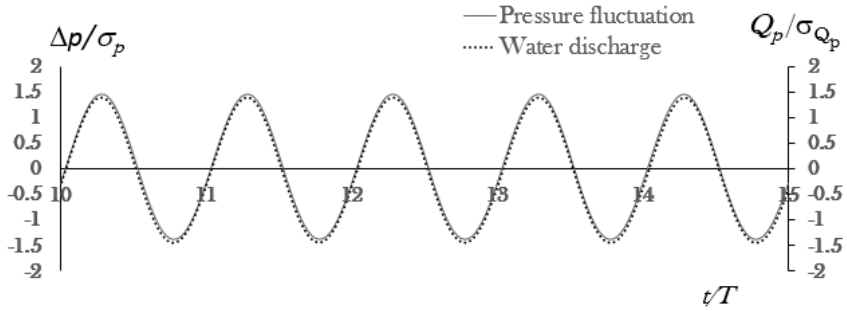

Figure 5.11- Pressure fluctuation Δp and discharge Qp at 3L distance from the wavemaker, as a function of t/T. Values have been divided by their own standard deviation σ.

The wave energy flux $\Phi_{in}(t)$ crossing instantaneously the fixed vertical section is given by

$$\Phi_{in} = \int_{-d}^{\mu} \Delta p(t) v_y(t) \mathrm{d}z \,, \qquad 5.1$$

and it is represented in Figure 5.12, in the same time interval shown in Figure 5.11. The mean energy flux is 140 W/m. It is 12% less than the value calculated by means of eq. (3.25) with measured values of H and T in the flume.

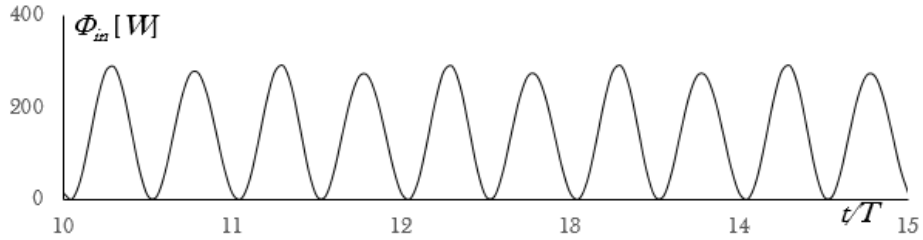

Figure 5.12 - The instantaneous energy flux versus time of incident waves, at a distance y=3L.

InFigure 5.13, some snapshots of envelopes of surface waves propagating along the wave flume, are shown at different time instants. At the time instant t=0 the wavemaker starts to move. As we can see, a wave group advances along the wave flume, as said before, the wave energy advances at the same velocity as the wave train, that is the group celerity C_G. To estimate C_G, we sight the position assumed by the base of the head of the train along the flume at subsequent time instants. In the first snapshot (t=3T) the group has covered about 1/13 of flume length and the head of the group is at a distance of 2.2 L from the wavemaker. Likewise, in Figure 5.13b the head of the group is at 4.7 L from the wavemaker at t=7T; (snapshot c) at t=12T, finally, the group is at y= 8.7L and then in the last snapshot (at t=18T) the basis of the head of the group is at abscissa y= 12.7L.

The average group celerity, evaluated as the ratio $\Delta y/\Delta T$, is equal to 2.78 m/s. The theoretical C_G, calculated by means of (3.24) is 12% more than the numerical one. This difference is due to numerical errors seen in the ΔP_p and Q_p.

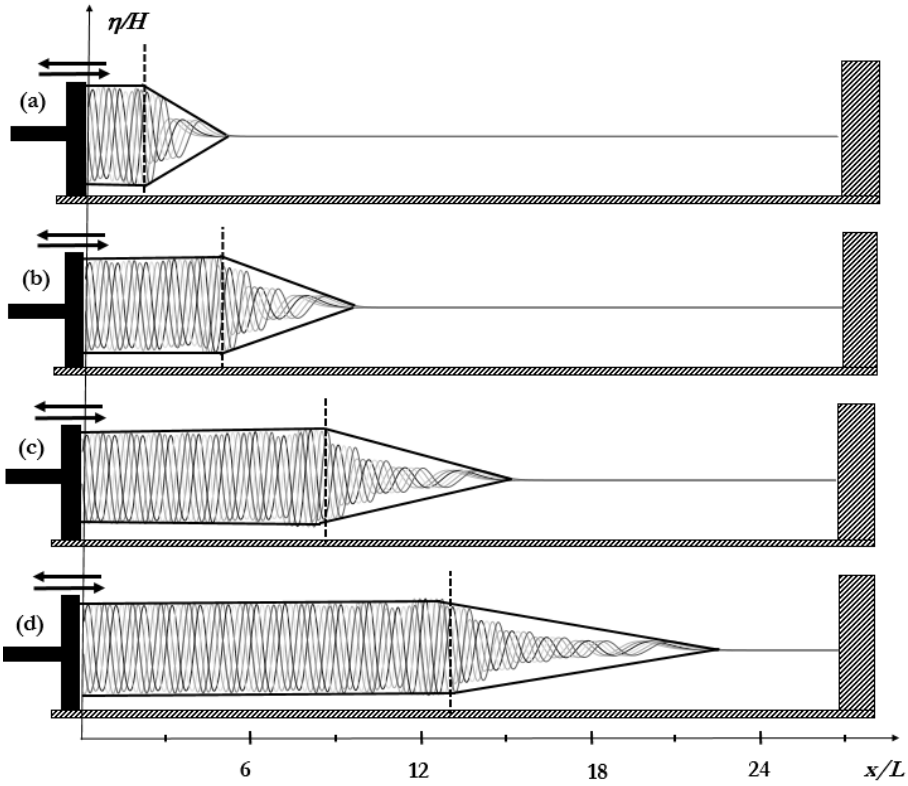

Figure 5.13- Envelopes of waves (H=0.20 m, T=3.5s) in different time instants, generated by a wavemaker, propagating in the wave-flume towards the vertical wall.

The head of the group hits the breakwater (placed at section y/L=26.7) in the instant t=25T and is reflected, towards the wavemaker. Starting from this time instant, the reflected waves superimpose with the incident ones generating a standing wave field expanding from the wall toward the wavemaker. The transition between the waves travelling towards the wall and the standing waves are clearly visible in Figure 5.14. As we can see, the height of the waves of the standing field is bigger than the height of waves generated by the wavemaker. The first snapshot taken at t=35T shows the group at 2.4L from the vertical wall and at 24 L from the wavemaker. Likewise, in the second snapshot, at t= 45T, the head of the group is at 6 L from the vertical wall and finally, in the last snapshot, taken at t=55T, the basin of head of the

standing wave train is at abscissa y= 12.8L from the wavemaker. The average group celerity of the reflecting waves is about equal to C_R= 2.5 m/s.

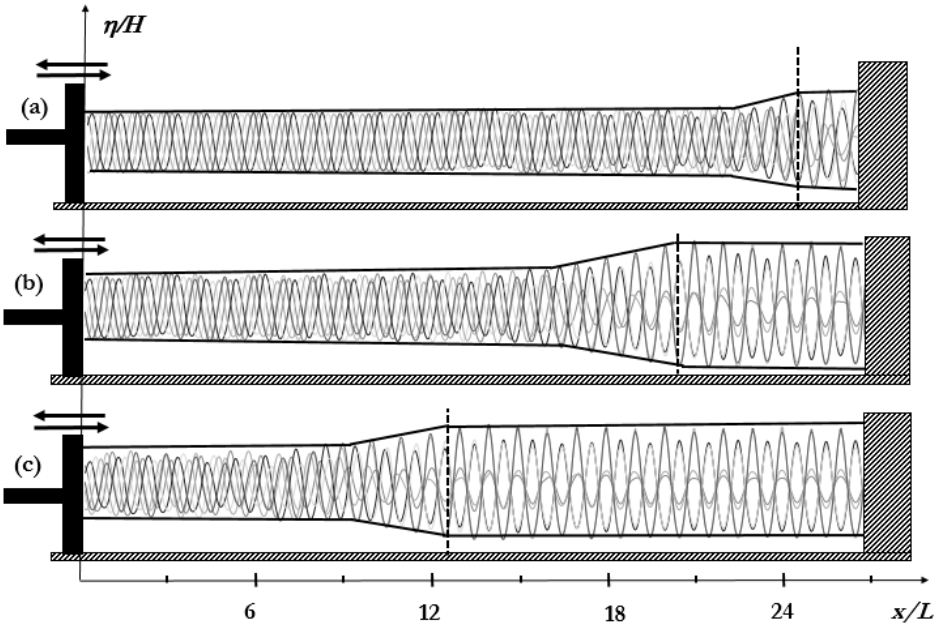

Figure 5.14- The overlapping of waves propagating towards the wall and waves reflecting towards the generator (H=0.20m, T=3.5s).

In conclusion, the standing wave field expands from the breakwater to the wavemaker with the same speed of the progressive wave field.

5.5 Conclusive remarks

Some preliminary tests on the numerical wave flume were conducted in order to validate the procedure. Firstly, the wave generation and propagation in the flume was checked comparing the surface displacement generated numerically with the analytical solution for transient waves generated in a flume (Huges,1993) initially at rest. As seen, there is a good agreement between the numerical results and the analytical ones, confirming that the approximate relationship for the stroke [eq.(3.8)] is well posed. Moreover, as

concerning the progressive waves field, we found that the wave kinematics is very close to Stoke's first order wave kinematics and dynamics. Indeed, both the head pressure waves, the horizontal and vertical components of velocity, calculated at some fixed depth below the free surface, are in a punctual agreement with analytical values.

Also from an energetic point of view, results agree with theory. The wave energy propagation along the flume calculated by means of (3.24) is 12% bigger than the numerical one. As regards to the standing waves field, the numerical envelope of waves in front of a vertical reflective wall, confirm the existence of nodes and anti-nodes, as well known by theory.

6 Results

6.1 The waves before the U-OWC

The wave field in front of the absorber breakwater is produced by the interaction between the incoming waves and the pulsating discharge through the plant. Therefore, the resultant wave field is quite different from the standing wave field in front of a vertical reflecting wall.

We could assume that the wave field before the U-OWC is periodic in space and time and the surface elevation and the velocity potential in front of the absorber are given respectively by (Boccotti, 2007a):

$$\eta(y,t) = H\cos(ky)\cos(\omega t) - H^I \sin(ky)\cos(\omega t + \varepsilon), \tag{6.1}$$

$$\phi(\mathrm{y,z,t}) = -g\omega^{-1}\frac{\cosh[k(d+z)]}{\cosh(kd)}\cdot \tag{6.2}$$

$$\cdot[H\cos(ky)\cos(\omega t) + H^I \sin(ky)\cos(\omega t + \varepsilon)],$$

Figure 6.1 shows the overlapping of several snapshots of the surface waves in the flume. Each frame is taken every $1/20T$, during a wave period.

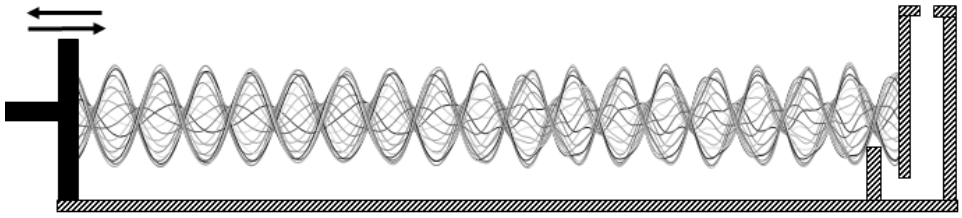

Figure 6.1 - Envelope of surface waves (H=0.20 m, T=3.5 s) in different time instants in front of U-OWC breakwater.

A detailed view is shown in Figure 6.2. As we can see, in front of the U-OWC wall, nodes disappear, giving place to "pseudo-nodes", which are points where the amplitude of η is at its minimum but different from zero.

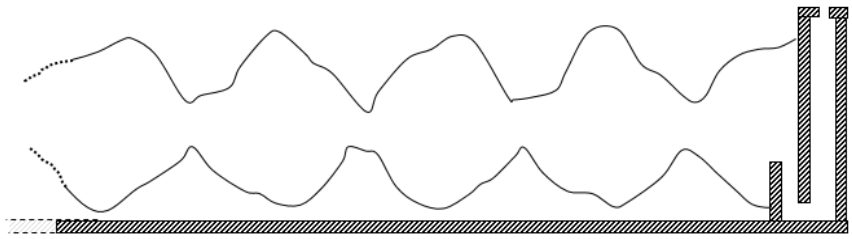

Figure 6.2 - Wave envelope of the quasi-standing wave field in front of the U-OWC shown in Figure 6.1 .

Moreover, when the incident wave train has impacted the absorber-breakwater, the wave amplitude at the breakwater wall is smaller than in front of a vertical reflecting wall.

Referring to the scheme of Figure 6.3 where Hv and Hn are the quasi-antinode height and the quasi-node height respectively, the equivalent incident wave height H_i, and the reflected wave height H_r, can be calculated by means of Healy's formula:

$$H_i = \frac{H_v + H_n}{2} \tag{6.3}$$

$$H_r = \frac{H_v - H_n}{2} \tag{6.4}$$

H_v and H_n being equal to 0.32 m and to 0.08 m, we have H_i=0.2m, H_r=0.12m respectively and hence the reflection coefficient

$$K_r = \frac{H_v - H_n}{H_v + H_n}, \tag{6.5}$$

is equal to 60%.

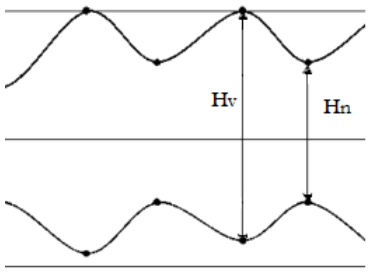

Figure 6.3 - Wave envelope of the quasi-standing wave field in which *Hv* is the quasi-antinode height and *Hn* is the quasi-node height.

Figure 6.4 shows four snapshots of the free surface elevation η, in front of the U-OWC. The chosen time instant is the same as in Figure 5.9. Also sections y_1, y_2, y_3 and y_4, mark the same distance from the wall ($L/4$, $L/2$; $3L/4$, and L, respectively) in the two cited Figures.

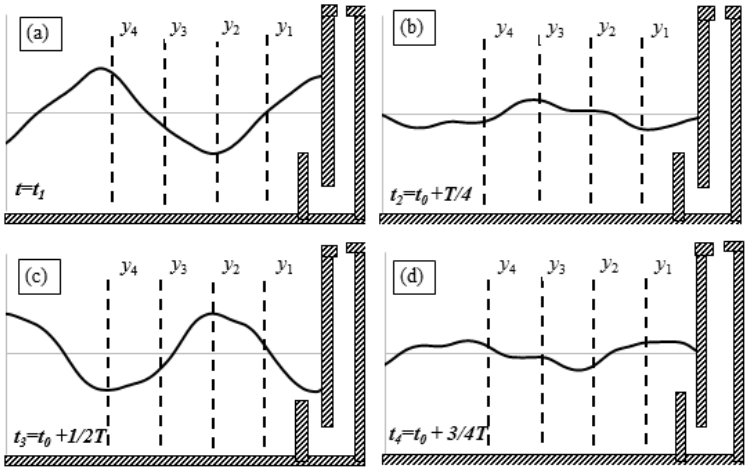

Figure 6.4 - Four snapshots of the free surface elevation η, at different time instants in front of the U-OWC breakwater.

Despite the trend of η being quite similar in the homonymous panels of Figure 5.9 and Figure 6.4, the horizontal velocity distributions exhibit quite a different trend between standing and quasi-standing wave field. As we can see, v_y is at its maximum under crests (y_4,t_1), (y_2,t_3), and its minimum under troughs

(y_4,t_3), (y_2,t_1), as occurs for a progressive wave. Near the breakwater wall (abscissa y_1), v_y crosses the z axis in proximity to the outer opening (instants t_1 and t_3).

The waves envelope before the U-OWC is shown in Figure 6.5. As we can see, a standing wave field is expanding from the absorber towards the wavemaker. The head of the incident wave train impacts the breakwater at the instant t=25T. After this moment, the partial reflection and the absorption by the plant starts, and in the proximity of the breakwater, we can see the overlapping of waves propagating towards the U-OWC (wave train A) and waves moving, in the opposite direction, towards the generator (wave train B). The wave train B expands gradually so that reflected waves superimpose to the incoming waves (train A). As we can see in Figure 6.5a this wave field has reached a distance 2.14 L from the U-OWC wall, marked by a vertical dashed line. The transition between the two wave fields (the incoming one and the reflected) is clearly visible by the inclined lines of the envelope.

Going forward, panel (b) shows a snapshot at t= 45T. As we can see, the wave field before the absorber is covering about 23% of the total of the flume and 10 period after (see panel c), is established in half the flume. The three snapshots enable us to estimate the advancing velocity of wave train B, which is the velocity with which the energy of this field expands towards the wavemaker.

The average group celerity C_R of wave train B is equal to 2.36 m/s and it is only 5 % less than propagation speed of the incoming waves.

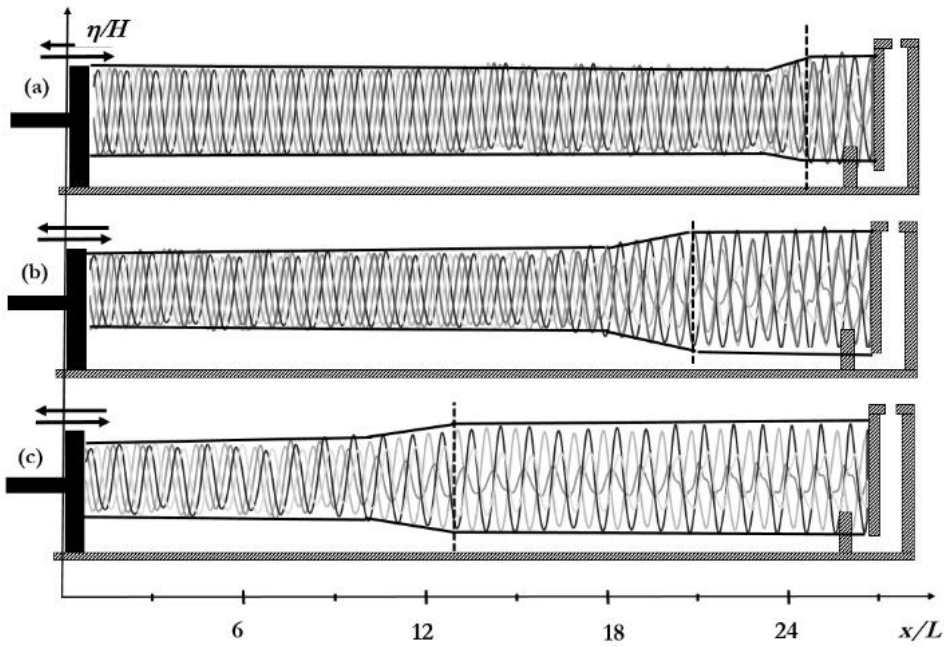

Figure 6.5 - Three snapshots of the waves envelopes (H=0.20m T=3,5s) before the U-OWC at different time instants.

Figure 6.6, shows the distribution of horizontal velocity v_y, along vertical sections y_1, y_2, y_3 and y_4, at the same time instants considered in Figure 5.9. At the time instants $t=t_1$ and $t=t_3$ the horizontal velocity is not zero along every vertical section, unlike the horizontal velocity distribution of standing waves in front of a reflected wall. In fact, at these time instants the free surface elevation is at its minimum but different from zero because of the existence of pulsating discharge, and the phase difference between the progressive and the reflected waves. In particular, at the vertical section placed at $L/4$ from the absorber, in the time instant $t=t_3$ ($= t_0 + 1/2T$), we can observe a change in the sign of the horizontal velocity along the z-axis. This phenomenon can be observed in Figure 6.7, where the vectors of water velocity in the wave flume at t_3 are represented. The position of section y_1 is indicated by the vertical yellow line. The inversion of the sign of the horizontal velocity is due

to the superimposition of the standing wave (i.e. the field that there would be without absorption) and the wave generated by the pulsating discharge.

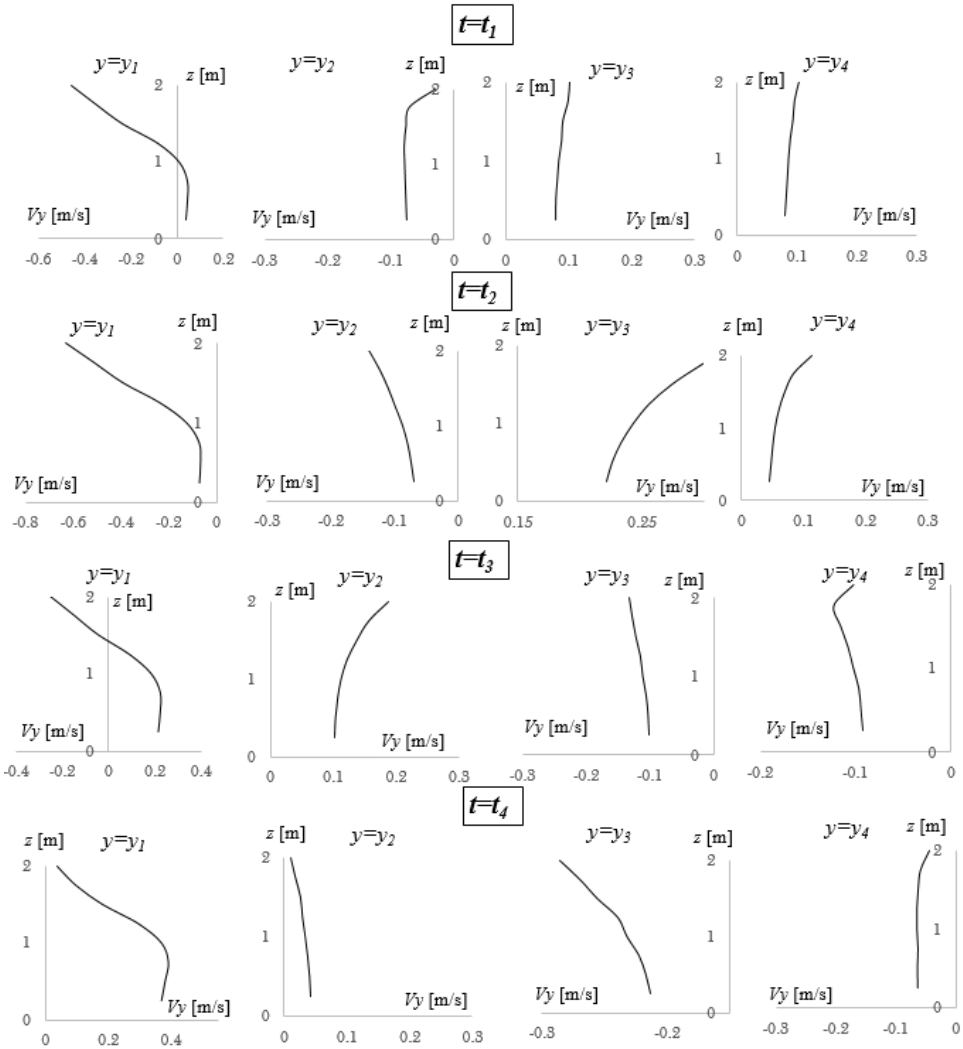

Figure 6.6 - Distribution of horizontal velocity v_y, along vertical sections y_1, y_2, y_3 and y_4, in the time instants of Figure 6.4.

As we can see, there is an evident macro circulation of the velocity at t_3, the instant when the trough is at a quarter of a wavelength before the plant, horizontal velocity is positive (i.e. directed towards the plant) below the quote of the upper opening of the vertical duct, and it is negative near the free

surface. Before the wave absorber, when a trough is at the wall, the discharge is exiting the plant, so the water must flow from the absorber towards the wavemaker, but after a while the water rises, so a mass of water must enter from marked section y_1. This is the reason why in the lower part of this section the water flows towards the plant, while in the upper part, it moves in the opposite direction. In other terms, near the surface the motion induced by the discharge prevails, whereas that induced by waves is stronger near the bottom.

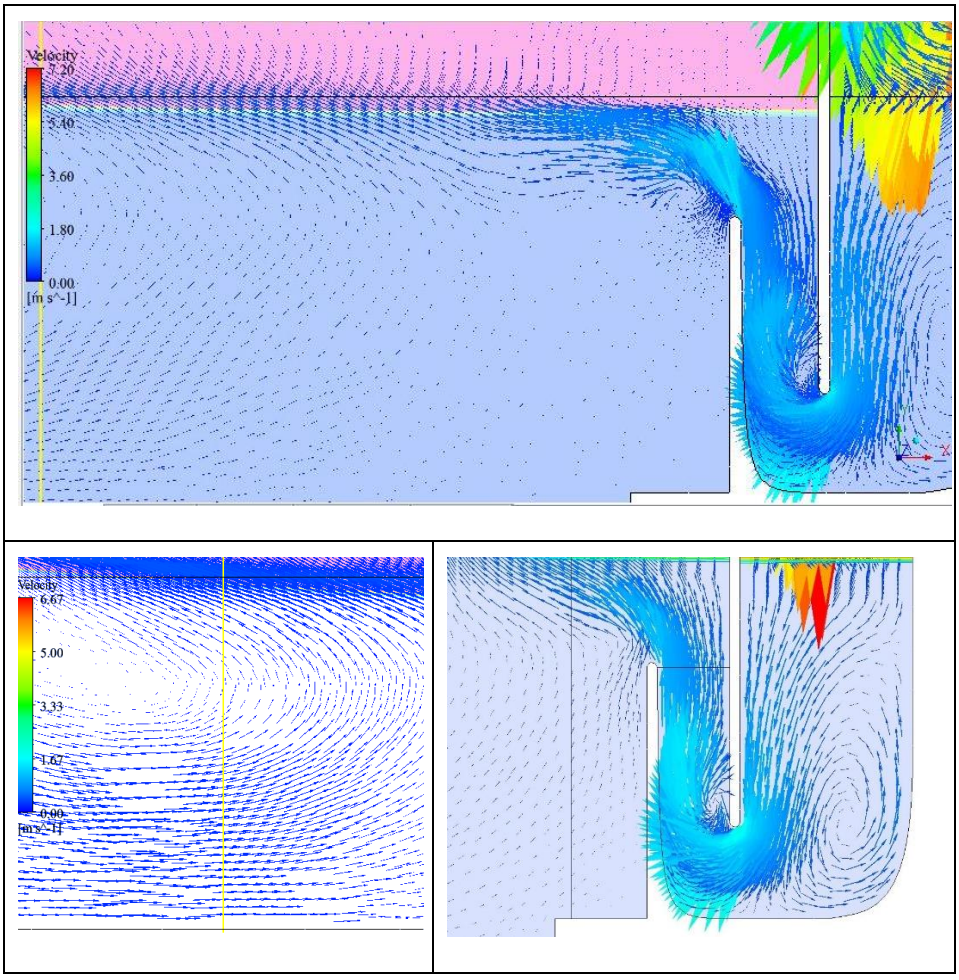

Figure 6.7 – Snapshots of the vectors of the water velocity in the flume. The yellow line represents the vertical section y_1, placed at $L/4$ from the U-OWC at t= 173.25 s (=t_3).

Lastly, Figure 6.8 shows what happens to the air-water interface inside the chamber, during a wave cycle. The position of the interface is shown at intervals equal to 1/20T. The sequence of instants during a rise up of the free surface is shown on the left of the panel (a). It is related to the increasing of the instantaneous level of water on the absorber wall, as shown in the diagram on the right. Panel (b) of Figure 6.8 shows a sequence of positions of the water surface in the chamber during its movement downward. The decrease of the water level is associated with the lowering of the free surface displacement on the wall. It is noticeable that the water surface inside the chamber remains horizontal during all stages of its movement. It is a remarkable difference from what happens in conventional OWC.

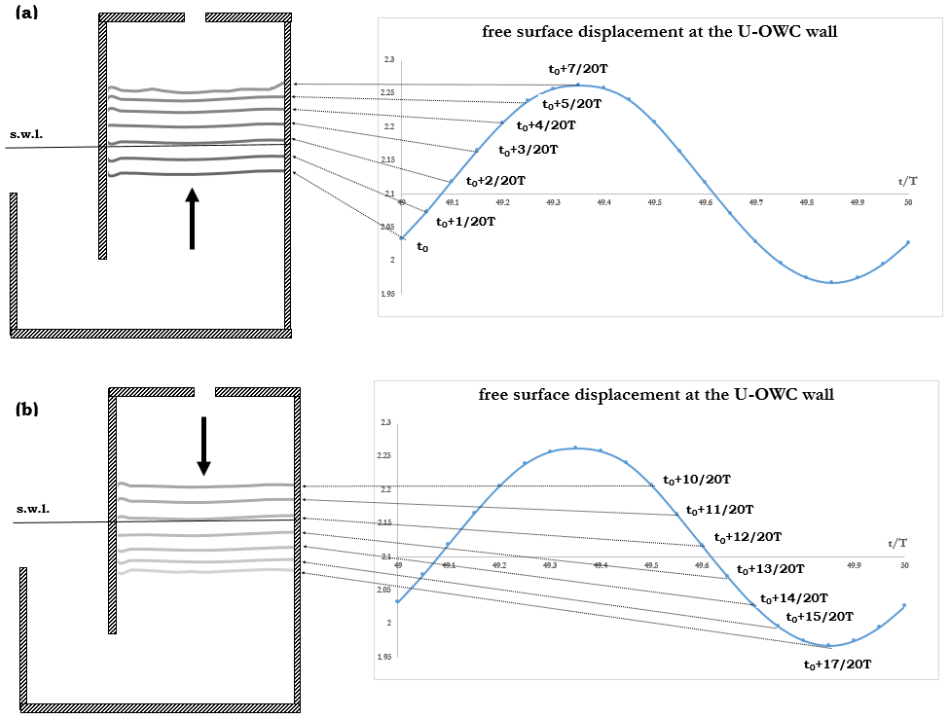

Figure 6.8 – Free surface displacement. On the left in the U-OWC chamber; on the right at the U-OWC wall.

Indeed, several authors (see Viviano et al., 2016) observed the formation of waves and jets inside the chamber. This happens mostly with the highest waves, producing some impulsive wave loads on the wall and some risks to the power take off system. It is due to the fact that wave can propagate inside the chamber because of the large opening of conventional OWCs. Conversely, waves cannot enter into the U-OWC thank to the presence of the vertical duct, which transforms wave energy into water flow energy.

6.2 Plant efficiency estimate

In order to verify the share of the incident wave flux absorbed by the U-OWC, we calculated the energy flux in different sections along the wave flume. Figure 6.9 shows the energy flux versus time at three different vertical sections. Panel (a) shows the energy flux of the incoming wave train (i.e. the waves generate by the wavemaker) at some wavelengths from the wavemaker; panel (b), the energy flux of the wave field before the U-OWC and, finally, panel (c) shows the energy flux absorbed by the plant.

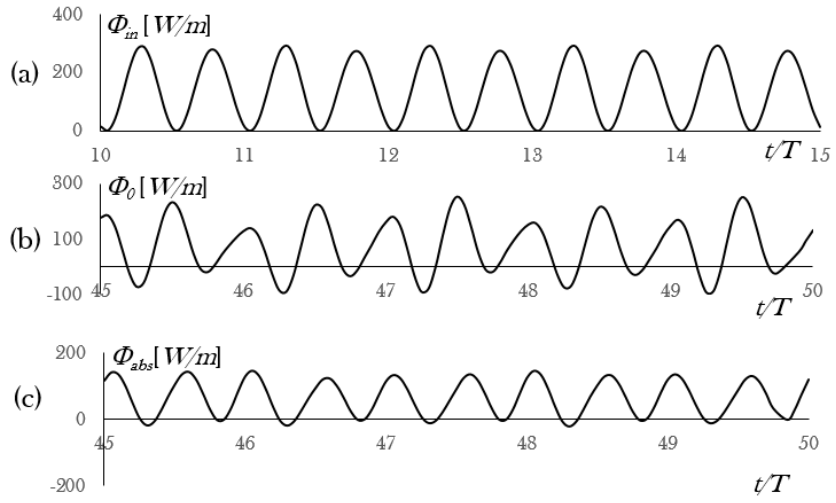

Figure 6.9 - The instantaneous energy flux versus time: (a) of incident waves; (b) in front of the energy absorber; (c) inside the plant. [Values refer to unitary widths of both the flume and the absorber.]

The mean energy flux of waves generated by the wavemaker is approximatively equal to 140W/m. The mean energy flux of the wave fields before the U-OWC is about 74W/m and, finally, the mean absorbed power is 64W/m.

These values are consistent with what emerges when applying the energy balance equation to the control volumes indicated in Figure 6.10. In fact, the energy flowing through section AB (=140W/m), is partially reflected by the absorber and partially absorbed by it (=64W/m). The balance of energy applied to volume CDEF, states that the energy flux crossing section CD is equal to the energy flux volume through section EF, the mean energy inside CDEF being constant. On the contrary, the energy content of volume ABEF is varying in time due to the expansion of the reflected wave field, towards the wavemaker. The energy variation inside ABEF equals the difference between the energy flux in AB and EF.

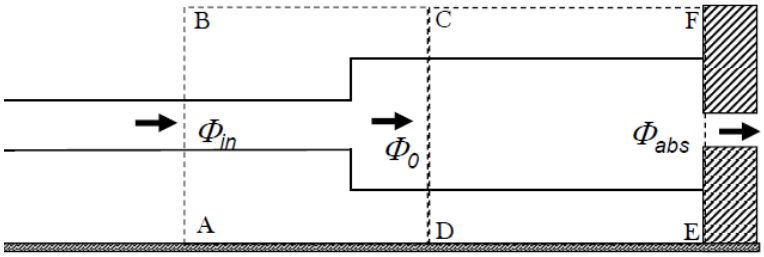

Figure 6.10 - Control volumes for energy balance check. Φ_{in} is the energy flux per unit length of the incoming waves; Φ_0 is the mean energy flux per unit length of waves before the absorber, and Φ_{abs} is the mean energy flux absorbed by a unitary length of the plant.

The energy absorbed by the plant is 46% of the energy generated by the wavemaker. The performance of the plant depends on the resonance. If the wave period is equal to the eigenperiod, the plant works in resonance.

To check how close to resonance the working conditions are, we look at the pressure fluctuation Δp, at the outer opening of the vertical duct and at

the discharge Q_p, in the plant, (see Figure 6.11). The time shift T^* between Δp and, Q_p, is equal to $3/20T$. A T^* positive means that the wave period is smaller than the eigenperiod (Boccotti, 2015), while $T^*<0$ indicates that the wave period is greater. Therefore, in the present case, to improve the plant's performance, we should increase the wave period.

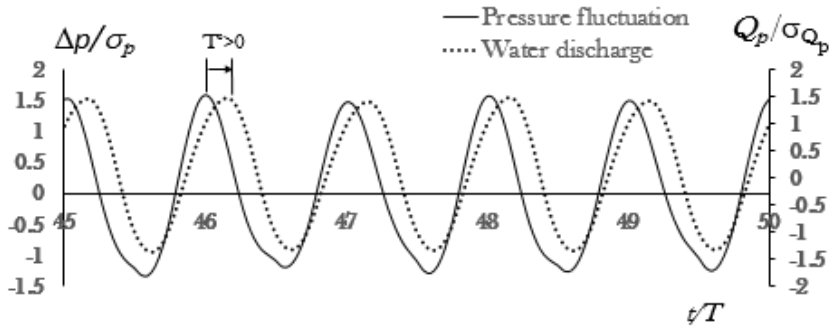

Figure 6.11 - Pressure fluctuation Δp at the outer opening and discharge Qp in the plant, as a function of t/T. Values have been divided by their own standard deviation σ. [The Qp is positive if it enters the plant.]

6.3 The frequency response of the plant

In the previous section, we illustrated the interaction between the U-OWC and a wave train with T=3.5 s and H=0.2m. As shown, under this condition the plant is able to absorb about 50% of the incident waves power. In order to check the performance of the plant whilst varying the periods of incoming waves, we carried out several simulations, for 3.5 s< T < 9 s, maintaining the wave height at the fixed value of 0.2m.

We define the absorption coefficient A, as the ratio between the mean power absorbed by the plant Φ_{abs}, and the mean energy flux Φ_{in}, of the incident waves. The incident wave power Φ_{in}, is calculated at a fixed abscissa of the wave flume located far enough from the absorber during the time interval in which a stationary progressive wave is established.

Figure 6.12 shows Φ_{in} versus wave period T, [line with crosses]. For comparison, the values calculated by linear wave theory [eq. (3.25)] have been reported too [dashed line].

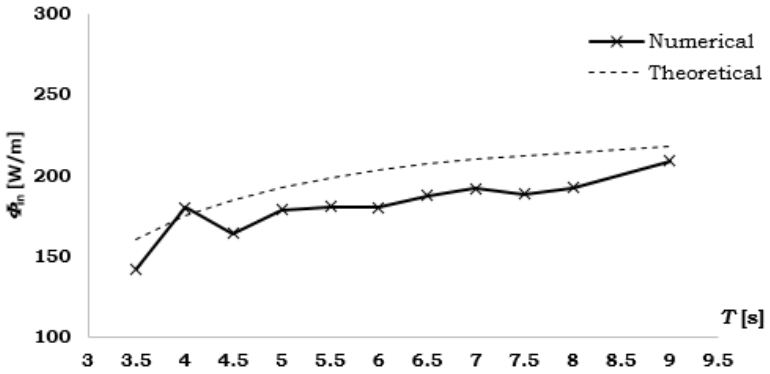

Figure 6.12 – The mean energy flux of the incident wave. The dashed line shows the theoretical results, calculated by eq. (3.25) and, the line crosses, the numerical results.

As we can see, there is a reasonably good agreement, being that the maximum difference between theoretical and numerical values, corresponding to the same abscissa, is less than 10%.

For each generated wave, we calculated the mean energy flux absorbed by the plant. In Figure 6.13, the absorption coefficient A, is shown. As we can see, the plant absorbs about 58% on average of the incident wave power. In particular, A reaches its maximum with waves having periods between 4s and 4.5s. In correspondence to these periods, the plant absorbs 87% of the wave energy, suggesting us that it is working in resonance.

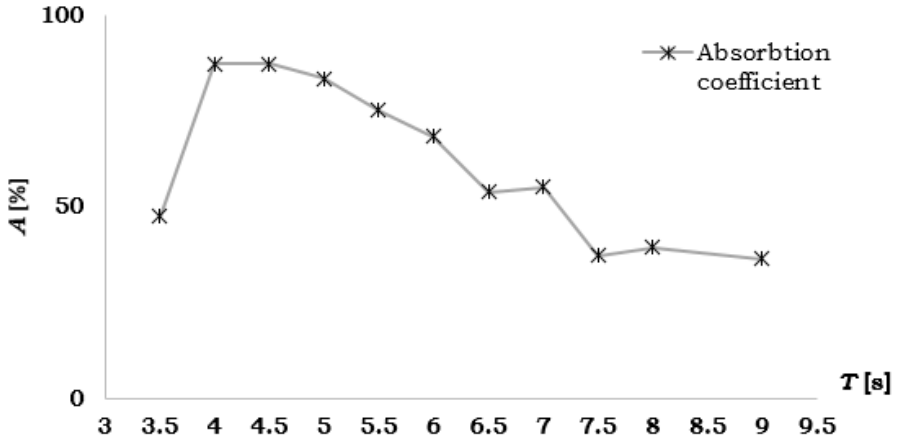

Figure 6.13 – The absorption coefficient *A*, versus wave period *T*.

The resonant coefficient *R*, introduced in section 4, is a useful index to check how close to resonance the plant is working. *R* is calculated starting from the phase difference between the water discharge Q_p and the fluctuating wave pressure at the outer opening of the plant Δp. As said, values of *R* less than zero mean that the wave period is greater than the eigenperiod, whereas values greater than zero mean that the wave period is smaller than the eigenperiod. Values close to 0 mean that the plant is near to resonance. Figure 6.14 shows the values of *R*, for each period of the generated waves. As we can observe, the nearest value to zero is -0.2, and it occurs at T= 4 s.

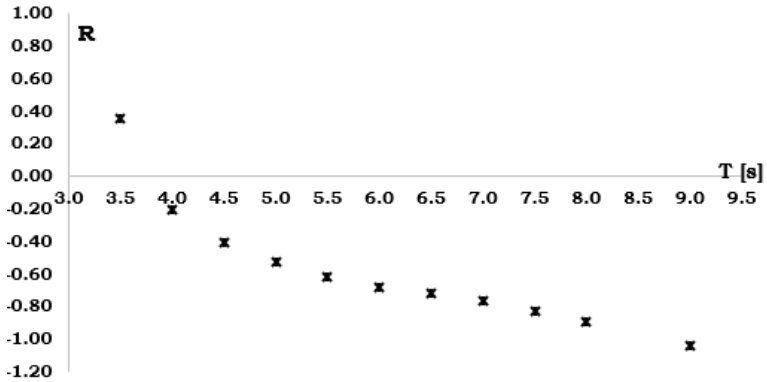

Figure 6.14 – The resonant coefficient *R*, for the different wave periods analyzed.

Finally, in order to check Boccotti's theory concerning the wave field in front of the U-OWC, we calculated the ratio between the celerity group of the reflected waves and the celerity group of the incoming waves, and the amplification factor β. The latter represents the quotient between the wave amplitude at the breakwater converter and the wave amplitude at a conventional reflecting breakwater.

Tab.1 shows a synthesis of the main results obtained. The values of the amplification factor β, about on average equal to 0.84, confirm that the wave amplitude at the breakwater is always smaller than the amplitude before a conventional reflecting breakwater subjected to the same incoming waves. Tab.1 shows also that β is much closer to 1 as the absorption coefficient A, decreases. Also, the ratio between the celerity group of the reflecting waves field and the incident waves is close to 1.

Tab.1 – The plant performance obtained from the CFD simulations.

Time Period [s]	*Incident waves power [W/m]*	*Absorption waves power [W/m]*	*Absorption coefficient [%]*	*Resonance coefficient*	C_R/C_G	*Amplification factor*
3.5	142.4	67.8	47.6	0.36	0.90	0.85
4.0	180.3	157.4	87.3	-0.20	0.86	0.77
4.5	164.6	143.6	87.3	-0.41	0.89	0.63
5.0	179.1	149.6	83.5	-0.53	0.95	0.72
5.5	181.1	136.2	75.2	-0.62	0.93	0.81
6.0	180.3	123.1	68.3	-0.68	0.91	0.87
6.5	187.9	101.5	54.0	-0.72	0.93	0.92
7.0	192.1	105.9	55.1	-0.76	0.94	0.86
7.5	188.7	70.6	37.4	-0.83	0.92	0.92
8.0	192.4	76.0	39.5	-0.89	0.92	0.95
9.0	209.0	76.5	36.6	-1.04	0.93	0.94

6.4 Comparison between experimental data and numerical simulations

Boccotti et al. (2007) describe the result of the experiment carried out, directly, at sea on a 1:6 scale model of a U-OWC breakwater conceived for the Mediterranean coast. The physical model and the plant used in this thesis have the same size.

During the experiment at sea, several sea states, formed by wind waves or by a superimposition of wind waves and swells were recorded. They were characterized by energy spectra whose peaks ranged between 2 s and 9 s. The authors measured the wave pressure fluctuations on the outer opening of the vertical duct and in the undisturbed wave field with a transducer placed at the same depth beneath the mean water level. In each record, which lasted 5 min, they obtained the values of the significant wave height, the peak period T_p and the absorption coefficient A. Figure 6.15 shows A as a function of T_p. Each point represents a record. In total, there are 187 records, 96 of them are wind waves (marked by spreaders), 60 records are of swells (marked by points) and about 31 records represent wind waves superimposed on swells.

Figure 6.16 shows the data of Figure 6.15 and the values of A obtained in the present work (bold line with rhombus). For comparison, a regression of Boccotti et al. (2007), data has been reported too (dashed line). Both the two lines show that A grows rapidly for increasing wave periods up to a maximum ranging between 4s and 5 s. The maximum value of A is close to 90% for both the experiments (both the physical and the numerical ones).

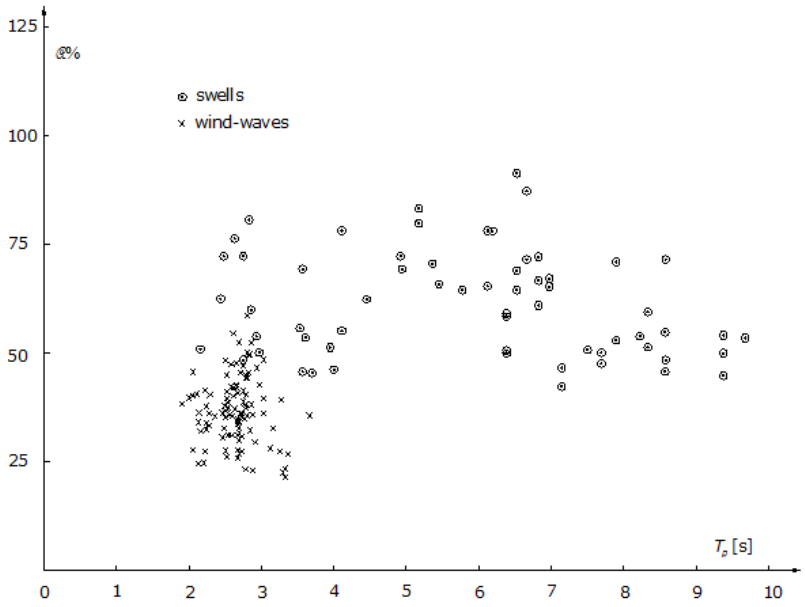

Figure 6.15 – The absorption coefficient as a function of the peak period obtained by Boccotti et al. (2007).

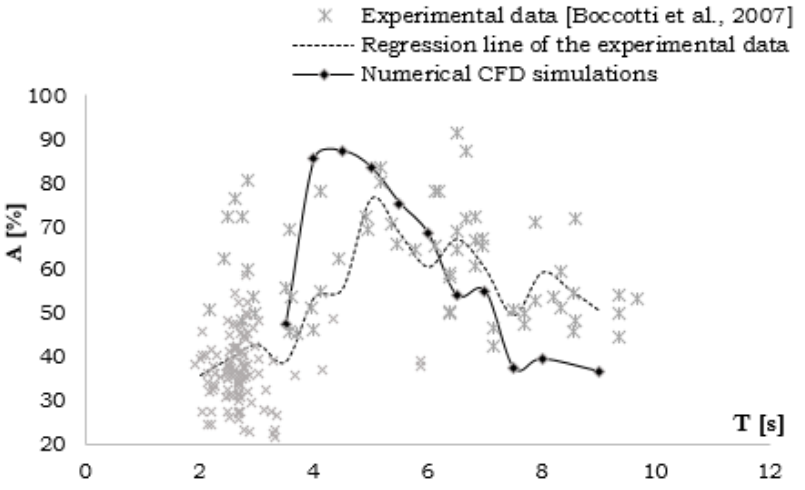

Figure 6.16 – Comparison of the absorption coefficient carried out by Boccotti et al., 2007 and the absorption coefficient calculated by means of CFD simulations.

The plant tested at sea achieved better performance with lower frequencies than those reached in the numerical flume with periodic waves. In particular,

very high values of A occurred with some records of long swells. In these cases, the wave height at the absorbing breakwater grows with respect to the wave height at a conventional reflecting breakwater. Therefore, the amplification factor β is greater than 1. This phenomenon is evident looking at Figure 6.17. It shows the comparisons of the spectrum of the Δp recorded on the outer opening of the vertical duct and the spectrum of Δp recorded in the undisturbed wave field at the same depth beneath the mean water level. This super amplification corresponds with a β of about 2.4.

According to Boccotti's theory, the extraordinarily large value of β is not the reason for the large energy absorption, in that it is due to the slowing down of the propagation speed of the reflected wave energy, C_R. Indeed, if the absorber works far from the resonance condition (i.e. when waves with very large wave period occur) and it absorbs 100% of the incident wave energy, the celerity of the reflected wave field is zero. This means that at the breakwater-converter there is a huge wave amplification, which remains locked to the breakwater and cannot expand backwards. The fact that there is no energy advancing seaward implies that the whole incident wave energy is absorbed by the plant (Boccotti, 2015).

In order to verify the behavior of the plant under this condition we conducted two numerical simulations which replicate the interaction with the sea states of Figure 6.17.

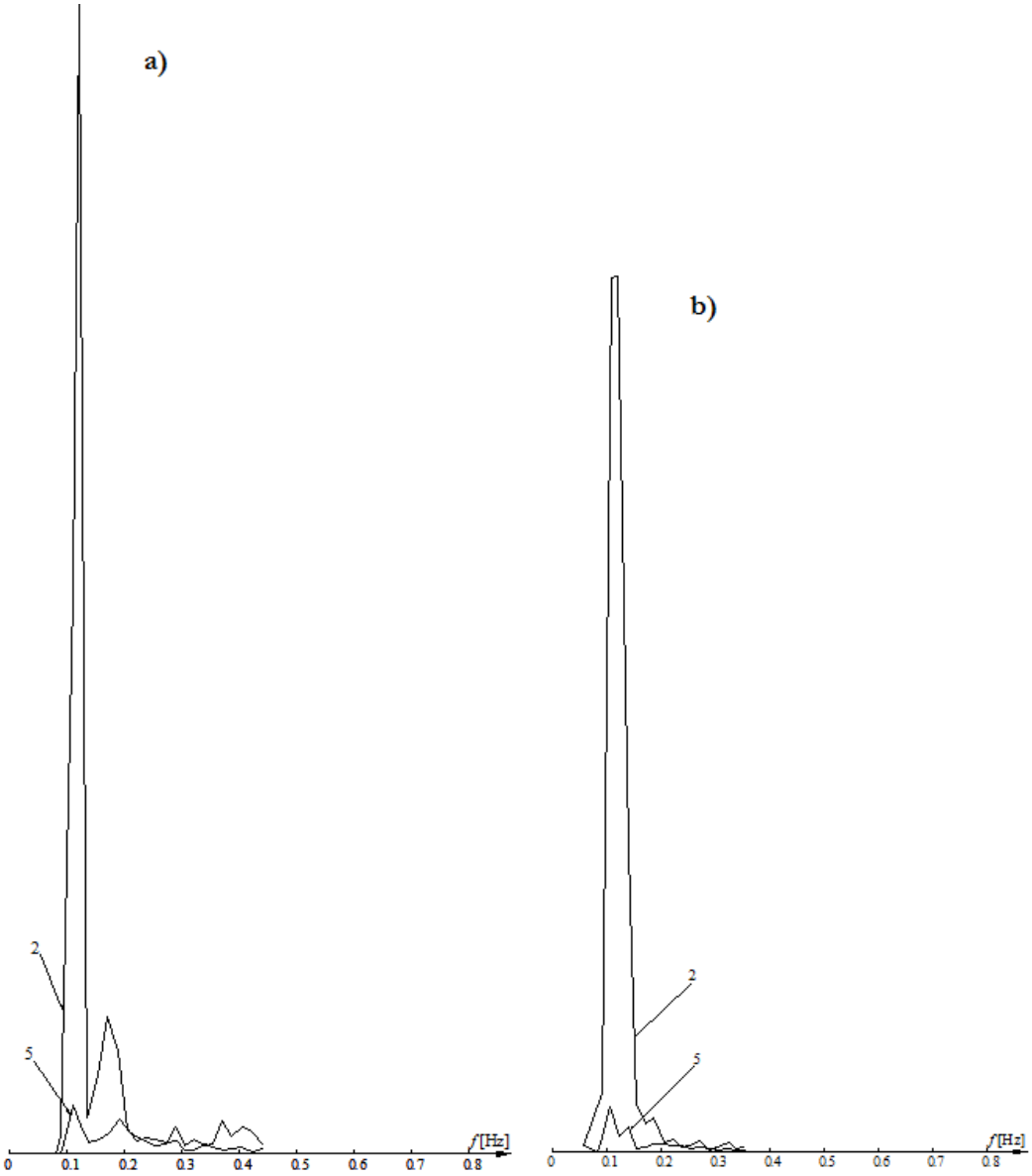

Figure 6.17 – The spectra of the pressure fluctuations Δp, on the outer opening of the vertical duct and in the undisturbed field. (a) the spectra of a record of swells with H_s = 0.191 m. (b) the spectra of a record of swells with H_s = 0.159 m. [Boccotti et al., 2007.]

Figure 6.18 represents a scheme of a piece of spectrum (POS), at the undisturbed wave field (E_5) and at the breakwater converter (E_2). The r.m.s. of a POS is given by

$$\sigma_{POS} = \sqrt{\int_{f_1}^{f_2} E(f)\mathrm{d}f} \,, \tag{6.1}$$

and the β of a POS, is defined as

$$\beta_{POS} = \frac{1}{2}\sqrt{\int_{f_1}^{f_2} E_2(f)\mathrm{d}f} \Big/ \sqrt{\int_{f_1}^{f_2} E_5(f)\mathrm{d}f} \,. \tag{6.2}$$

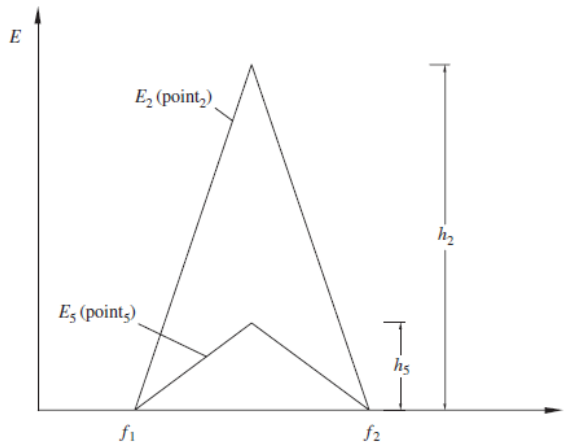

Figure 6.18 – Reference scheme for the analysis of the deformation of the frequency spectrum from the undisturbed wave field (E_5) to the breakwater converter (E_2) [Boccotti et al. (2007)].

The periodic wave generated in the CFD simulation has a period $T = T_p$, and a crest-to-trough height $H = H_s/\sqrt{2}$ having the same r.m.s. of the surface displacement as the sea waves.

Referring to the POS of Figure 6.17*a* having $0.089 < f < 0.135$, we obtain

(i) $H = 0.07$ m, $T = 9$s;

and, to the POS of Figure 6.17*b* having $0.092 < f < 0.155$, we obtain

(ii) $H = 0.09$ m, $T = 8$.

Figure 6.19 shows the energy flux Φ_{abs}, absorbed by the plant. In particular, panel (a) shows the Φ_{abs} of the plant subjected to waves (i) and panel (b) Φ_{abs} of the plant subjected to waves (ii).

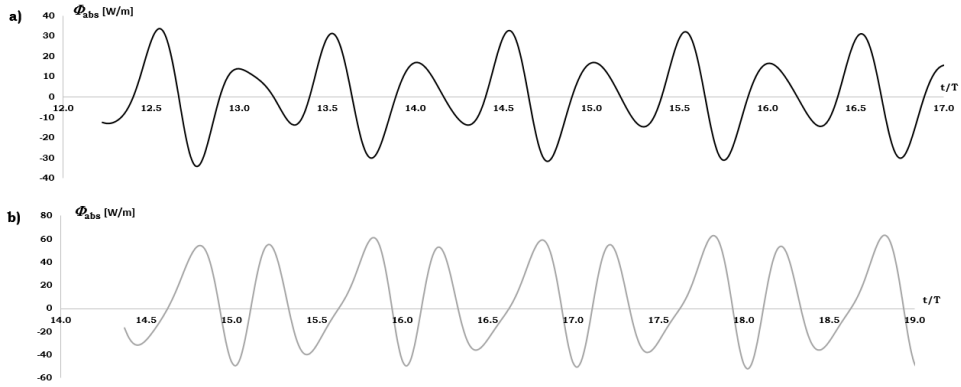

Figure 6.19 – The energy flux absorbed by the plant. Panel (a) refers to wave (i) Panel (b),to wave (ii).

As we can see the energy flux assumes many negative values, meaning that the plant is not tuned with the incoming waves (i.e. operations are far from resonance). It is confirmed by very low values of A shown in Tab.2, disagreeing with Boccotti's theory estimations. The resonance coefficient is close to -1. Furthermore, in these two simulations, the amplification factor β is close to 1 and the ratio between the C_R and C_G (= group celerity of the reflected wave / group celerity of the incoming wave), is close to one instead of approaching zero as indicated by theory.

Tab.2 – The summary of the simulations of two wave groups in which their period is greater than eigenperiod of the plant.

T (s)	*H [m]*	*Incident waves power [W/m]*	*Absorption waves power [W/m]*	*Absorption coefficient [%]*	*Resonance coefficient*	C_R/C_G	*Amplification factor*
8	0.09	40.5	6.27	15.5	-1	0.91	1.00
9	0.07	25.1	0.37	1.5	-1	0.94	1.01

Conclusions

In this work, we carried out a numerical experiment aiming to analyze the interaction between waves and a U-OWC breakwater. The numerical method adopted is the numerical integration of Reynolds averaged Navier-Stokes equation (RANS) using the volume of fluid (VOF) model, to describe the multiphase flow, implemented in the commercial code Ansys Fluent 17.0, Academic Version. To validate the numerical flume, we carried out some preliminary tests finalized to compare numerical results of a vertical reflecting wall with the analytical solution of linear standing waves.

The geometry and size of the U-OWC breakwater utilized in this work is the same as the 1:6 scale physical model of breakwater tested by Boccotti et al. (2007) directly, at sea, off the coast of Reggio Calabria (in the eastern coast of the Messina Straits).

The performance of the plant depends on whether it is working in resonance or not. Tuning of the plant with waves is revealed by the presence of a time shift between the water discharge into the plant and the pressure fluctuation at the outer opening of the vertical duct. To check the plant working conditions, we choose waves with characteristics (height and period) similar to those which interacted with the plant at sea. Therefore, we made several simulations, varying the wave period in the range [3.5, s 9 s] and maintaining the wave height fixed at 0.2m.

With an incoming wave train having height of H=0.20 m and period of T=4 s, the plant absorbs nearly the 90% of the incoming wave energy. In this condition the lag between the fluctuating pressure on the outer opening of the plant and the pulsating discharge is near to zero. It is a result which agree very well with the performance measured at sea in correspondence to wind

generated waves with similar periods. Moreover, a relevant issue emerged from the present work concerning the oscillations of the air-water interface in the chamber. Unlike what occurs in conventional OWCs, the free surface remains practically horizontal during its motion. This matter has some positive consequence for structural safety, because there is no impact pressure on the inner wall of the chamber, as observed in conventional OWCs.

Some remarkable differences arise in the interaction with very large wave periods. Indeed, Boccotti et al. (2007) found that with some long swells the plant achieved high values of absorption coefficient, despite its working conditions being far from resonance. They gave an explanation of this occurrence in light of Boccotti's theory concerning the wave field in front of the U-OWC (Boccotti, 2007). The basic assumption of theory is that the propagation speed of the envelope of the reflected wave C_R can vary between zero and C_G. As a consequence, the reflected wave field is locked near the breakwater wall and doesn't expand towards the open sea (the wavemaker). All the numerical simulations carried out in this work showed that C_R is nearly equal to C_G. Moreover, we have not found any large absorption far from resonance. These results are congruent with an alternative formulation of Boccotti's theory, which is based on the assumption that $C_R = C_G$. Also, the obtained values of A are consistent with this formulation.

Considering the discrepancies which emerged from the results of the physical experiment in correspondence with the largest wave periods, we cannot draw conclusions concerning the validity of Boccotti's theory, at least regarding the plant behavior for $R \rightarrow -1$ (i.e. for periods much larger than the eigenperiod). An experiment on a physical model carried out in a long wave flume could give a definitive answer.

Acknowledgments

The computing resources and the related technical support used for this work have been provided by CRESCO/ENEAGRID High Performance Computing infrastructure and its staff [G. Ponti et al., 2014[1]]. CRESCO/ENEAGRID High Performance Computing infrastructure is funded by ENEA, the Italian National Agency for New Technologies, Energy and Sustainable Economic Development and by Italian and European research programmes, see http://www.cresco.enea.it/english for information".

[1]G. Ponti et al., "The role of medium size facilities in the HPC ecosystem: the case of the new CRESCO4 cluster integrated in the ENEAGRID infrastructure", Proceedings of the 2014 International Conference on High Performance Computing and Simulation, HPCS 2014, art. no. 6903807, 1030-1033;

References

Arena, F. & Filianoti, P. (2003). "*A new kind of breakwater for converting wave energy into electrical power*" Fifth European Wave Energy Conference (EWEC) University College Cork, Ireland 17th-20th September 2003.

Arena, F. & Filianoti, P. (2007) "*A small-scale field experiment on a submerged breakwater for absorbing wave energy*", ASCE Journal of Waterway, Port, Coastal, and Ocean Engineering, Volume 133, Issue 2, pp. 161-167, doi:10.1061/(ASCE)0733-950X (2007)133:2(161);

Aricò C., Sinagra M., Tucciarelli T., (2013). "*Monotonic solution of flow and transport problems in heterogeneous media using Delaunay unstructured triangular meshes*". Advances in Water Resources - Volume 52, February 2013, Pages 132–150

S. F. Barstow, G. Mørk, L. Lønseth, P. Schjølberg, U.Machado, G. Athanassoulis, K. Belibassakis, T. G., C. Stefanakos and G. Spaan, (2003). WORLDWAVES- "*High quality coastal and offshore wave data within minutes for any global site*", Proc. 2003 Int. Conference on Offshore Mechanics and Arctic Engineering, Mexico.

Barstow, S., Haug, O. and Krogstad, H. (1998) "*Satellite Altimeter Data in Wave Energy Studies*". Proc. Waves'97, ASCE, vol. 2, pp. 339-354

Barth T. J. & D. Jespersen, (1989). "*The design and application of upwind schemes on unstructured meshes*". Technical Report AIAA-89-0366. AIAA 27th Aerospace Sciences Meeting, Reno, Nevada.

Boccotti P, (2000). "*Wave mechanics for ocean engineering*", Amsterdam - Lausanne - New York- Oxford - Shannon - Singapore – Tokyo, an imprint of Elsevier Oceanography Series, 64 [2000]

Boccotti P, (2002). US Patent 6450732 B1.

Boccotti P. (2003a), "*On a new wave energy absorber*", Ocean Eng. 30, 1191-1200.

Boccotti P., (2003b). European Patent EP 1133602 B1.

Boccotti P., (2003c). PCT N. PCT/IT03/00310.

Boccotti P., (2007a). "*Caisson breakwaters embodying an OWC with a small opening - Part I: Theory*", Ocean Engineering 34 (5-6), 806-819.

Boccotti P., (2007b). "*Comparison between a U-OWC and a conventional OWC*", Ocean Engineering 34 (5-6), 799–805

Boccotti P., Filianoti P., Fiamma V., Arena F., (2007). "*Caisson breakwaters embodying an OWC with a small opening - Part II: A small-scale field experiment*", Ocean Engineering 34 (5-6), 820-841.

Boccotti P, (2015). "*Wave mechanics and wave loads on marine structure*", Amsterdam; Boston, Butterworth-Heinemann, an imprint of Elsevier, [2015]

Chakrabarti S.K., (1994). "*Offshore structure modeling*" World Scientific Publishing, Singapore.

ChorinJ., (1968). "*Numerical solution of Navier-Stokes equations*". Mathematics of Computation. 22. 745–762.

Dean R.G. & Dalrymple R.A., (1984). "*Water wave mechanics for engineers and scientists*", Prentice Hall, Inc. Reprinted Singapore: World Scientific Publishing Co., 1991, pp. 170-178.

Drew B., A.R. Plummer, M.N. Sahinkaya, (2009). "*A review of wave energy converter technology*", Proc. Institution Mech. Eng. Part A J. Power Energy, 223 (8), pp. 887–902

Falcão A. F. de O, (2003). "*First-generation wave power plant: current status and R&D requirements*", Proc. of OMAE2003; 22nd International Conference on Offshore Mechanics and Arctic Engineering, Cancun, Mexico.

Falcão António F. O., (2014). "*Modelling of Wave Energy Conversion*", Instituto Superior Técnico, Universidade de Lisboa Tech. Rep. (2013) https://fenix.tecnico.ulisboa.pt/downloadFile/3779580606646/Chapter%25201%25282014%2529.pdf

Falcão Antonio F.O. and Joao C.C Henriques, (2016). "*Oscillating-water-column wave energy converters and air turbines: A review*", Renewable Energy 85 (2016) 1391e1424.

Falnes J., (2002). "*Ocean Waves and Oscillating Systems*". Cambridge University Press. ISBN 0-521-01749-1., 288 pp.

Ferreira F. B, D.S. Falcão, V.B. Oliveira, A.M.F.R. Pinto., (2015). "*Numerical simulations of two-phase flow in proton exchange membrane fuel cells using the volume of fluid method - A review*". Journal of Power Sources 277 (2015) 329e342

Filianoti P. (2000). "*La disponibilità di energia ondosa su varie aree del pianeta*". In Atti del XXVII Convegno di Idraulica e Costruzioni Idrauliche, Genova, Italia.

Filianoti P. & Camporeale S., (2007). "*A small scale field experiment on a wells turbine model*", 7th European Wave and Tidal Energy Conference, 11 - 14 Sept., Porto.

Filianoti P. & Camporeale S., (2008). "*A linearized model for estimating the performance of submerged resonant wave energy converters*". Renewable Energy, 33, 4, 631-641.

Filianoti P., S. M. Camporeale, (2009a). "*In field measurements on a small scale OWC device*", Proceedings of the 8th European Wave and Tidal Energy Conference, Uppsala, Sweden, 2009.

Filianoti P., S. M. Camporeale, (2009b). "*Behaviour of a small Wells turbine under randomly varying oscillating flow" submitted to the Journal "Renewable Power Generation*." published by the Institution of Engineering and Technology Stevenage, Hertfordshire, UK

Filianoti P. & Piscopo R., (2015). "*Sea wave energy transmission behind submerged absorber caissons*", Ocean Engineering 93, 107-117.

Fucai Li and Yanmin MuLow, (2014). "*Mach number limit of the full compressible Navier–Stokes–Maxwell system*", Journal of Mathematical Analysis and Applications, 412, 334–344

Fugro OCEANOR website, available from http://www.oceanor.no/Services/Worldwaves/ (accessed 18.10.16)

Gu H.B., Causon D.M., Mingham C.G., L. Qian, Han-Bao Chen, (2011) "*On the Numerical Simulation of a Piston-type Wavemaker*", International Offshore and Polar Engineering Conference Maui, Hawaii, USA, June 19-24, 2011.

Haikal G. and K.D. Hjelmstad, (2010). "*An enriched discontinuous Galerkin formulation for the coupling of non-conforming meshes*", Finite Elements in Analysis and De-sign 46 496–503

Havelock, T.H., (1929). "*Forced Surface Wave on Water*", Philosophical Magazine, Series 7, Vol. 8, pp 569-576.

Heath T. V., (2012). "*A review of oscillating water columns*" Philosophical Transaction of Royal Society 370, 235–245

Hirt C.W & B.D Nichols, (1981). "*Volume of fluid (VOF) method for the dynamics of free boundaries*", Journal of Computational Physics Volume 39, Pages 201–225.

Hughes, S.A., (1993), "*Physical Models and Laboratory Techniques in Coastal Engineering*", Advanced Series on Ocean Engineering, Vol. 7. World Scientific, London, 568 pp.

Johan T., Deen, N.G., Peters, E. A. J. F. & Kuipers, J. A. M., (2015). Chapter Three – *Euler–Lagrange Modeling of the Hydrodynamics of Dense Multiphase Flows, Advances in Chemical* Engineering Volume 46, 2015, Pages 137–191

Komen, GJ and Cavaleri, L. and Donelan, M. and Hasselmann, K. and Hasselmann, S. and Janssen, P. et al, (1994): "*Dynamics and Modelling of Ocean Waves*", Cambridge, 534 pp

Lopez & Iglesias, (2014). "*Efficiency of OWC wave energy converters: A virtual laboratory*", Applied Ocean Research 44 (2014) 63–70.

Mavriplis D. J., (1997). "U*nstructured grid techniques*", Annu. Rev. Fluid. Mech. 1997. 29:473–514

OPT — Ocean Power Technology website). Available from http://www.oceanpowertechnologies.com (accessed 17.10.2016)

Ploeg J. & Funke E.R., (1980). "*A survey of random wave generation techiniques*", International Conference on Costal Enegineering, ASCE, p.138.

Pontes, M.T, (1998). "*Assessing the European Wave Energy Resource*", Journal of Offshore Mechanics and Arctic Engineering, vol. 120, p. 226-231.

Previsic, M., Bedard, R. and Hagerman, G, (2004). "*Assessment offshore wave energy conversion devices*". Electric Power Research Institute, Electricity Innovation Institute, E21 EPRI WP 004

Raghunathan S. (1995) "*The Wells air turbine for wave energy conversion*". Prog Aerosp Sci 1995; 31:335–86.

Raghunathan S., (1995). Prog. Aerospace Sci. 31, 335.

R.H. Charlier and J.R. Justus (1993) "*Environmental, Economic and Technological Aspects of Alternative Power Sources"* Ocean Energies, Volume 56, 1st Edition, ISBN: 9780080870946

Saintfluo G., "*Essai sur les digues maritimes verticals*", Annales des Ponts

Sarmento A. J. & A. F. de O. Falcão, 1985. "*Wave generation by an oscillating surface pressure and its application in wave-energy extraction*", J. Fluid Mech. 150, 467.

Steven C. Chapra & Raymond P. Canale, (1998). "*Numerical Methods for Engineers*" Published by McGraw-Hill, a business unit of The McGraw-Hill Companies, Inc., 1221 Avenue of the Americas, New York, NY 10020.

Torresi M. S.M. Camporeale, P.D. Strippoli, G. Pascazio, (2008) . "*Accurate numerical simulation of a high solidity Wells turbine*" Renewable Energy 33 (2008) 735–747

Versteeg and W Malalasekera, (1995). "*An Introduction to Computational Fluid Dynamics*" Pearson Education Limited, Edinburgh Gate Harlow Essex CM20 2JE England.

Viviano A., Naty S., Foti E., Bruce T., Allsop W., Vicinanza D. (2016), "*Large-scale experiments on the behaviour of a generalised Oscillating Water Column under random waves*" Renewable Energy, 99 (2016) 875 – 887

WAVEPISTON website, available from http://www.wavepiston.dk (accessed 07.02.17)

Zhang J.F. Jin-Ping Wang, Zhi-Guo Qu, Ya-Ling He, Wen-Quan Tao , (2014). "*The study of different discretized schemes for density and convection terms in high*

speed compressible flow using the pressure-based method", Applied Thermal Engineering, Volume 73, 1533–1540.